

REPORT DOCUMENTATION PAGE

AD-A198 878

(2)

1. RESTRICTIVE MARKINGS													
2. DISTRIBUTION/AVAILABILITY OF REPORT Approved for public release, distribution unlimited													
3. MONITORING ORGANIZATION REPORT NUMBER(S) AFOSR-TR- 88-0290													
4. PERFORMING ORGANIZATION REPORT NUMBER(S)	5. NAME OF MONITORING ORGANIZATION AFOSR/NE												
6a. NAME OF PERFORMING ORGANIZATION Colorado State Univ	6b. OFFICE SYMBOL (If applicable)												
7a. ADDRESS (City, State and ZIP Code) Fort Collins, CO 80523													
7b. ADDRESS (City, State and ZIP Code) Bldg 410 Bolling AFB, DC 20332-6448													
8a. NAME OF FUNDING/SPONSORING ORGANIZATION Same as 7a	8b. OFFICE SYMBOL (If applicable)												
9. PROCUREMENT INSTRUMENT IDENTIFICATION NUMBER F49620-86-C-0083													
10. SOURCE OF FUNDING NOS.													
<table border="1"><thead><tr><th>PROGRAM ELEMENT NO.</th><th>PROJECT NO.</th><th>TASK NO.</th><th>WORK UNIT NO.</th></tr></thead><tbody><tr><td>61102F</td><td>2306</td><td>A2</td><td></td></tr></tbody></table>		PROGRAM ELEMENT NO.	PROJECT NO.	TASK NO.	WORK UNIT NO.	61102F	2306	A2					
PROGRAM ELEMENT NO.	PROJECT NO.	TASK NO.	WORK UNIT NO.										
61102F	2306	A2											
11. TITLE (Include Security Classification) Sub-Micron Carbon Filaments for Optical Applications													
12. PERSONAL AUTHOR(S) Ian L Spain, Carol M McConica													
13a. TYPE OF REPORT Final	13b. TIME COVERED FROM 15 Jul 86 to 15 Mar 87												
14. DATE OF REPORT (Yr., Mo., Day) Nov 87													
15. PAGE COUNT													
16. SUPPLEMENTARY NOTATION													
17. COSATI CODES													
<table border="1"><thead><tr><th>FIELD</th><th>GROUP</th><th>SUB-GR.</th></tr></thead><tbody><tr><td></td><td></td><td></td></tr><tr><td></td><td></td><td></td></tr><tr><td></td><td></td><td></td></tr></tbody></table>		FIELD	GROUP	SUB-GR.									
FIELD	GROUP	SUB-GR.											
18. SUBJECT TERMS (Continue on reverse if necessary and identify by block number)													
19. ABSTRACT (Continue on reverse if necessary and identify by block number) The objective of this work was to study the growth and physical properties of carbon fibers prepared by the ion-bombardment of carbon surfaces, with particular reference to optical obscuration applications. During the contract period, it was decided to include another class of carbon fibers grown by catalytic-chemical-vapor-deposition (CCVD). This initial work showed that submicron diameter filaments of high aspect ration could be grown. (JES) K													
20. DISTRIBUTION/AVAILABILITY OF ABSTRACT UNCLASSIFIED/UNLIMITED <input type="checkbox"/> SAME AS RPT. <input type="checkbox"/> DTIC USERS <input type="checkbox"/>													
21. ABSTRACT SECURITY CLASSIFICATION UNCLASSIFIED													
22a. NAME OF RESPONSIBLE INDIVIDUAL ROSENSTEIN	22b. TELEPHONE NUMBER (Include Area Code) 202-767-4933												
22c. OFFICE SYMBOL NE													

DD FORM 1473, 83 APR

EDITION OF JAN 73 IS OBSOLETE
888 24 012

SECURITY CLASSIFICATION OF THIS PAGE

DTIC
ELECTE
S AUG 24 1988 D

Final Report to AFOSR
SUB-MICRON CARBON FILAMENTS FOR OPTICAL APPLICATIONS

From: Ian L. Spain and Carol M. McConica
Colorado State University
Fort Collins, CO 80523

To: Major J. Hager
AFOSR
Bolling Air Force Base
Washington, D.C. 20323

Accession For	
NTIS CRA&I	<input checked="checked" type="checkbox"/>
DTIC TAB	<input type="checkbox"/>
Unannounced	<input type="checkbox"/>
Justification	
By	
Distribution/	
Availability Codes	
Dist	Avail and/or Special
A-1	

Contract #: F49628-86-C0083

Date of Report: November 1987

Period of Contract: July 15, 1986 to November 14, 1987



TABLE OF CONTENTS

I.	Introduction	1
II.	Growth of Carbon Filaments	2
II.1	Apparatus	2
II.2	Growth of CCVD Filaments	3
II.3	Thermal Calculations for the Growth of CCVD Filaments	3
II.4	New Methods for Preparing Catalysts	4
II.5	Growth and Structure of Vapor-Deposited Filaments on Carbon and Silicon Substrates	4
II.6	Thickened Carbon Fibers	5
II.7	Some Speculations Concerning Growth Features on Carbon Surfaces Due to Ion-Bombardment	5
II.8	Fibers Grown from Ion-Bombardment of Carbon and Silicon Substrates from Plasmas	5
III.	Physical Property Measurements	6
III.1	Electron Microscope Studies	6
III.2	Relationship Between Elastic, Structural, and Piezoelectric Properties of Carbon Fibers	6
III.3	The Elastic Parameters of Graphite	7
III.4	The Electrical Properties of C/BN Alloys	7
IV.	Review of the Physical Properties of Carbon Fibers and Filaments	8
V.	Subcontract to Oregon State University	8
VI.	Summary	8

I. INTRODUCTION

Earlier studies on carbon filaments were funded by a joint contract to Colorado State University and IBM Watson Research Laboratories (see Final Report to AFOSR on Contract #F49628-84-K-0006). The objective of this work was to study the growth and physical properties of carbon fibers prepared by the ion-bombardment of carbon surfaces, with particular reference to optical obscuration applications. During the contract period, it was decided to include another class of carbon fibers grown by catalytic-chemical-vapor-deposition (CCVD). This initial work showed that submicron diameter filaments of high aspect ratio could be grown. However, they were not straight.

Although straight filaments are not necessarily required for obscuration applications (it is possible that coiled and helical filaments have higher scattering and absorption cross-sections), the comparison of theoretical models and optical measurements can only be carried out for this case at the present time. Accordingly, the present contract was funded together with one to Panametrics, Inc. in which the overall objectives were as follows.

1. To ascertain the conditions under which relatively straight submicron diameter carbon filaments of high aspect ratio can be grown. Although the thrust of this work was with CCVD filaments, some experiments were to be carried out with plasma-assisted growth.

2. To characterize the structure and electrical resistivity of these filaments.
3. To provide Panametrics, Inc. with samples of these filaments, so that electromagnetic scattering and absorption experiments could be carried out and compared to theory.
4. A thorough review of the physical properties of carbon filaments was to be carried out in collaboration with other experts working in the field.
5. Advances in carbon science were to be made wherever appropriate to the overall aims of the above work (growth mechanisms and models, structure, physical properties, etc.)

Progress made in the present contract to Colorado State University will be reviewed in this report. A brief account will be given first in this section, with further details in Sections II-V. Each brief account below is given the same number as the corresponding report section.

II. GROWTH OF CARBON FILAMENTS

II.1 Apparatus

A differential high vacuum system has been constructed to allow the growth and in situ characterization of CCVD carbon filaments in a clean environment. In some of the earlier CCVD filament work by McKenney and Bowers, there was the possibility of contamination coming from within the system; impure source gases and impure environment (i.e., air). A system has now been built where these impurities have been minimized. Along with being a clean system, it is technologically superior to the old furnace and tube system used in the earlier work, employing mass

flow controllers, temperature programming, and precision pressure measurement.

II.2 Growth of CCVD Filaments

The growth parameters which have been identified are the amount of catalyst evaporated, catalyst reduction time and temperature, hydrogen to hydrocarbon ratio, total flow rate, use of inerts, type of graphite substrate and the catalyst type. The growth of fibers on nickel with acetylene optimizes at low temperature, long times and with a predeposition hydrocarbon saturation period. Highly oriented pyrolytic graphite is a superior substrate for it does not allow nickel diffusion into the bulk, leaving more catalyst for filament growth. Methane was found to produce no filaments on nickel at 1000°C. Chemically deposited iron catalysts did give abundant filament growth with acetylene in the 600-1000°C temperature range. Optimization of growth parameters will continue for the Fe/acetylene and Fe/benzene systems.

II.3 Thermal Calculations for the Growth of CCVD Filaments

Assuming that the catalytic dehydrogenation of acetylene proceeds at a rate identical to the diffusion rate of carbon in nickel, and thus the filament growth rate, no temperature rise was predicted on the nickel surface. If this were true, deposition would not be self-limiting. Because filament growth is self-limiting, carbon must be accumulating on the catalyst surface, suggesting that a nonsteady model must be solved, in which the acetylene decomposition rate is greater

than the filament growth rate. This nonsteady state problem will be solved in the next year.

II.4 New Methods for Preparing Catalysts

Four methods have been used to create supported metal substrates. Nickel was evaporated onto both Poco and (HOPG) samples. The method of ion exchange was used with semiconductor grade silicon dioxide in order to deposit angstrom-size nickel clusters. The defect-free SiO_2 surface prevented ion exchange, thus no nickel or growth resulted. Iron was deposited in a chemical bath of $\text{FeCl}_2 \cdot 4\text{H}_2\text{O}$. Extensive filament growth resulted. Quantitative control of iron deposition is currently being achieved electrochemically. New methods for growing very small metal clusters will be established in the next year.

II.5 Growth and Structure of Vapor-Deposited Filaments on Carbon and Silicon Substrates

It was found in the previous contract period that filaments grown on silicon substrates with nickel substrates at 850°C were unexpectedly graphitic. Further measurements were carried out in the present contract period at temperatures between $700\text{--}1000^\circ\text{C}$, indicating that graphitic filaments were only grown over a narrow temperature range and that SiC was formed at higher temperature. This SiC is probably on the substrate, and not filamentary. The results were interpreted qualitatively in terms of a model of the growth processes. A paper on our earlier work is to be published shortly in Carbon, and a further paper on our recent work is to be submitted to the same magazine.

II.6 Thickened Carbon Fibers

The chemical-vapor-deposition technique can also be used to thicken fibers. Experience with the growth of filaments suggests that this thickening occurs preferentially above about 1100°C. Commercial ex-PAN fibers were thickened from acetylene/hydrogen vapors using controlled conditions. The results were interpreted to give information about the kinetics of the reaction. This work will continue in the following contract period as a collaborative project with the University of Newcastle, UK, and will include the fabrication of carbon composites using these fibers and the measurement of mechanical properties.

II.7 Some Speculations Concerning Growth Features on Carbon Surfaces Due to Ion-Bombardment

A model for the growth of carbon filaments by bombardment of carbon surfaces by energetic (~1 keV) ions was presented in the previous contract report. This model was based on the idea of mobile carbon atoms on the surface supersaturating at preferential sites and leading to continued growth. Further work was carried out which established the importance of further growth from redeposition of sputtered atoms and suggested a mechanism for the observed increase in the density of growth features with temperature. A paper on this topic is to be submitted to J. Cryst. Growth.

II.8 Fibers Grown from Ion-Bombardment of Carbon and Silicon Substrates from Plasmas

Carbon filaments were grown on three types of carbon surfaces from argon, argon/hydrogen, argon/propane, and argon/methane plasmas. The growth features depended on the substrate and plasma gas and did not

appear to fit current models of the growth processes well. None of these experiments produced straight filaments of uniform diameters. Experiments were also carried out with silicon substrates and unusual growth features were observed. No submicron filaments were grown. A paper on this topic is to be submitted to J. Vac. Sci. and Tech.

III. PHYSICAL PROPERTY MEASUREMENTS

III.1 Electron Microscope Studies

Carbon filaments grown by CCVD techniques were studied by several electron microscope techniques, including scanning microscopy, high-resolution transmission electron microscopy in both selected-area and converging-beam modes, lattice fringe imaging, and energy-dispersive x-ray analysis. This work is in a preliminary stage and will be pursued further in the next contract period.

III.2. Relationship Between Elastic, Structural and Piezoelectric Properties of Carbon Fibers

A considerable body of experimental work was carried out at Celanese Research Company (ARO Contract #DAAG29-81-C-0016) on structural, electrical, mechanical, and piezoelectrical properties of ex-PAN and ex-pitch carbon fibers in collaboration with one of the present PIs. This work was analyzed further during the current contract period in which the Young's modulus of the fibers was fitted to elastic constants of the hexagonal layers using data on the orientation distribution function obtained from x-ray diffraction measurements. These data were then used to analyze the piezoelectric coefficient for different fiber types. This work is of particular importance since it

tested current models for fiber properties in novel ways. The report on this work is to be submitted to J. Appl. Phys. once permission has been granted from Hoechst-Celanese Research Company.

III.3 The Elastic Parameters of Graphite

The variations of the lattice parameters with pressure of graphite were studied experimentally in the last contract period. The results were analyzed further in this period, giving information about the C-axis elastic parameter C_{33} and its variation with strain. Of particular importance is the ability of these measurements to measure the elastic constant C_{13} . The previous value obtained from ultrasonic measurements was 15 ± 5 GPa, and that from our results 21 ± 2 GPa. This elastic parameter is of importance in physical properties of graphite and carbon fibers, such as the thermal expansion and the piezoelectric effect. A paper on the high pressure data and analysis of results has been submitted to Phys. Rev. (accepted with minor changes), and a letter to Carbon on the value of C_{13} is to appear shortly.

III.4 The Electrical Properties of C/BN Alloys

Some applications of high-strength fibers require lower electrical conductivity than that of typical carbon fibers. One conceptual way to achieve this is by alloying carbon with boron nitride. Samples of C/BN were prepared at Union Carbide Parma Laboratory, which also provided us with a small grant to initiate this work. The electrical resistivity, Hall Coefficient, and magnetoresistance of several samples were determined experimentally. It was found that electrical properties were

similar to those found on boronated samples of graphite. It is intended to submit a paper on this topic to J. Appl. Phys.

IV. REVIEW OF THE PHYSICAL PROPERTIES OF CARBON FIBERS AND FILAMENTS

It was intended to prepare a review of approximately 125 pages for Advances in Physics on the physical properties of carbon fibers and filaments. The final article was much longer than this and, being of unsuitable length for this magazine, will be published as a book in early 1988 by Springer Verlag (~500 pages, 600 references).

V. SUBCONTRACT TO OREGON STATE UNIVERSITY

A subcontract was awarded to James A. VanVechten of Oregon State University to study theoretical aspects of carbon filaments. His work established a theoretical basis for unusual forms of carbon, characterized by "magic numbers" which have been observed in pulsed laser ablation experiments and explained the unusual density of the carbon in ion-grown filaments. This work has been published in Physical Review, Rapid Comm. and has excited the interest of the popular press (Science News, 15 August 1987).

VI. SUMMARY

Although the above represents a considerable body of accomplished work, we have not yet succeeded in producing relatively straight filaments with high aspect ratios for which the electrical resistivity has been characterized. The reasons for this will be discussed in the technical reports, but in summary:

1. It has not proved possible to duplicate the results reported earlier on plasma-grown filaments. (This work was reported in a brief form, and we have been unable to obtain further details of the results.)
2. It appears that the acetylene/nickel combination does not produce filaments at temperatures above 850°C. It is hypothesized that at the high temperatures needed for straight filament growth, the nickel surface becomes completely covered and is no longer catalytic. Optional filament growth for the acetylene/nickel system occurs at temperatures below 850°C.

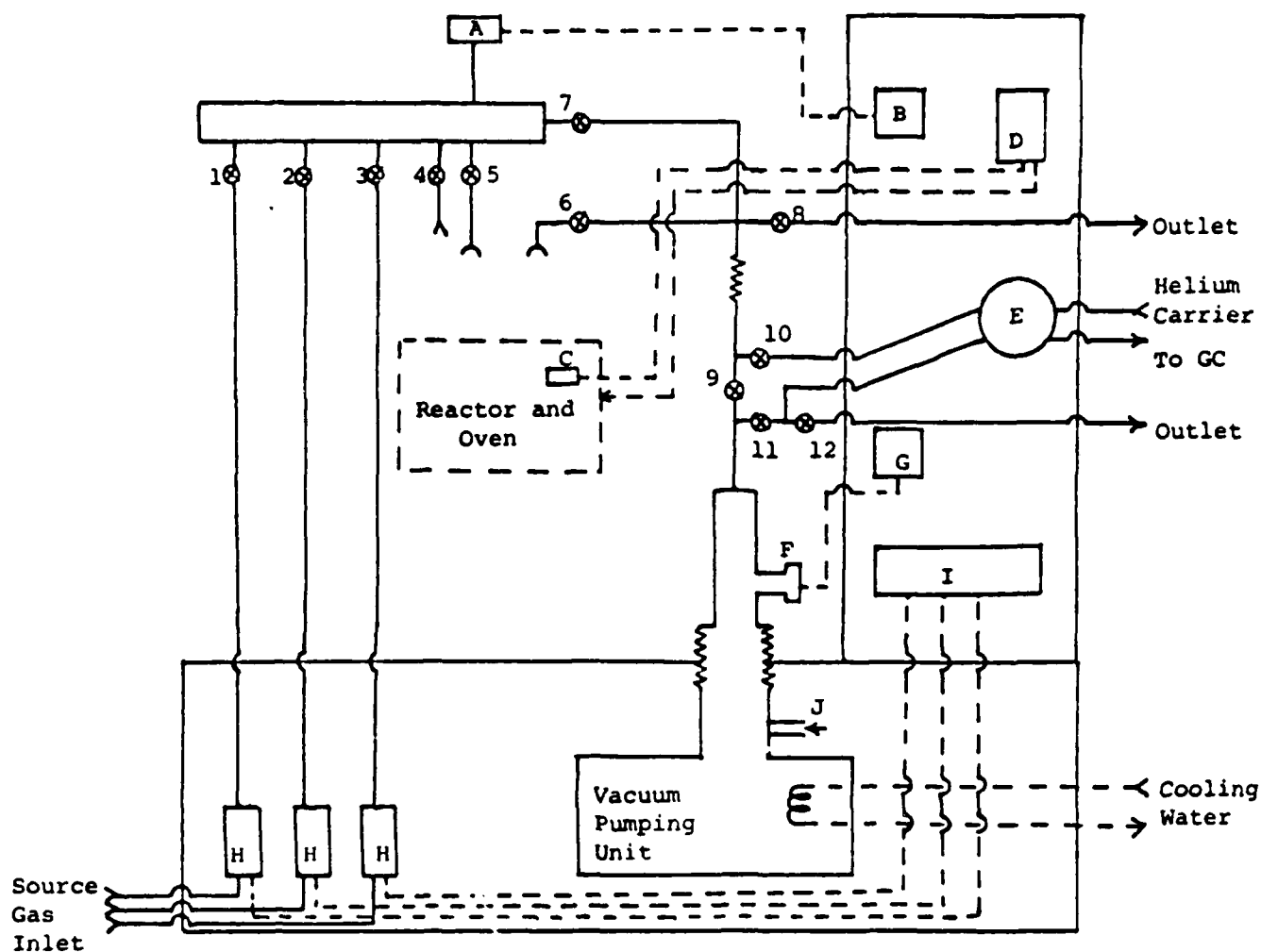
Further work will be carried out in the following contract to resolve these issues and to grow the required filaments.

II-1. APPARATUS

Christina Schmitt and Carol M. McConica
Department of Chemical Engineering
Colorado State University
Fort Collins, CO 80523

Introduction

A differential high vacuum system has been constructed to allow the growth and in-situ characterization of CCVD carbon filaments in a clean environment. In some of the earlier CCVD filament work by McKenney and Bowers, there was the possibility of contamination coming from within the system; impure source gases and impure environment (ie: air). A system has now been built where these impurities have been minimized. Along with being a clean system, it is technologically superior to the old furnace and tube system used in the earlier work, employing mass flow controllers, temperature programming, and precision pressure measurement. A complete schematic of the system is shown in Figure 2.1.1.



- A- Capacitance Manometer
- B- Manifold Pressure Readout
- C- Thermocouple
- D- Temperature Programmer and Controller
- E- Six-Way GC Valve
- F- Cold-Cathode Ion Gauge
- G- Ion Gauge Readout
- H- Mass Flow Controllers
- I- Flow Controller Readout
- J- Emergency Vent Valve

Valves #1-8: High Vacuum Glass Stopcocks

Valves #9-12: Stainless Nupro (SS-4H)

FIGURE 2.1.1 High Vacuum CCVD System

Justification of Design and Equipment

Pump Unit: The pumping station is a Balzers TSH 170 Turbo-molecular pumping unit, having a nitrogen volume flow rate capacity of 170 l/s and operating pressure from 760 to less than 5×10^{-8} Torr. This pump is both convenient and efficient for CCVD work; convenient in that there is no contamination from pump oil, and therefore less maintenance than for a diffusion pump, and its compact size allows easy relocation. It is efficient in that despite it being on the small end of turbopumps, it has a short pump down time and is capable of pumping all lines in the system, back to gas regulators, to the range of 10^{-6} Torr (measured at the pump inlet) in less than 30 minutes. At this pressure, measured at the pump inlet, pressure at the manifold is approximately 10^{-2} Torr. The large pressure drop between the pump inlet and manifold is due to the small diameter lines (discussed later in this section) and a rough calculation has been made based on this resistance.

Other features added to the pumping station are:

Emergency Vent Valve: This protects the turbopump by causing automatic purging and shutdown when the system over pressurizes. There is also the option to bypass the vent valve to allow for low pressure runs, but this eliminates the safety and wear maintenance feature of the

emergency vent valve and is only utilized during low pressure runs.

Bellows: The stainless steel bellows protects the glassware from vibrations caused by the turbo and backing pumps.

Screen: A splinter shield is used in the line just upstream of the pump. Unfortunately, a mesh size that would prevent carbon filaments from entering the turbo pump would impede pump performance. This screen can only protect the blades from glass splinters or other accidental foreign objects. (See later, in section on reactor design that quartz frits are used in some reactors to prevent escape of filaments.)

Cold Cathode Ion Gauge: A Varian 524-2 Cold Cathode Ionization gauge is mounted just beyond the bellows at the pump inlet. It is mounted on a 2.5" diameter stainless steel tube to give most accurate pressure measurement (as close to pump inlet as possible). This gauge measures pressures from 1×10^{-7} to 10^{-2} Torr and its output is displayed by a Varian 860A-2 Cold Cathode Gauge Control mounted on the cabinet.

Plumbing from pump station to glassware: All lines from the large diameter tube at the pump inlet up to the glassware are .25" stainless with Swagelok fittings. Nupro SS-4H (high vacuum capability throttle valves) are to prevent pressure 'bursts' to the pumping unit which could cause shutdown. There is a 6-way gas chromatograph valve to allow

on-line sampling of reactant or product gases. The plumbing around the 6-way GC valve gives the user the following options: pump system only (excluding GC valve), pump system and GC valve, run through the pump only (low pressure runs without GC use), run through the GC only (atmospheric pressure runs), or run through the GC and pump (low pressure runs with GC capabilities). The stainless lines are attached to the glassware by a glass to flex metal tube (permanently attached on glassware end) to decrease stress on the glassware.

Glassware:- The motivation for using glass for the reactors and gas manifold was that it is cheaper and more inert than stainless steel (Nickel in stainless can catalyze filament growth). The manifold is used for mixing of reactant gases and has four inlets (forseeing the possible use of mixing hydrocarbons) and is small enough (about 1 liter) to allow BET studies to measure carbon filament surface area. An MKS Baratron type 222C Capacitance Manometer is mounted on the manifold with a VCO fitting. The pressure range of this manometer is 0.1 to 1000 Torr with an accuracy to 0.5% of reading. The pressure readout is an MKS PDR-1 and is mounted on the cabinet. The two outlets from the manifold go to the reactor and directly to the pump (stainless plumbing). The line to the pump is used as a bypass so that the user is able to

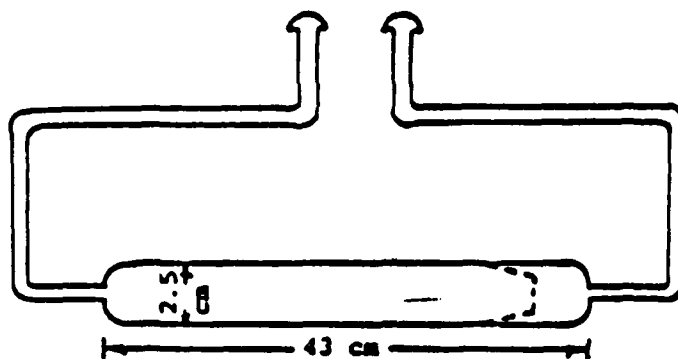
evacuate all lines when there is no reactor attached. This saves pumping time by being evacuated during off time. There is also a vent valve off of this bypass which can be used during runs (reactor attached) that take advantage of neither pump nor chromatograph. This has been used on most of our runs to prevent unnecessary soot buildup in the remainder of system. All valves in the system are high vacuum stopcocks. (Both high vacuum Silicon grease and Apiezon have been found satisfactory. The less expensive Si grease is being used.) The four inlets to the manifold are .25" glass lines with VCO fittings.

Plumbing from gas sources to glassware: The source gas regulators are all fitted with vacuum regulating tee's to allow evacuation of gas lines up to the regulators. The lines are teflon which is inert and allows for easy movement of the entire system. Each gas is in line with its own mass flow controller (MKS type 1259B). The hydrogen and helium (inert) have flow controllers with a range of 0-200 sccm, and the hydrocarbon flow controller has a range of 0-20 sccm. Accuracy is to 0.5% of full scale. The mass flow controllers interface with the power supply and an MKS type 247B (4 channel independent or ratio mode control) readout mounted on the cabinet front panel for easy access. The flow controllers are all mounted on the lower cabinet shelf (along

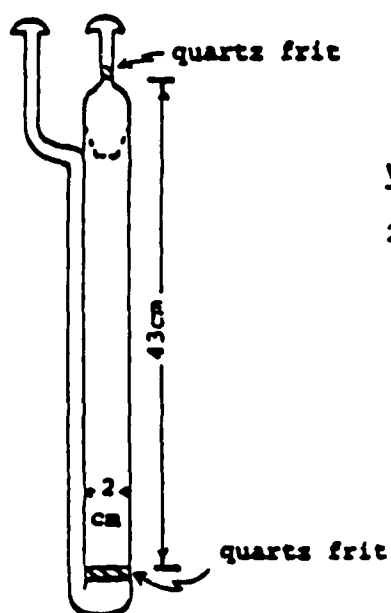
with the pumping station).

Heating Unit: All reactors are designed to fit into a high temperature resistance heated oven. The oven allows for reactors with diameters up to 1", and it cannot be opened, so reactors must be able to slide through. The oven can be rotated to a horizontal or vertical position. An Omega CN-2010 Programmable Temperature Controller and SSR 240 A45 solid state relay are used to power and control the oven. The temperature controller has an eight step ramp and soak capability, giving the option of various heating rates and either on/off or PID control. The PID control loop gives an overshoot of less than 10°C at 1000°C and controls within 1°C after about 5 minutes at this temperature. The controller has one input/output for the oven. A type K Chromel-Alumel thermocouple is used for input.

Reactors: There are currently 4 reactors; 2 each of horizontal and fluidized bed (vertical), (see Figure 2.1.2). All are made of quartz and have inlet and outlet male socket joints, where they are clamped to the rest of the glassware. The horizontal reactors are composed of 2 pieces so they can fit through the oven. The pieces are connected by a ground glass joint where substrates can easily be loaded and unloaded. The joint is located at the reactor outlet, so as not to introduce any



Horizontal Reactor
2 pieces, quartz



Vertical Reactor (Fluidized Bed)
2 pieces, quartz

Silicon grease prior to the reaction on the substrate. The fluidized bed design is a vertical structure with a gas preheat tube. The bed itself is contained between two quartz frits which prevent catalyst particles and filaments from escaping. The top frit (at reactor outlet) is housed in a reactor cap, which can be removed for catalyst loading and unloading.

Experimental Procedures

Because a clean system for filament growth and characterization has been constructed, special procedures are followed during experiments, and during general system maintenance, to insure that everything used is, and remains clean.

Substrates: All substrates (Silicon wafers, Poco graphite, and single crystal graphite) are cleaned with organic solvents, rinsed in deionized water, and baked in a convection oven at 60°C. The most common technique for catalyst deposition is evaporation. The evaporator is located in a Class 100 clean room. The source for the evaporated nickel is nickel powder, 99.999% pure. Substrates are blown off with nitrogen (clean room- unpurified) prior to evaporation. All substrates are stored in a dessicator until ready for filament growth. Other catalysts that have been used for filament growth are in the form of

powders. They have been prepared earlier (McConica) and are used as is (in fluidized bed reactors). More catalyst deposition techniques will be discussed in a later section.

Source Gases: All gases used in CCVD carbon filament growth experiments are high purity: Hydrogen (99.9998%), Helium (99.998%), Argon (99.999%), Acetylene (Grade 2.6), Methane (99.5% minimum), Air (Breathing quality- used for baking out reactors after runs are completed).

Preparation for Run: The system was closed off to the atmosphere and evacuated (continuously) when no run was being made. (Evacuated up to manifold inlets, no reactor attached.) The reactor, with substrates inside, was attached to the rest of the system prior to run, and was also evacuated. All lines from source gases to be used were evacuated and then filled with their respective gases up to their mass flow controllers.

Running Filament Growth:

The evacuated system was shut off from the pump station. Either hydrogen or helium (inert) was turned on (now the substrates are heated and cooled in an inert, but some of the first runs used hydrogen (see Experimental Results)). The system was filled until the capacitance

manometer read above atmospheric pressure (630-640 Torr in Ft. Collins), and then an exit line was opened, bringing the pressure back down to atmospheric (running pressure). At this time the temperature programming began. Pressure and temperature were monitored closely. When helium was used during the heat period, a separate reduction period was used where the flow was switched over to hydrogen (at the same total flow rate as the helium). The reduction temperature was then the same as the run temperature. Directly following the reduction period there was either the actual run (hydrogen and hydrocarbon) or a hydrocarbon saturation period (inert and hydrocarbon), followed by a CCVD run. In either case the total flow was kept constant by decreasing the hydrogen or the inert flow rate. All runs were at constant temperature, but temperature and pressure were monitored throughout, to make sure that no reaction 'ran away' or that there was no pressure buildup due to soot blockage. When the run was complete, the oven input was turned to 0%, and the reactor cooled (inside the oven for horizontal reactors, so cooling was slow). Only inert (helium or argon) was flowed through the system during cooling (some earlier runs used hydrogen, but this may have caused depletion of carbon filaments by the reverse of the decomposition reaction). The inert was left flowing until the reactor and substrate

were below 400°C (more than 3 hours for runs at 1000°C). When the helium was shut off, air could enter the system, so the substrate was cooled enough to assure that there would be no oxidation of the filaments.

Only one low pressure run has been made. The procedure differs from that of atmospheric runs in that the system was not closed off to the pump, but was throttled to keep the reactor at the desired operating pressure (greater than 1 Torr). All gases exited through the pumping system. The emergency vent valve was not used during low pressure runs, to keep the turbopump operating while there was inlet flow. The turbopump cannot operate at full speed during low pressure runs.

Clean Up: When runs were complete, substrates were removed from reactors and placed in a dessicator until ready for analysis. The reactor was baked out, and the system was prepared for the next use. The reactors were baked at 800°C in air flowing at 100 sccm after each run to burn off any carbon deposited on the walls. After every few runs, or when there was an abundance of carbon deposited upstream of the substrate, reactors were cleaned in aqua regia to remove any metal deposits which may cause extraneous reactions.

Analysis: A scanning electron microscope was used to observe the substrates for filament growth. Substrates were glued onto SEM stubs with graphitic paint, baked in a vacuum oven, and gold sputtered. We have found the following conditions to work the best for our samples in the Philips 505 SEM: Accelerating Voltage set at 25 keV, filament current at 30 uA, bias voltage at 150eV, and a spot size of 20 nm. More on analysis techniques is discussed in another section of the report. EDAX has also been done on the most recent samples (after B9) to check for impurities on the substrate which may be a source of filament growth. These samples were not gold sputtered and an accelerating voltage of 30 keV was used to penetrate carbon on the sample surface. Only nickel was found lying on the substrate (besides the carbon) which indicates that there were no impurities being introduced onto our substrates during preparation. (See Figure 2.1.3 for an example of EDAX).

B-11 (CS 11/12/87)
100 sec

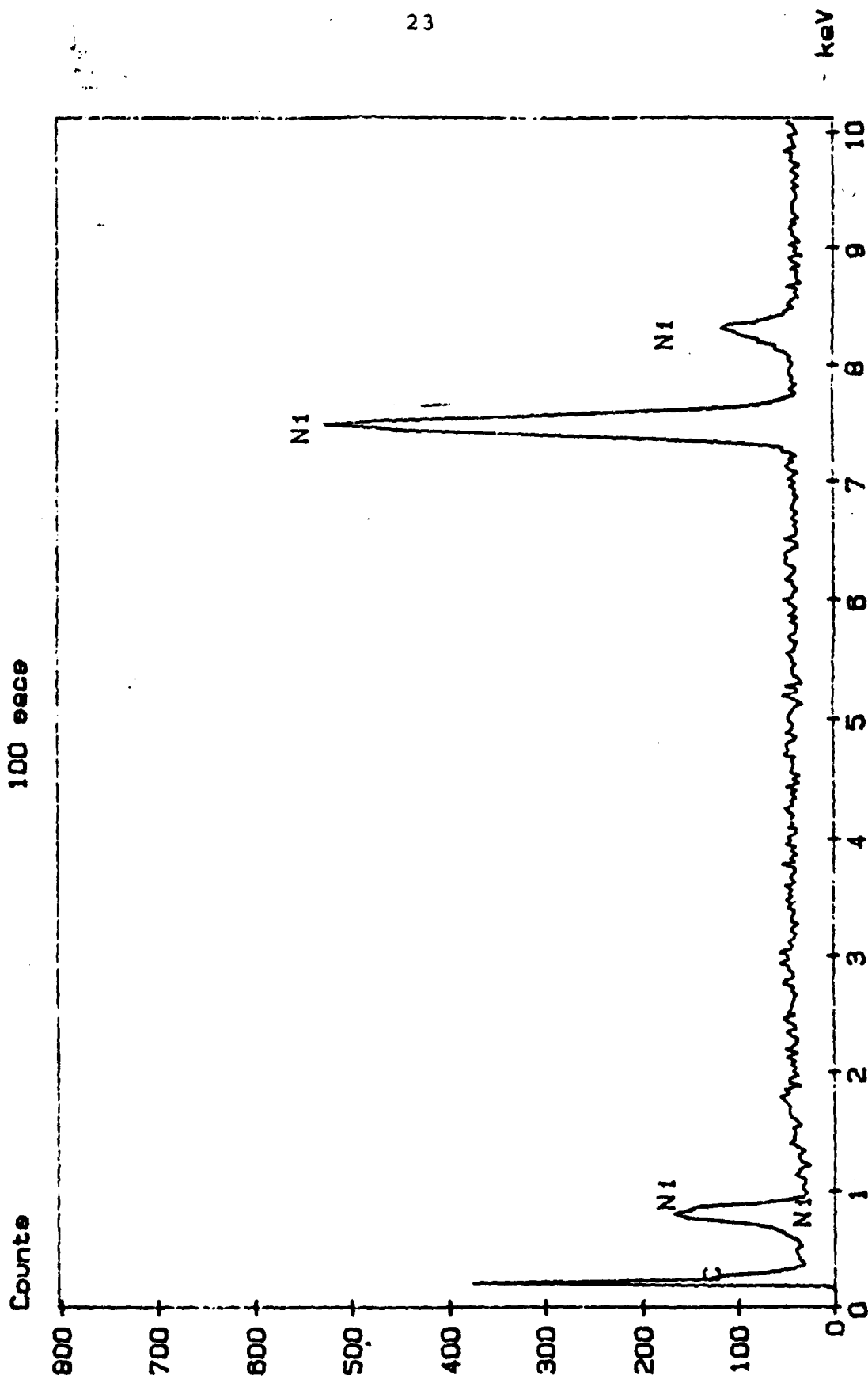


FIGURE 2.1.3 EDAX on Sample B11

II-2. GROWTH OF CCVD FILAMENTS

Christina Schmitt and Carol M. McConica
Department of Chemical Engineering
Colorado State University
Fort Collins, CO 80523

Introduction

The overall objective of the experimental work on CCVD carbon filaments thus far, has been to find a method by which straight, submicron filaments can be grown with aspect ratios > 1000 . The purpose for filaments of this type has been discussed elsewhere. The high vacuum system that has been built enables production of filamentous carbon in controlled growth regimes, and good reproducibility in experiments has been shown. Much of the work here is a continuation of earlier work done at CSU by McKenney and Bowers; ie: Nickel catalyst evaporated on graphite substrates, and acetylene used as the hydrocarbon. The growth parameters which have been identified are the amount of catalyst evaporated, catalyst reduction time and temperature, hydrogen to

hydrocarbon ratio, total flow rate, use of inerts, and type of graphite substrate. Since it is believed that the catalyst plays a major role in the dimensions of the filament, we have also looked at various methods for seeding the substrates (discussed in more detail in another section.) Because the system is new, many of the experiments were more relevant towards it's characterization which help to substantiate and interpret the results of grown filaments. A statistical approach is employed for setting up and analyzing the results of the CCVD carbon filament growth.

Initial Runs

The first four runs made on the system were done to verify that the system was actually working. Run #'s 1, 2, and 3 were conducted at temperatures between 700 and 850°C. Substrates were nickel evaporated on Poco graphite (prepared by Bowers). Acetylene was used as the hydrocarbon with hydrogen to hydrocarbon ratios from 10:1 to 50:1. All three runs were 15 minutes long (time of acetylene flow). Many submicron filaments were grown using these conditions. Run # 4 was made to test the fluidized bed reactor. The catalyst was in the powder form, 2.73% nickel on silica. Only amorphous carbon was deposited. During

these four runs the system was monitored very closely, especially the temperature profile. Substrates were placed at the same axial location in the furnace tube as the thermocouple, though the thermocouple was located between the reactor wall and the furnace. Temperature readings were plotted against time as some of the tuning parameters in the temperature controller were varied. Good control was achieved. An example of a temperature profile is shown in Figure 2.2.1.

One run was made at low pressure (between 10 and 100 Torr) to check the performance of the pump, and, of course, to examine for filamentous growth. This run, A3LP, gave mostly nucleation 'clumps' and only very short, tangled filaments. The pumping unit ran at less than half speed when total pressure was 10 Torr. To alleviate some of the stress on the pump the total pressure was increased to 100 Torr 5 minutes into the 10 minute run. No further attempt has been made to run below atmospheric pressure.

Five experiments have been run to survey different substrates and catalyst preparation techniques. Nickel evaporated on Si (Run Si-1) was one such substrate (prepared by Bowers). Growth conditions were similar to previous conditions on graphite substrates where filaments grew, but none grew on this particular substrate. Four graphite substrates were

Run B2 (10/5/87)
Cycle Time=1 second
Tolerance=10°C (Assured Soak)
Ramp Rate=10°C/min
X=set points

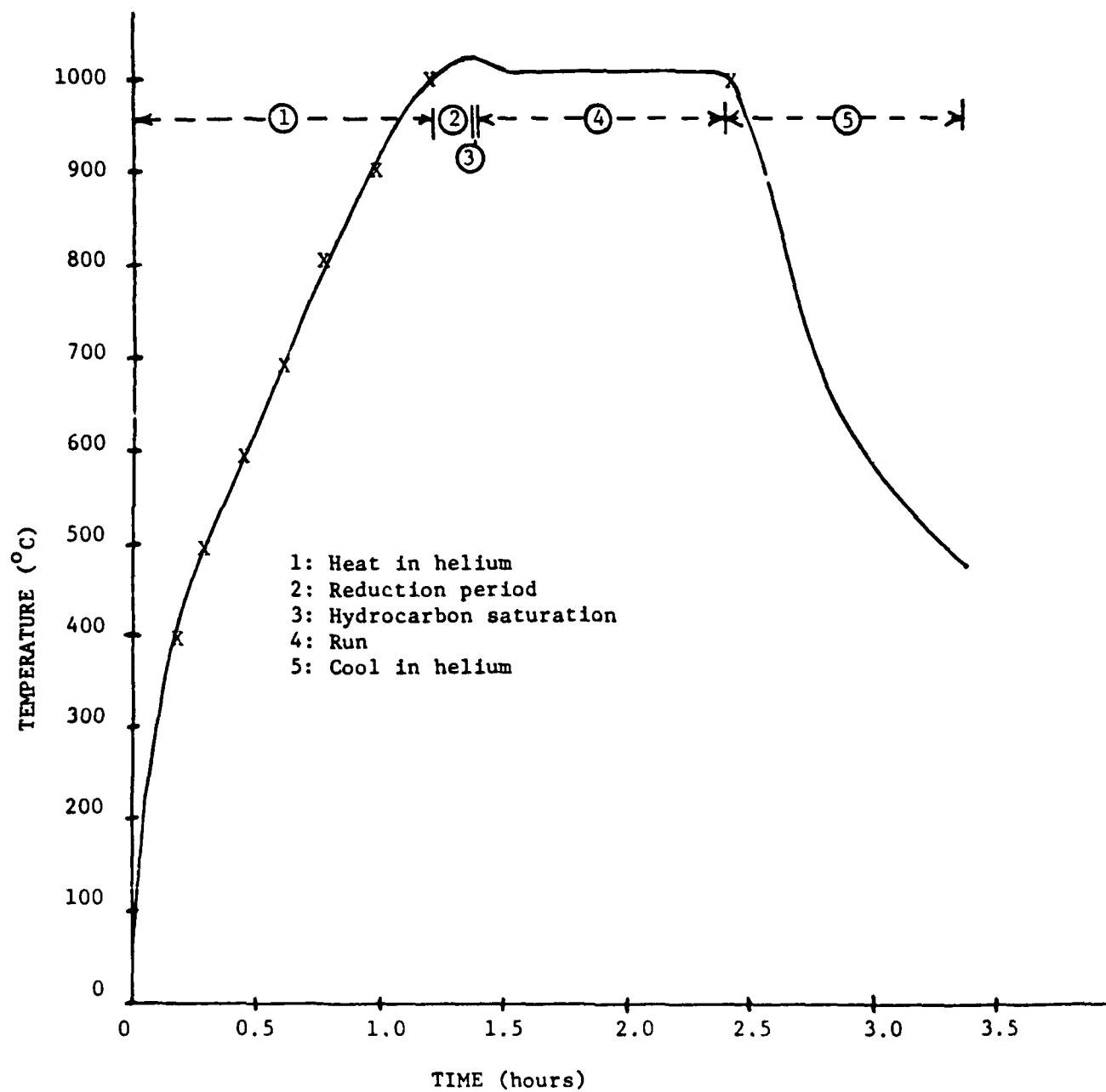


FIGURE 2.2.1 Temperature Profile

prepared by plating them with nickel using a Watts nickel solution at various load times/currents (at PCB Colorado). This preparation was not very controlled, and was made more as an inquiry to see if this type of deposition should be pursued. The two runs made on two of these plated substrates (PCB1 and PCB2) gave very interesting octopussy, or sea-urchin, type growth, which appeared to be similar to some sulfur catalyzed fibers.¹ . Filaments grown were fairly straight, with submicron diameters, and some aspect ratios >100 (see Figure 2.2.2). However, this growth cannot be attributed to the nickel catalyst because the plating solution (electrolyte) may have contributed many impurities to the substrate. EDAX was done on one of these electroplated substrates before filament growth, and although there was a lot of noise in the reading, there does not appear to be anything besides carbon and nickel on the substrate. Most of the noise occurred around where the sulfur and lead peaks were located. (See Figure 2.2.3). The study of CCVD filament growth on electroplated substrates has ceased, but it will be pursued in the future with modifications in the purity of the electrolyte (see other section).

Runs IX-1 and IX-2 used substrates prepared by an ion exchange technique (see other section for details). Nickel was deposited on

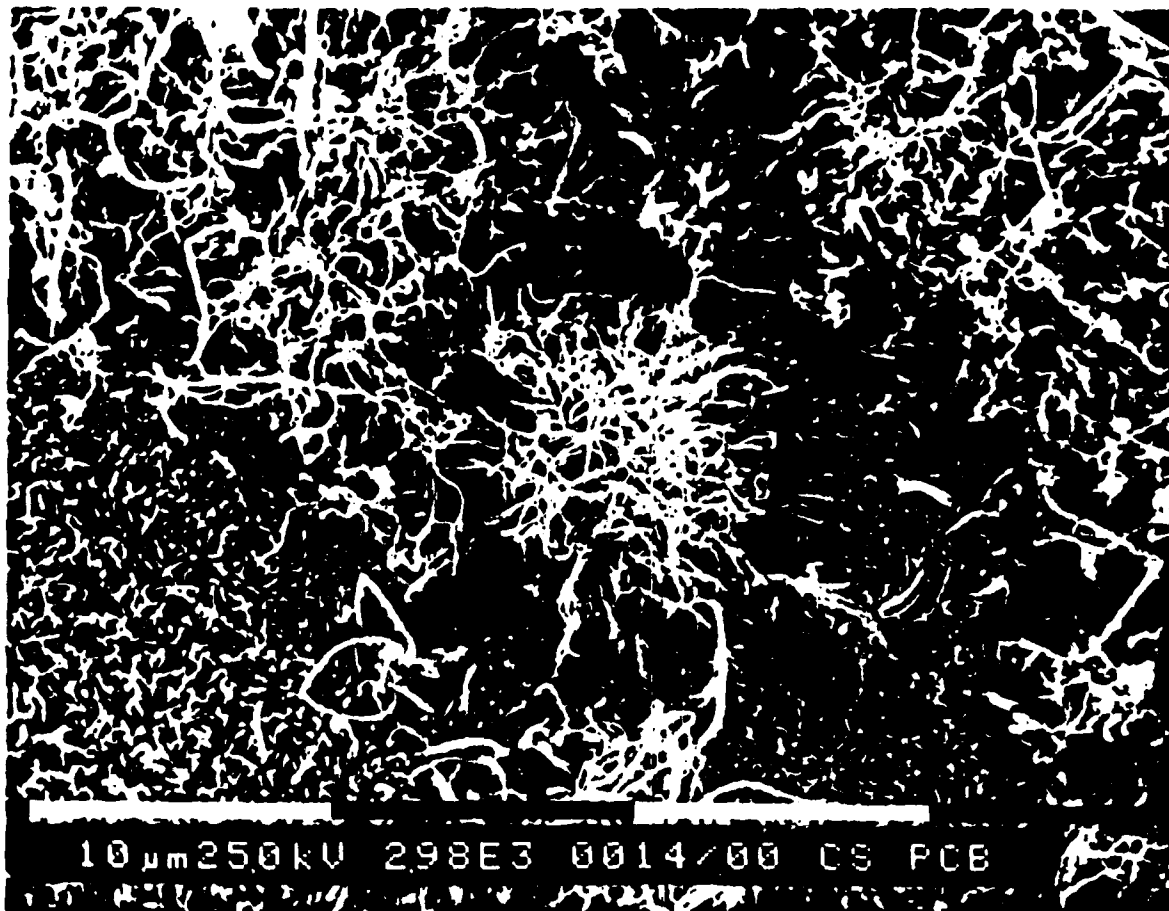


FIGURE 2.2.2 Sea-Urchin Type Filament Growth

PCB-4 (C.S. 11/19/87
100 eace

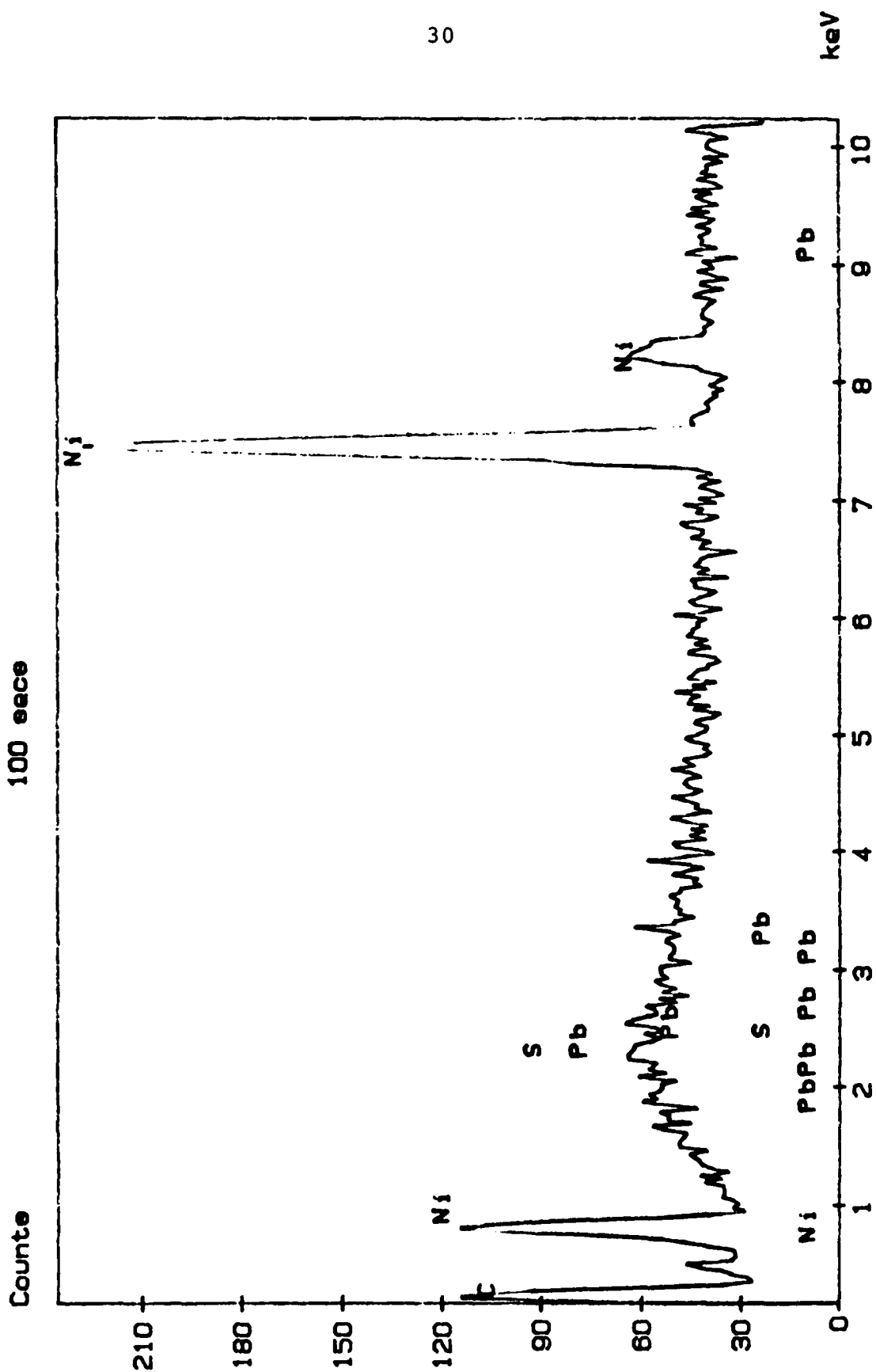


FIGURE 2.2.3 EDAX on PCB Substrate

silica wafers at different weight loadings. There was no carbon deposition observable by eye, and both samples were inadvertently destroyed before any SEM analysis could be made.

All runs 1-4, PCB, A3LP, and some of the earlier matrix A runs (see below) were conducted with hydrogen as the cooldown gas. The hydrogen may have depleted the mass concentration at high temperatures, where the hydrogenation reaction rate could be significant. To check the effect of hydrogen flow during cooldown, 2 experiments were run, 3-I and 4-I, which used helium instead of hydrogen during cooldown, but were otherwise identical to run #'s 3 and 4 respectively. No more abundant growth was attained in 3-I than in run #3, and no growth of filaments was observed in 4-I as in run #4. Both of these runs were conducted at 850°C. There may have been a more pronounced difference between hydrogen and helium cooldowns at higher temperatures (eg. 1000°C) but this was not measured. However, the run procedure was changed, and now a helium cooldown is incorporated in all runs. Hydrogen was used later for cooldowns at low temperature (run temperature=600°C) when the helium flow controller was being used for other gases. Most likely, the hydrogen caused no filament depletion at this temperature, and it did prevent any oxygen from entering the system, which would oxidize any

filament growth even at this temperature.

Statistical Approach

There are many ways to statistically design an experiment. Ideally, it is desired to get the most information (useful information) from the results of the CCVD growth with the least amount of experimentation. In the growth of CCVD carbon filaments, there are many growth parameters, and to do a complete study on all of them, and all of their interactions, would take an unreasonable amount of time. Instead, experiments have been set up using the method of self-directing optimization (SDO).² The primary goal at this point in the research is to optimize, not to document effects. A matrix of 8 experiments is used for a 7 variable problem. (See Table 2.2.1). Each variable is given an upper and lower bound, for example, run temperature between 600 and 1000°C. The upper and lower bounds should be working limits, where, hopefully, the optimum lies within. If there is no direction induced from the statistical approach, perhaps the limits have not been reached, so therefore, it is a good idea to exaggerate these limits (which, as is seen in the next section, has not been done due to other limitations in the apparatus). When the matrix has been completed, the values of each

Self-Directing Optimization Matrix for
Less Than Seven Variables. (Chemtech, August 1980, p.494.)

	x_1	x_2	x_3	x_4	x_5	x_6	x_7
A	Low	Low	Low	Low	High	High	High
B	High	Low	Low	High	High	Low	Low
C	Low	High	Low	High	Low	High	Low
D	High	High	Low	Low	Low	Low	High
E	Low	Low	High	High	Low	Low	High
F	High	Low	High	Low	Low	High	Low
G	Low	High	High	Low	High	Low	Low
H	High	High	High	High	High	High	High

TABLE 2.2.1 Optimization Matrix

variable, such as temperature and run time, from 'good' runs (ie: in the filament work, the runs which produced the straightest, thinnest, longest filaments) are summed and averaged and multiplied by 2. From these new values, the values from the 'worst' run are subtracted. This is done for each run that has a produced inadequate filaments, or more precisely, received a rating below some set standard. The final derived values are now the new variable values for the next run. This procedure continues until the boundaries are brought close enough together to give the optimum running conditions. This statistical approach cannot give nearly as much information as could be obtained from doing 2^n (n-variables) experiments, but it is a quick method for optimizing reaction conditions (or for finding out whether the experiment is being run outside of its boundaries). It also satisfies an important requisite of any group of experiments; ensuring, with confidence, that the results are caused by programmed changes and not by chance.

A-Runs

The first series of experiments is labelled matrix A. A listing of the first 8 experiments and their conditions is shown in Table 2.2.2. Subsequent experiments (A9 through A11) were formulated by the SDO

Parameter Limits:

- 1) Nickel Deposition (50-500 Å)
 2) Ramp Rate (5-25 °C/min)
 3) Run Temperature (600-1000 °C)
 4) Run time (5-30 minutes)
 5) Total Flow Rate (40-400 sccm)
 6) H₂:HC Ratio (3:1-50:1)
- All Runs: P= 1 atm (~640 Torr)
 HC= Acetylene
 Ni evaporated on
 Poco Graphite

EXP.	DATE	Variables						Ratings					
		(1)	(2)	(3)	(4)	(5)	(6)	DIAM.	LENGTH	A.R.	STRAIGHT	OVERALL	
A1	7/13	-	-	-	-	+	+	10	1	1	3	5	4
A2	8/5	-	+	+	-	+	-	1	1	1	5	7	3
A3	8/15	-	+	-	+	-	+	7	4	5	2	5	4.6
A4	8/18	-	-	+	+	-	-	6	2	2	5	1	3.2
A5	9/15	+	-	+	-	-	+	0	0	0	0	0	0
A6	9/15	+	-	-	+	+	-	7	3	3	5	8	5.2
A7	9/17	+	+	-	-	-	-	8	3	3	3	6	4.6
A8	9/19	+	+	+	+	+	+	6	3	4	5	1	3.8

TABLE 2.2.2 Runs A1-A8 Summary of Conditions and Ratings

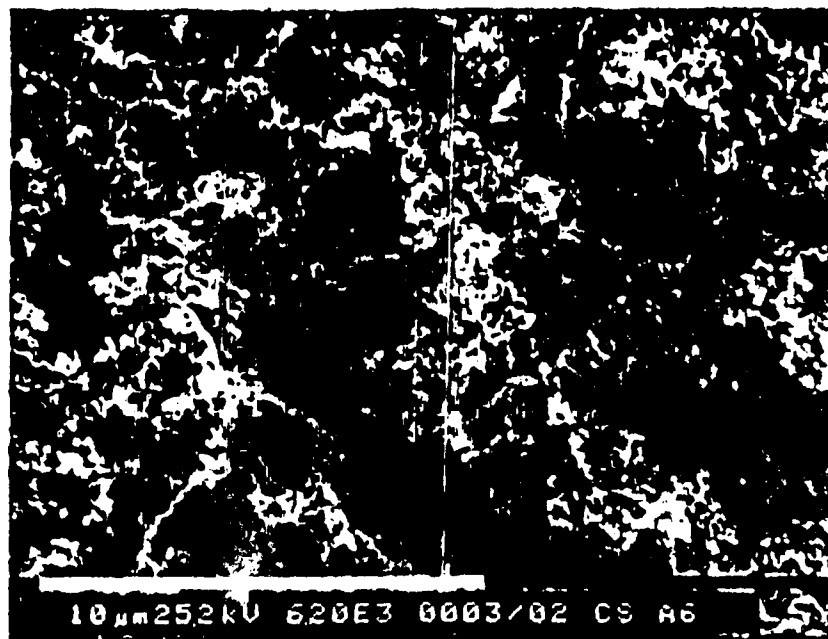


FIGURE 2.2.4 Sample A6 Carbon Filaments



FIGURE 2.2.4 Sample A6 Carbon Filaments

method mentioned earlier. 'Best' and 'worst' runs were determined by a rating system which is experimentally biased to some extent ("tendentiousness of experimenter"³ in analyzing micrographs). Runs A1 through A8 were rated from 1-10 in five different categories: diameter [1=1 μ m, 10=0.01 μ m], length [1=0.001mm, 10=1mm], aspect ratio [1=1, 10=10,000], straightness [1=smokey, 3=indistinguishably tangled, 5=tangled, 7=not tangled, 10=straight as an arrow], and density [1=1 filament, 5=scattered areas of growth, and 10=growth everywhere]. The latter is not really priority for this research, but as it deals somewhat with consistency, it is important in reproducibility of the methods. The overall rating of 1-10 is an average over these five categories. The highest rating given for runs A1 through A8 was a 5.2 (not very encouraging!) for run A6 (see Figure 2.2.4). Using the SDO statistical method, runs A2, A4, and A5 were discarded for having a rating of less than 3.5. By throwing out these three runs, three more runs (A9, A10, and A11) were created by using the average, 2x average, minus 'worst' run technique. All of the three new runs pointed in the direction of a lower temperature (360°C). Only A11 produced a filament. The diameter was on the order of nanometers (lowest limit of filament growth) but twisted. The three new runs produced essentially nothing,

and therefore it was concluded that the initial matrix was not bounded correctly or that possibly it is nearly impossible to achieve straight, submicron, high aspect ratio carbon filaments by CCVD with nickel on graphite, and acetylene. See Table 2.2.3 for conditions and results of the full A matrix. From the results (as analyzed by SEM) of matrix A, the most apparent observation is that high temperatures (1000°C- the upper bound on run temperature) are unfavorable. A longer run time (30 as opposed to 5 minutes) was determined to be favorable: The two low temperature longer reaction time runs being ranked #1 and tied for #2, and the low temperature and short reaction time runs being ranked as tied for #2, and #3. All of the low temperatures received the highest rankings in the diameter category (smallest diameters) which indicates that as the temperature increases the filaments begin to thicken, or else the nucleation period of growth may be significantly different at the two temperatures (for example, more agglomeration of catalyst particles at higher temperatures, producing thicker filaments from the start).

Since this matrix may not have been bounded correctly, as it pointed towards lower temperatures, and this was not successful, it was decided to work at the high temperature limit of 1000°C. This seemed to be

RUN	DATE	NI DEP. (Å)*	RAMP (°/min)	RUN T (°C)	RUN t (min)	TOT. FLOW (sccm)	H ₂ :HC	COOLING GAS	COMMENTS
A1	7/13	25	5	600	5	204	50:1	H ₂	Short filaments, d=.06um, l=.4um.
A2	8/5	25	25	1000	2.5	200	1:1	H ₂	No filaments; looks like start of growth.**
A3	8/15	25	25	600	30	53	50:3	H ₂	'Smokey' filaments, d:.05-.4um, AR>100.
A4	8/18	25	5	1000	10	40	5:1	H ₂	Few filaments, d=.4um, short.**
A5	9/15	100	5	1000	5	40	40:1	He	Nothing.**
A6	9/15	100	5	600	30	200	3:1	H ₂	Tangled filaments, d: .15-1.0um, l>10um.**
A7	9/17	100	25	600	5	40	3:1	He	Bundles of tangled filaments, d=0.1um
A8	9/19	100	25	1000	30	200	50:1	He	Few filaments, d=.4um, l=50um. Not straight.
A9	9/23	100	4	360	37	76	61:1	H ₂	Nothing.
A10	9/24	100	20	360	10	200	57:1	H ₂	Nothing.
A11	9/24	100	4	360	35	147	12:1	H ₂	One filament, d<.01um.**

* estimated deposit

** carbon deposits on reactor

TABLE 2.2.3 A-RUNS

reasonable, since long, straight filaments are produced by Endo et. al.⁴ at higher temperatures ($>1000^{\circ}\text{C}$) using benzene and a metalorganic catalyst. Unfortunately, his experimental details are not detailed enough to reproduce them in this laboratory. So the next step in our experimental design was to define a new matrix by examining a variety of run techniques at higher temperatures.

B-Runs

The runs labelled B are not in a matrix form. These runs are preliminary work to examine possible run parameters in order to achieve long, straight, submicron carbon filaments. A table of all B runs to date is shown in Table 2.2.4. The major difference between A runs and B runs is a shortened reduction time. All runs in the A matrix were heated to the final run temperature in hydrogen. It is possible that no or few filaments were found in the high temperature A runs because all, or most, of the nickel catalyst could have diffused into the graphite substrate. All substrates used were Poco type, so nickel was evaporated on a variety of carbon planes, much of it easily accessible to the C-axis where diffusion will be much more rapid than on/through the basal surface. Reduced nickel (in its zero valence state) has a much higher

RUN	DATE	SUBST.	NI DEP. (Å) *	RAMP (C/min)	RUN T (C)	RUN t (min)	TOT. FLOW (sccm)	H ₂ :HC	RED. T (C)	RED. t (min)	COOL. GAS	HC and HC SAT. t (min)	COMMENTS
B1	10/1	Poco	100	10	1000	60	40	5:1	1000	10	He	C ₂ H ₂ /0.5	Strt. filaments, d:5-6um, AR<50.**
B2	10/5	SiO ₂	?	10	1000	60	40	5:1	1000	10	He	C ₂ H ₂ /1.0	No SEM.**
B3	10/8	Poco	500 (plated)	10	1000	60	40	5:1	1000	10	He	C ₂ H ₂ /0.5	One filament. d=.6um AR<20.**
B4	10/13	Poco	100	10	1000	60	40	5:1	1000	10	He	C ₂ H ₂ /1.0	See B1.
B5	10/13	Poco	100	10	1000	60	40	5:1	1000	10	He	C ₂ H ₂ /0	See B1.
B6	10/21	HOPG	50	10	1000	60	40	5:1	1000	10	He	C ₂ H ₂ /0.75	Octop. filaments, d: .2-.5um, AR<100.**
B7	10/22	HOPG	50	10	1000	60	40	5:1	1000	10	He	CH ₄ /1.0	Nothing.
B8	10/24	Poco	100	10	1000	60	40	5:1	1000	10	He	CH ₄ /1.0	Nothing.
B9	11/3	HOPG	100	10	1000	180	40	5:1	1000	15	He	CH ₄ /1.0	Nothing.
B10	11/5	HOPG	100	10	1000	60	126.5	10:1	1000	10	He	C ₂ H ₂ /1.0	Nothing.
B11	11/5	HOPG	100	10	1030	15	126.5	10:1	1030	10	He	C ₂ H ₂ /1.0	Nothing.**
B12	11/9	HOPG	100	10	1030	60	126.5	10:1	1030	10	He	C ₂ H ₂ /1.0	Nothing.**
B13a	11/11	HOPG	100	?	1100	60	136.6	8.8:1	→1100	?	H ₂	C ₂ H ₂ /0	Nothing.
B13b	11/11	HOPG	100	?	1100	60	136.6	2.5:1	→1100	?	H ₂	C ₂ H ₂ /0	Nothing.
B14	11/10	HOPG	100	10	1000	60	126.5	10:1	1000	10	Ar	C ₂ H ₂ /1.0	Nothing.**
B15	11/14	HOPG	100	10	850	60	126.5	10:1	850	10	He	C ₂ H ₂ /1.0	Bundles of fila- ments, d=.2um, long.**

* estimated deposit

** carbon deposits on reactor

TABLE 2.2.4 B-RUNS

diffusion rate than unreduced nickel.⁵ The reduction time was therefore reduced from total heat up time (usually greater than one hour for a run temperature of 1000°C) to 10 minutes. 10 minutes should be sufficient time for the reduction of all of the catalyst. A longer reduction period of 15 minutes was also used for one run (B8) and there was no observable difference in the results (somewhat inconclusive for only one run, but still confident with 10 minutes).

Another change in the run procedure was the inclusion of a hydrocarbon saturation period. Only hydrocarbon and the inert (to keep total flow constant) were run at this time, which followed the reduction period. The purpose of a hydrocarbon saturation period is to form a carbide at the catalyst surface initially, which should enhance filament growth (following Sacco et. al.⁶). Two comparison runs, B4 and B5, were made. All conditions were identical in both runs with the exception that B4 had a 1 minute saturation period, whereas B5 had none. Nothing conclusive could be extrapolated from the results, as both produced very few filaments. The only encouraging information was that slightly longer filaments were grown in B4 (with the saturation period), indicating the possibility of an enhanced rate of growth. No further investigation has been conducted to optimize or exclude the hydrocarbon

saturation period.

During the B runs, the use of a different hydrocarbon was examined. Many people (most notably Baker⁷) have denounced the use of methane as a possible decomposition precursor to filament growth. Although most arguments accuse impurities as the source of filaments when they have been grown using methane, Keep et. al.⁷ has attributed it to the decomposition of secondary unsaturated hydrocarbons, which are strictly the result of methane-hydrogen reactions. The conditions used in the methane experiments (runs B7, B8, and B9) were similar to those used in the acetylene runs (see Table 2.2.4) except that run time was increased in one of them up to 3 hours. No filaments were obtained in any of these samples. Without any of Keeps experimental data, it is difficult to compare with his results, but assuming that the system is without impurities, it is tempting to conclude that Bakers' theory still holds. No further attempts have been made to grow carbon filaments using methane.

Another attempt to eliminate the problem of possible nickel diffusion into the substrate at high temperature, was to change the type of graphite substrate. Poco graphite was replaced by single crystal graphite or highly oriented pyrolytic graphite (HOPG) as the substrate.

Nickel was evaporated onto these substrates, which were 'peeled' off of a single block of graphite. Surfaces were prepared in the same manner as mentioned earlier in the previous section. The chips that were peeled off did not seem to have very uniform surfaces (although all quite different from the Poco graphite). A new shipment of HOPG chips with very uniform surfaces has just been received from Union Carbide (generously donated by Arthur Moore). These samples still need to be prepared before running, but hopefully they will serve as a good comparison to the HOPG now used. The first run made with a HOPG substrate (nickel evaporated), B6, gave more filament growth than did other runs with similar conditions using Poco graphite (B1, B4, and B5). Increasing the temperature from 1000 to 1030°C (still within a critical range where no thickening should occur⁸) produced no filaments on the HOPG substrates. Increasing the hydrogen to hydrocarbon ratio from 5:1 to 10:1 and increasing the total flow rate from 40 to 126.5 sccm also produced no filaments.

One run in the B series was made to determine the effects of the inert used. Argon was used instead of helium for run B14, as one colleague suggested, that helium will carry many more impurities into the system than will argon. No filaments were obtained by SEM analysis

on this sample. This indicates that the lack of filaments in these runs is not associated with the type of inert used. There is probably no growth at all, and not the case that growth is being destroyed by the introduction of oxygen, for example, at elevated temperatures.

Two runs, B13a and B13b, were run in the old furnace set up as was used by McKenney and Bowers in this research in previous years. This was done as an inquiry to the effects of impurities. No filaments were found on these samples- but they were also made at 1100°C, which is beyond the limits that have been used in the high vacuum system, and seems to be beyond the limits of filament growth.

The last run in the B series of experiments was B15. B15 was run at 850°C using an HOPG substrate. There was a lot of filament growth on the substrate, and the filaments had diameters of about 0.2 μm . It was difficult to determine any lengths, as growth occurred in 'bundles' (very tangled). (See Figure 2.2.5). The results of this run indicate that the previous B experiments were run at a temperature ($>1000^\circ\text{C}$) which is beyond the limit of mass filament growth. This 850°C run, however, grew uncontrollable filaments. Perhaps the region between 850 and 1000°C includes an optimum growth temperature, where solitary filaments, ie: more than one but not in bundles, will grow straight and controllably.

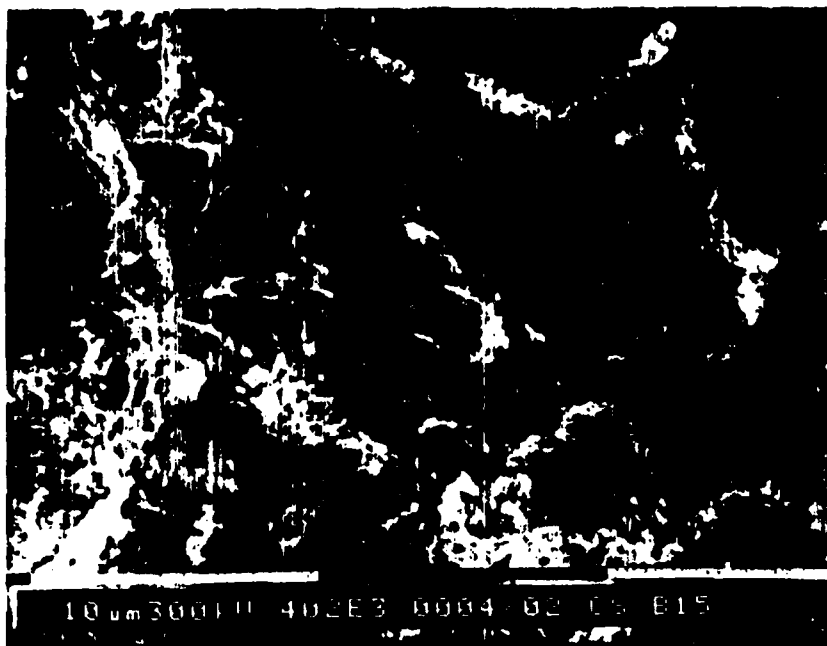


FIGURE 2.2.5 Sample B15 Carbon Filaments

Conclusions

The ultimate goal of the CCVD filament research at this stage, to grow straight, submicron, high aspect ratio filaments, has not yet been achieved. A variety of growth conditions have been examined, based almost entirely on the decomposition of acetylene over an evaporated nickel catalyst. From the results of these experiments, or rather lack of, it may be futile to continue with acetylene and/or nickel as the main ingredients for filamentous growth, as they might never be able to produce the type of filament that is desired. The straightest and most distinguishable filaments grown have been made at high temperatures (1000°C). This, however, produced very little filament growth and quite a lot of carbon deposits on the reactor walls. The deposits ranged from yellowish-brown tints to very shiny black (pyrolytic carbon) and have given off a variety of aromas from eau de dead fish to moth balls. There are obviously many reactions occurring at the higher temperatures, and these reactions are probably diminishing the amount of reaction to produce carbon filaments.

The next stage of the research will involve the use of different materials, most likely benzene as the hydrocarbon and an iron catalyst. Itoh et. al.² has been able to grow the type of filaments that are

desired using benzene and iron, but his work is not well defined and will be difficult to reproduce. There are many details which are unknown, but it is hoped that these can be found with future investigations using the CCVD system that has been built.

REFERENCES

1. M. Egashira, H. Katsuki, Y.Ogawa, and S. Kawasumi, Carbon, 21 (1), (1983). pp.89-92.
2. C.D. Hendrix, Chemtech, August (1980). pp.486-497.
3. J.M. Thomas, Chemistry and Physics of Carbon (P.L. Walker Jr.,ed.), Vol.1, Dekker, New York, 1965.
4. M. Endo, Y. Hishiyama, and T. Koyama, J. Phys. Chem. Appl. Phys., 15 (1982). pp.353-363.
5. I.L. Spain, private communication.
6. A. Sacco Jr., P. Thacker, T.N. Chang, and A.T.S. Chiang, J. of Catalysis, 85 (1984). pp.224-236.
7. R.T.K. Baker and P.S. Harris, Phys. Chem. Carbon, 14, (1978). pp.83-105.
8. I.L. Spain, M.L. Dresselhaus, to be published.

II-3. TEMPERATURE DISTRIBUTIONS IN A CATALYST PELLET IN CCVD OF CARBON

Sulagna Chatterjee and Dr. Carol M. McConica
Department of Agricultural and Chemical Engineering
Colorado State University, Fort Collins, CO 80523.

Introduction

The purpose of this work is to study the temperature distributions in a growing carbon filament formed during catalytic chemical vapour deposition. When a hydrocarbon gas is passed over a nucleated catalyst surface, carbon is deposited. Carbon deposits in the form of filaments, carrying the metal catalyst particle at their free ends. The major factors that affect the temperature changes in the catalyst particle are

- i) The heat generated due to chemical reaction on the exposed catalyst surface.
- ii) The heat radiated out from the exposed catalyst surface to the gas phase.
- iii) The heat conducted away from the catalyst particle to the carbon filament.

The Mathematical Model

A rigorous heat balance over the metal catalyst particle takes into account the convection and conduction effects to the gas phase and the convection effects into the carbon filament. A time varying linear differential equation has been developed which takes account of these effects. Since this equation becomes very complicated, simplifications were made based on the reaction conditions.

From the law of conservation of thermal energy over a control volume element :

$$\begin{aligned} \text{Heat flux in} - \text{Heat flux out} + \text{rate of generation of heat} \\ \text{in the control volume} \\ = \text{rate of accumulation of heat} \\ \text{in the control volume} \end{aligned}$$

For the catalyst particle this leads to : (Fig.1)

$$\Delta H_{rxn} = \frac{\sigma(T^4 - T_a^4)}{1/e_1 + A_1/A_2(1/e_2 - 1)} - h(T - T_a) - k_g \left. \frac{dT}{dr} \right|_{r=R} - H_{int} = \frac{4}{3} r^3 \rho C_{p,m} \frac{dT}{dt} \quad (1)$$

where H_{int} is the heat flow across the carbon-iron interface.

The following assumptions were made in developing eqn(1) :

- a) The catalyst particle were assumed to be spherical when, in reality, they are pear shaped.
- b) There are no temperature distributions in the catalyst particle itself.
- c) The filament diameter is the same as the catalyst particle diameter. This holds for initial growth periods.

For the reaction conditions cited by Baker in CAEM[1], the simplifications were used :

- d) The convective and conductive effects to the gas phase were negligible compared to radiative effects. This is especially valid since the CAEM technique uses a vacuum reaction chamber.
- e) The area of the catalyst particle, exposed to the gas phase is very small compared to the area of the reactor walls. Hence $A_1/A_2 \rightarrow 0$.
- f) The products formed by the decomposition of acetylene have negligible amount of hydrogen. This has been experimentally tested.
- g) Thermal steady state is achieved.
- h) Mass transfer steady state is achieved.

Calculation of the reaction rate:

- 1) The hydrocarbon used in reference [1] is acetylene,
- 2) The metal used is iron,
- 3) The substrate used is graphite.

From reference [2] the rate of growth of carbon filaments was found to be a function of temperature as :

The rate of filament growth(R_g) = $79594.478 \exp(-9212/T)$ nm/sec

Since we are assuming mass transfer steady state,

The rate of chemical reaction, $r_{rxn} = KR_g$,

i.e, $r_{rxn} = 7.283 \times 10^{-4} \exp(-9212/T)$ g moles/sq.cm sec

where $K = (4\pi r^2)/2\pi r^2$

Calculation of the heat flux across the carbon iron interface

H_{int}:

From the assumption of thermal steady state:

Heat flux across the carbon-iron interface = heat flux across the filament

$$\text{Hence from eqn(1), } H_{int} = -k_c \frac{dT_c}{dx} \text{-----(i)}$$

$$\text{and } R_g = \frac{dx}{dt} \text{-----(ii)}$$

where the coordinate x is the linear distance along the direction of filament growth as shown in Fig.1b.

From (ii) it is clear that $dx = R_g dt$ and substituting the value of dx in eqn(i);

$$k_c \frac{dT_c}{dx} = k_c \frac{dT_c}{dt} \text{-----(iii)}$$

where dT_c is the change in temperature of the carbon filament. Also, from the steady state assumption,

$$dT_c = \frac{C_{p,m}}{C_{p,c}} dT$$

Substituting the value of dT_c in eqn(iii)

$$H_{int} = k_c \frac{dT}{dx} = \frac{C_{p,m}}{C_{p,c}} \frac{dT}{dt} k_c R_g$$

Calculation of the heat of reaction:

The heat of reaction is calculated using the following equation :

$$\Delta H = \Delta H_{298} + A(T-298) + (B/2)(T^2-298^2) + (C/3)(T^3-298^3)$$

where $C_{p,g}dT = (A + BT + CT^2)dT$

and the gas phase is considered to be acetylene by simplification(f).

Substituting the above expressions and making the necessary simplifications in eqn(1) :

$$\frac{2r_m}{3} C_{p,m} + \frac{k_c}{R_g} \frac{C_{p,m}}{C_{p,c}} \frac{dT}{dt} = \left[\Delta H_{298} + A(T-298) + \frac{B(T^2-298^2)}{2} + \frac{C(T^3-298^3)}{3} \right] r_{rxn} - \sigma e(T^4 - T_a^4) \text{-----(2)}$$

Results

The equation(2) is a first order nonlinear differential equation which was solved numerically on the computer, using a third order Runge-Kutta method. The data used for the several constants used in equation(2) are as follows[4] ;

The heat of reaction at 25 °C for the decomposition of acetylene is 54194 cal/g mole.

The emissivity of iron oxide is 0.85 to 0.89

To calculate the specific heat of various elements :

For acetylene in a temperature range of 298-1500 K

$C_p = 7.331 + 12.622 \times 10^{-3}T - 3.889 \times 10^{-6}T^2$ cal/deg mole

For carbon in a temperature range of 273-1373 K

$C_p = 2.673 + 0.002617T - (116900/T^2)$ cal/deg mole

For α -iron in a temperature range of 273-1041K

$C_p = 4.13 + 0.00638T$ cal/deg mole

For a filament of diameter 140 nm the temperature distribution with time was calculated. Over a time of 40 secs., which is the time of growth cited in [1], the temperature was found to be more or less constant. In effect, the temperature change is of an order of magnitude less than 10^{-6} at the temperature of 1000 K.

Conclusion

The results are directly related to the underlying assumptions. The reaction rate was assumed to be in equilibrium with the diffusion rate of carbon through the catalyst particle. If this were so, there would be no surface coverage of the catalyst particle and the gas phase reaction would not stop in such a short time.

Also, there could be some poisoning effect that retards the reaction. Since the actual mechanism of the gas phase reaction is unknown, it was impossible to take account of these effects.

Future Work

It would be worthwhile to model the system for the unsteady state process, when the intrinsic chemical reaction rate far exceeds the rate of diffusion through the catalyst particle. This would lead to a temperature rise in the catalyst particle, which would trigger off more reaction, and thus more deposition of carbon. This would lead to full surface coverage of the catalyst particle and thus the reaction sequence would stop. Thus, a steady state is never reached.

For the proposed mechanism, it is necessary to find the true reaction rate on the nickel surface. The reaction rates, cited in literature are calculated from the amount of carbon deposited on the metal catalyst. A thorough search for the intrinsic chemical reaction rate is still underway.

Nomenclature

- e_1, e_2 = The emissivities of the metal catalyst, the reactor walls respectively.
- A_1, A_2 = The exposed area of the metal catalyst, the area of the reactor walls respectively in sq.cms.
- T, T_a = temperature of the metal catalyst, temperature of the ambient gas phase respectively in K.
- k_c, k_g = The thermal conductivities of the carbon and gas phase respectively in cal/cm sec K.
- ρ_m, ρ_c = The densities of the metal and carbon respectively in moles/c.c.
- $C_{p,m}, C_{p,c}$ = The specific heat capacities of the metal and carbon respectively in cal/mole K
- σ = The Stefan - Boltzmann constant in cal/sq.cm sec K^4
- h = Coefficient of convective heat transfer to the gas phase in cal/sq.cm K.

References

1. Baker et.al., Journal of Catalysis 30, 86-95(1973).
2. XVIIth Biennial Conference on CARBON Pg. 156, 19-24 July 1987.
3. Perry and Chilton, Chemical Engineer's Handbook 5th edition.

C-----

C NOV. 8, 87

C-----

C

```

COMMON TA,H,TIMI
READ(*,*)TA,H,TIMI
T=TA
TIM=TIMI
PRINT*, 'TIME(SECONDS)    TEMPERATURE(KELVIN)'
PRINT*, ' '

```

```

55  R1=H*FUNC(T)
    IF(ERROR.EQ.-1) GOTO 99
    X1=TIMI+0.5*H
    Y1=T+0.5*R1
    R2=H*FUNC(Y1)
    IF(ERROR.EQ.-1) GOTO 99
    X2=TIMI+H
    Y2=T-R1+(2.0*R2)
    R3=H*FUNC(Y2)
    IF(ERROR.EQ.-1) GOTO 99
    T=T+(1.0/6.0)*(R1+4.0*R2+R3)
    IF(T.LT.0)GOTO 98
    print*,tim,t
    TIM=TIM+H
    IF(TIM.GE.50)GO TO 10
    GO TO 55
98  PRINT*, 'TEMPERATURE NEGATIVE : EXECUTION TERMINATED'
99  PRINT*, 'DIVIDE BY ZERO ERROR : EXECUTION TERMINATED'
10  STOP
    END

```

```

REAL FUNCTION FUNC(T)
COMMON TA,H,TIMI
ERROR=0
A1=0.2129*EXP(9212.0/T)
if(t.eq.0.0)ERROR=-1
if(error.eq.-1) goto 100
A1=A1/(2.673+.002617*T-116900.0/(T**2))
A1=A1*(4.13+.00638*T)
A=(4.13+.00638*T)*6.517E-07
A=A+A1
F1=54194.0+7.331*(T-298.0)
F1=6.311E-03*(T**2-298.0**2)+F1
F1=-1.296E-06*(T**3-298.0**3)+F1
F1=F1*7.283E-04*EXP(-9212.0/T)
F2=1.2E-12*(T**4-TA**4)
FUNC=F1-F2
FUNC=FUNC/A
RETURN
END

```

100

C-----

INITIAL TEMPERATURE OF THE CATALYST PARTICLE = 800 K

TIME WHEN GROWTH STARTS = 10 SECS

TIME WHEN GROWTH STOPS = 50 SECS

TIME(SECONDS) TEMPERATURE(KELVIN)

10.000000	800.000000
11.000000	800.000000
12.000000	800.000000
13.000000	800.000000
14.000000	800.000000
15.000000	800.000000
16.000000	800.000000
17.000000	800.000000
18.000000	800.000000
19.000000	800.000000
20.000000	800.000000
21.000000	800.000000
22.000000	800.000000
23.000000	800.000000
24.000000	800.000000
25.000000	800.000000
26.000000	800.000000
27.000000	800.000000
28.000000	800.000000
29.000000	800.000000
30.000000	800.000000
31.000000	800.000000
32.000000	800.000000
33.000000	800.000000
34.000000	800.000000
35.000000	800.000000
36.000000	800.000000
37.000000	800.000000
38.000000	800.000000
39.000000	800.000000
40.000000	800.000000
41.000000	800.000000
42.000000	800.000000
43.000000	800.000000
44.000000	800.000000
45.000000	800.000000
46.000000	800.000000
47.000000	800.000000
48.000000	800.000000
49.000000	800.000000

Stop - Program terminated.

INITIAL TEMPERATURE OF THE CATALYST PARTICLE = 900 K

TIME WHEN GROWTH STARTS = 10 SECS

TIME WHEN GROWTH STOPS = 50 SECS

TIME(SECONDS) TEMPERATURE(KELVIN)

10.000000	900.000000
11.000000	900.000000
12.000000	900.000000
13.000000	900.000000
14.000000	900.000000
15.000000	900.000000
16.000000	900.000000
17.000000	900.000000
18.000000	900.000000
19.000000	900.000000
20.000000	900.000000
21.000000	900.000000
22.000000	900.000000
23.000000	900.000000
24.000000	900.000000
25.000000	900.000000
26.000000	900.000000
27.000000	900.000000
28.000000	900.000000
29.000000	900.000000
30.000000	900.000000
31.000000	900.000000
32.000000	900.000000
33.000000	900.000000
34.000000	900.000000
35.000000	900.000000
36.000000	900.000000
37.000000	900.000000
38.000000	900.000000
39.000000	900.000000
40.000000	900.000000
41.000000	900.000000
42.000000	900.000000
43.000000	900.000000
44.000000	900.000000
45.000000	900.000000
46.000000	900.000000
47.000000	900.000000
48.000000	900.000000
49.000000	900.000000

Stop - Program terminated.

INITIAL TEMPERATURE OF THE CATALYST PARTICLE = 1000K

TIME WHEN GROWTH STARTS = 10 SECS

TIME WHEN GROWTH STOPS = 50 SECS

TIME(SECONDS) TEMPERATURE(KELVIN)

10.000000	1000.000000
11.000000	1000.000000
12.000000	1000.000000
13.000000	1000.000000
14.000000	1000.000000
15.000000	1000.000000
16.000000	1000.000000
17.000000	1000.000000
18.000000	1000.000000
19.000000	1000.000000
20.000000	1000.000000
21.000000	1000.000000
22.000000	1000.000000
23.000000	1000.000000
24.000000	1000.000000
25.000000	1000.000000
26.000000	1000.000000
27.000000	1000.000000
28.000000	1000.000000
29.000000	1000.000000
30.000000	1000.000000
31.000000	1000.000000
32.000000	1000.000000
33.000000	1000.000000
34.000000	1000.000000
35.000000	1000.000000
36.000000	1000.000000
37.000000	1000.000000
38.000000	1000.000000
39.000000	1000.000000
40.000000	1000.000000
41.000000	1000.000000
42.000000	1000.000000
43.000000	1000.000000
44.000000	1000.000000
45.000000	1000.000000
46.000000	1000.000000
47.000000	1000.000000
48.000000	1000.000000
49.000000	1000.000000

Stop - Program terminated.

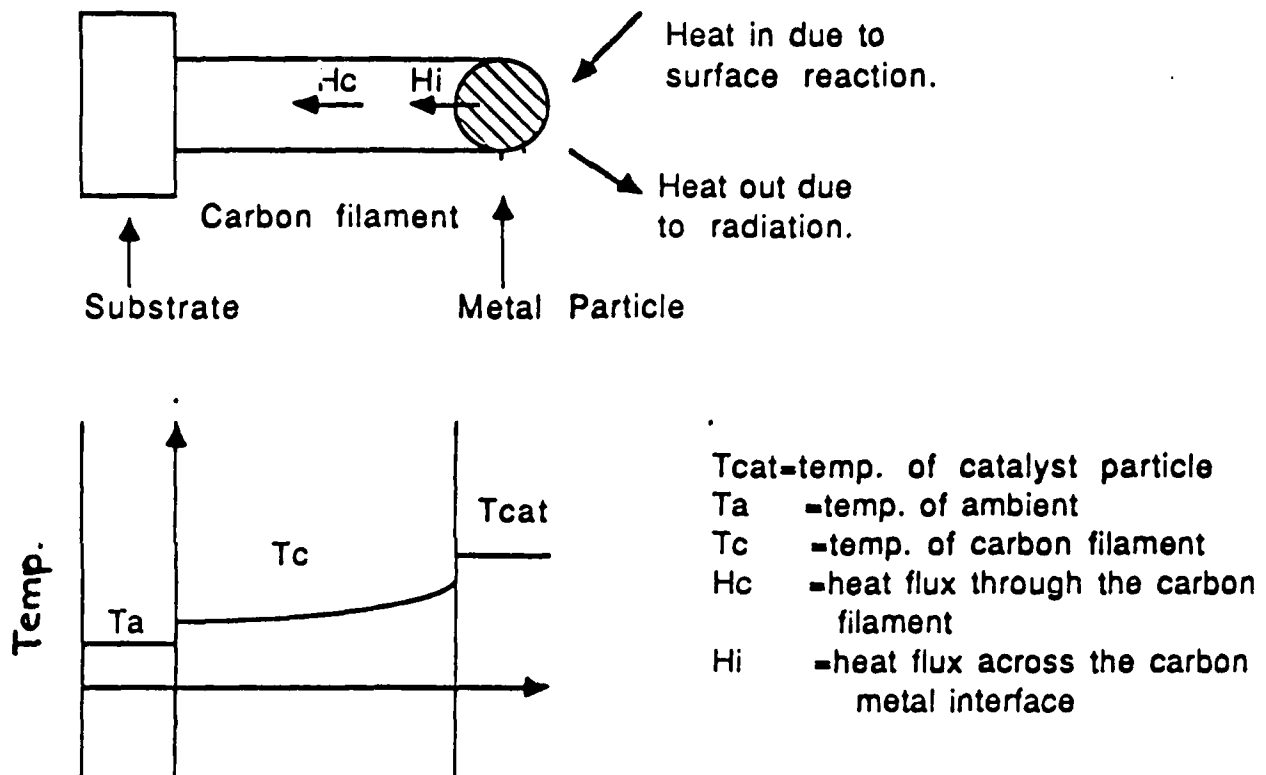


Fig.1: Temperature distributions in a growing carbon filament with the metal catalyst at its tip.

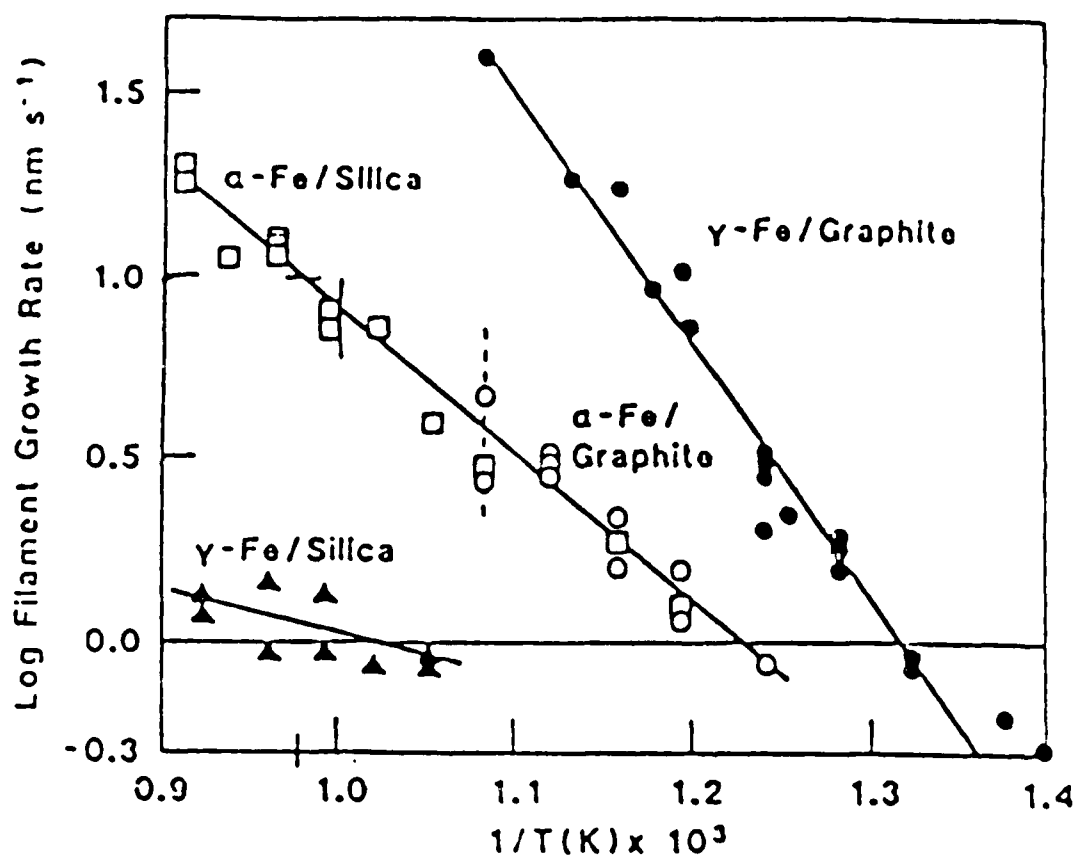


Fig. 1 : Arrhenius plot showing the variation of the growth rate of carbon filament with temperature for α -iron catalyst.(2)

II-4. SILICON AND GRAPHITE SUBSTRATE PREPARATION

Joseph R. Pollara
Department of Chemical Engineering
Colorado State University
Fort Collins, CO 80523

ABSTRACT:

It is the purpose of this work to develop new methods of depositing nickel and iron onto substrates for CCVD. Ion exchange of nickel onto oxidized single crystal silicon resulted in no filament growth. The gas phase decomposition of nickel carbonyl to give nickel particles was considered undesirable because of the toxicity of the gases. The electrolytic plating of iron onto graphite results in flocculant deposition. The most effective method of substrate preparation thus far, is direct submersion of the graphite into iron solutions.

INTRODUCTION:

The time consuming process of high vacuum evaporation led to the investigation of new methods of substrate preparation. The alternatives under consideration are ion exchange, nickel carbonyl decomposition, electrolytic plating and submersion. Both nickel and iron substrates are being prepared because acetylene was found not to give filaments at high temperatures on nickel. It is hypothesized that the nickel is the cause of no filament growth and a comparison of catalysts is necessary.

PROCEDURE:

The primary surface used to prepare silicon substrates has been silicon wafers manufactured by AUREL[™]. The average silicon dioxide thickness on the surface of the wafer is approximately 10,000 angstroms. The first investigated method of preparation is a modification of Benesis', et al., paper (1) on preparing catalysts by an ion-exchange method. Although the reaction involved does not strictly follow the definition of an ion-exchange it best describes the chemistry of the system. The desired catalyst to be deposited is nickel and will originate from a hexamine nickel(II) solution.

The method of ion-exchange consists of fixing metal cations by exchange with ions on the surface of an oxidized silicon wafer. Using nickel as the metal cation source the method makes use of the exchange of $\text{Ni}(\text{NH}_3)_6^{2+}$ with silica. The generic formula follows:

- 1) Add 29.9 g $\text{Ni}(\text{NO}_3)_2 \cdot 6\text{H}_2\text{O}$ to 100 ml. doubly distilled water. (Ni stock)
- 2) Add 10 ml. of Ni stock to 90 ml. of $\text{NH}_4\text{OH}:\text{H}_2\text{O}(1:1)$. (hexamine nickel(II) solution).
- 3) Add variable amount of hexamine nickel(II) solution to 100 ml. of $\text{NH}_4\text{OH}:\text{H}_2\text{O}$ to alter weight loadings. This mixture is the reaction bath.
- 4) Add silica wafer to reaction bath.

In step 4 two groups of silica wafers were prepared. One group of wafers were scribed using a diamond scribe, and the other group were left smooth. Each group was then subjected to various parameter changes. More specifically, the temperature, residence time in the reaction bath and weight loading of hexamine nickel(II) solution were run in excess individually in three different runs for each group of wafers. In this particular set of experiments two baths were prepared following the generic recipe for preparation.

Another proposed method was to use a nickel carbonyl gas in a reaction chamber at high temperatures. The nickel is deposited onto the surface by the decomposition of Ni Carbonyl to solid nickel and carbon monoxide. Although this method is very controlled and well suited to the needs of this experiment the hazardous nature of nickel carbonyl makes it an undesirable alternative.

In order to determine if growth on an iron substrate in acetylene was at all possible a submersion process was performed. A number of graphite chips were soaked in an aqueous solution of ferrous chloride($\text{FeCl}_2 \cdot 4\text{H}_2\text{O}$) for 1 - 3 hours, rinsed and dried overnight in an oven at 71°C .

The method presently being investigated is an electrolytic deposition onto Union Carbide Highly Oriented Pyrolytic Graphite (UC HOPG) using a modified iron plating bath (Figure 1). Once it was found that there was a possibility of growth on iron substrates a more controlled sequence of experiments were prepared. Using a modification of an iron plating process found in a book by Blum and Hogaboom (2) a bath was prepared using this general recipe:

- 1) Add 450 grams $\text{FeCl}_2 \cdot 4\text{H}_2\text{O}$ to 1 litre of doubly distilled water.
- 2) Add 4 ml. of .01N HCL.
- 3) Add small amount (quantity not crucial) of KCL.

A current of approximately 20 milliamps and 1.4 volts was run through the bath using a copper wire as the anode. Two chips were prepared in this manner; the first being plated for twenty seconds and the second for one minute. Table 1 illustrates the conditions of plating as well as an indication of whether growth has occurred.

ELECTROLYTIC PLATING OF IRON ONTO UC HOPG

TABLE 1

date prepared	sample #	time	current	volts	growth
12/10	C5	20 s	20mA	1.4V	none
12/10	C6	60 s	20mA	1.4V	none

RESULTS:

The method of ion-exchange produced no substantially enlightening results except that silicon wafers do not grow carbon filaments. The first bath (100 ml) run at excess temperature held a temperature of approximately 60°C. The second bath (250 ml) was run between 48-52°C. The scribed group of wafers were all broken in the baths during preparation because of the harsh stirring conditions of the reaction bath. The scribed group of wafers produced no carbon filament growth. The runs made with excess hexamine nickel(II) solution were prepared with 3.2 ml. and 5.0 ml. in the 100 ml. and 250 ml. baths, respectively. One scribed wafer was broken and the rest produced no carbon growth. The last parameter change executed was to run excess residence time in the baths. Each set of wafers were exposed in the reaction baths for six hours. No stirring was present in order to prevent wafer breakage. These wafers also produced no carbon filament growth. Upon finding no growth from this method Dr. Steven Thompson of the Chemistry department at Colorado State University was consulted. It became apparent that the surface chemistry of the silica wafers prevented any growth from occurring. The near perfect configuration of the silanol on the wafer surface restricts the exchange of the hexamine nickel(II) complex.

The submersion method has revealed that filament

growth on pyrolytic graphite is possible. Two of the chips were run at 750°C and the results were clouded surfaces and apparent growth on the edges of the chips. SEM analysis revealed growth and possibly the start of filaments on the first chip, and the second chip had no filaments and showed only trace amounts of iron on the surface when tested by EDAX. Another chip was submerged into the ferrous chloride solution for an undetermined amount of time, washed in methanol, rinsed with doubly distilled water and dried overnight in an oven at 71°C. The run conducted on this substrate resulted in straight filaments. A suspected method of deposition and reaction was that the ferrous chloride absorbed into the porous edges of the chips and reduced to iron when hydrogen was passed through the reactor at high temperatures. The reduced iron was fixed and then acted as a catalyst for the acetylene added at the peak of the temperature ramp and held at a constant flow for ten minutes.

The electroplating method of preparation resulted in flocculant growth for the two substrates run. It is thought that the iron deposited onto the graphite was not present in a large enough quantity to nucleate and act as an effective catalyst for the reaction.

DISCUSSION:

The key to preparing substrates that produce long, straight carbon filaments lies in an efficient and effective method that is easily reproducible.

The ion-exchange method is readily assembled however, it does not work on silicon wafers. In addition, the harsh conditions of its medium cause difficulties in maintaining an environment suitable for deposition.

Nickel carbonyl decomposition is also inadequate for much of the same reason. That is, the toxicity of the gas is too hazardous of a risk to make it a viable alternative. On the other hand, the submersion and electroplating methods are reasonably simple to construct, safe and apparently reproducible.

CONCLUSIONS:

The submersion and electroplating methods of substrate preparation have expressed the most promise of all the methods investigated so far. Its flexible characteristics involving safety, ease of assembly and reproducibility has proven that it is worthy of continued research and experimentation.

REFERENCES

1. Benesi, H. A., Curtis, R. M., and Studer, H. P., Journal of Catalysis 10, 328-335 (1968).
2. Blum and Hogaboom, Principles of Electroplating and Electroforming, 3rd Edition. New York, McGraw-Hill Co., 1949.

II-5. GROWTH AND STRUCTURE OF VAPOR-DEPOSITED FILAMENTS ON GRAPHITE AND SILICON SUBSTRATES

Charles W. Bowers and Ian L. Spain
Department of Physics
Colorado State University
Fort Collins, CO 80523

Carol M. McConica
Department of Chemical Engineering
Colorado State University
Fort Collins, CO 80523

and

Tamsin C. McCormick
Electron Microscope Facility
Department of Anatomy
Colorado State University
Fort Collins, CO 80523

Abstract

Filaments have been grown by catalytic-chemical-vapor-deposition techniques on graphite and silicon substrates at temperatures from 700-1000°C. Nickel catalyst and acetylene/hydrogen reaction-gas mixtures were used for all experiments. X-ray diffraction examination of the filaments indicated that those grown on graphite substrates were disordered, and those on silicon between 700-800°C were partially graphitic. Silicon carbide was formed on the silicon substrates between 900-1000°C but was probably not filamentary. The results are discussed in terms of a model for the growth process.

Introduction

In a previous paper (1) the growth of partially graphitic filaments was reported on silicon surfaces from acetylene at 850°C. The silicon surfaces were coated with a thin layer of Ni to provide a catalyst for the growth. The catalyst film forms small spherules on the surface when the temperature rises to that of the reaction. These spherules then act as surfaces for the decomposition of the hydrocarbon, and the deposited carbon deposits under the spherule, pushing it forward. The filament then grows outwards from the surface with the catalyst particle at its end (for a review, see Ref. 2).

The results reported in (1) suggested that the degree of graphitization of the filament was increased when growth occurred on silicon surfaces. X-ray diffraction patterns obtained on filaments grown on graphite substrates under the same conditions showed no evidence of graphene planes (i.e., (002) reflections were so broad that the structure was close to amorphous). On the other hand, those grown on silicon substrates showed well developed (002) reflections, with interlayer spacing characteristic of a graphitization index (3) of about 0.5. This is similar to the graphitization achieved by heat-treating an organic precursor such as anthracene to a temperature of about 2200°C.

This result is of possible technological significance, since it may allow high strength carbon filaments to be grown by the catalytic-chemical-vapor-deposition technique (CCVD) at significantly lower temperatures than those used presently (1100-1200°C) (4). The present study was carried out to investigate the temperature dependence of the graphitization index of the filaments.

The present report is provisional, of work that is not yet complete.

Experimental Details

Filaments were grown by the methods described in Ref. 1. Substrates were either a fine-grain nuclear graphite or single-crystal silicon. Table 1 lists the runs that were carried out. Nickel was used as the catalyst in all cases, 5:1 hydrogen:acetylene for the reaction gas.

After growth the filaments were studied using x-ray diffractometer techniques. The surfaces were also studied in a Phillips 505 scanning-electron microscope to verify that filaments had grown. Efforts are being made to obtain diffraction patterns using transmission-electron microscopy, but this study is not complete.

Experimental Results

Filaments were grown successfully on graphite substrates from 700-1000°C. Diffractometer traces of the filaments did not reveal (002) diffraction lines consistent with earlier findings (1).

Filaments grew on silicon substrates between 700-850°C. Three representative diffractometer traces for the samples grown at 700, 850, and 900°C are shown in Figs. 1-3. In all cases the line at 1.35 Å is from the Si (004) diffraction. The line at about 3.4 Å is identified as the (002) line of carbon. Whenever this line was observed, however, two others at 2.03 and 1.86 Å were also obtained. Table 1 summarizes the powder diffraction lines from graphite in this region. It is possible

that the line at 2.03 Å is the graphite (101), but the relative intensities of the (002) and (101) lines are not in accord with the standard (5). The line at 1.617 Å does not fit the standard (Table 1).

No line at approximately 3.4 Å was observed in the growth runs at 750, 900, 950, or 1000°C. The d-values of this line are recorded in Table 2 for different growth temperatures. It is to be noted that the value decreases between 700 and 800°C growth temperature, then increases at 850°C.

No filaments were grown above 850°C. However, many diffraction lines were observed (see Fig. 3, for example). The lines could not be indexed on the basis of α -SiC or nickel silicides (5). This agrees with similar findings in Ref. (1), where sharp diffraction lines were obtained for growth on carbon substrates which could not be indexed on the basis of known compounds.

Discussion of Results

The present results suggest that graphitic filaments can be grown on silicon substrates over a limited range of temperature (~700-800°C). The diffraction information suggests that the filaments are partially graphitic. Single-crystal graphite has an interlayer spacing of 3.354 Å, and fully turbostratic carbon (i.e., the hexagonal layers are stacked in an uncorrelated fashion) a value of 3.44 Å. The graphitization index is usually expressed as a linear interpretation of these values (3). Higher values than 3.44 Å, such as that found for the filament grown at 700°C, are attributed to the presence of interstitial atoms pushing the planes apart. It is curious in the present case that

the filament grown at 850°C has a lower graphitization index (0.5) than that grown at 800°C (0.7).

It is clear that the x-ray diffraction information obtained on these filaments is somewhat ambiguous, and it is important to state that the observation of a line at about 3.4 Å does not definitely establish the presence of graphitic filaments. Further work is necessary to study the structure using electron microscope techniques, and this work will be attempted in the next contract period.

One possible model for the growth of CCVD filaments is postulated by us as follows:

1. Graphitic filaments grown on graphite substrates at temperatures $>1150^{\circ}\text{C}$ (6) are associated with liquid catalyst particles. Carbon-transition metal eutectics are above this temperature (7), so that either impurities or the effect of small particle size must be responsible for depressing the eutectic temperature below its normal value. (Alternatively, the dehydrogenation reaction heats up the catalyst particle, but this could only be significant if the reaction occurs in bursts since the average temperature rise is too small (8).) These filaments are tubular in structure with a hollow core (9,10).
2. Filaments grown on graphite substrates below about 1100°C have solid catalyst particles. The facets of the catalyst particles favoring growth inhibit the formation of graphene layer tubes. A herringbone structure results (see discussion in Section 4) consistent with electron diffraction examination (11). The

small dimensions of the graphene layers prevent the development of strong (002) x-ray diffractions.

3. The growth of partially graphitic filaments at relatively low temperature on silicon substrates is related to the depression of the catalyst particle eutectic below the reaction temperature, so that it is in a liquid-like state. The eutectic may again be depressed below its normal, bulk, value by the small particle size and by the presence of both carbon and silicon in the metal.
4. The formation of silicon carbide inhibits the growth of carbon filaments from liquid-like catalyst particles at higher temperature.

Several experiments can be carried out to test these hypotheses. The most valuable would be to carry out structural investigations at the temperature of the reaction, but this may not be possible. A more accessible experiment would be to utilize transition metal alloys as catalysts and to investigate the structural evolution of filaments at room temperature as a function of the reaction temperature. A systematic study of this kind could find a direct correlation between the eutectics (bulk) and the reaction thresholds for production of graphitic filaments. One interesting possibility mentioned above is that the small particle size lowers the eutectic temperature. It would be interesting to investigate this experimentally. This may be done using magnetic measurements. Also, models of the melting could be developed as a function of particle size.

Finally, it may be possible to check the ideas proposed here using computer simulation techniques. These simulations are planned for the future.

References

1. Y. X. Zhao, C. W. Bowers, and I. L. Spain, accepted by Carbon (see also Final Report to AFOSR, 1986, Grant No. F49620-84-K-0006).
2. R. T. K. Baker and P. S. Harris, Chem. Phys. Carbon 14, 83 (1978).
3. J. Maire and J. Mering, Proc. 4th Int. Conf. Carbon, p. 345 (1960).
4. T. Koyama, Carbon 10, 757 (1972).
5. ASTM Card File.
6. M. Endo, T. Koyama, and Y. Hishiyama, Japan. J. Appl. Phys. 11, 2073 (1976).
7. M. Hansen and K. Anderko, "Constitution of Binary Alloys" (McGraw Hill, 1958).
8. See Section 4 of the present report.
9. M. Endo, A. Oberlin, and T. Koyama, Japan. J. Appl. Phys. 15, 1519 (1977).
10. G. G. Tibbets, J. Cryst. Growth 66, 632 (1984).
11. E. Boelland, P. K. DeBokx, A. J. H. M. Kock, and J. W. Gues, J. Catalysis 96, 481 (1988).

Table 1. Experimental details of runs.

Catalyst:	Nickel, evaporated onto substrates to thickness of 0.2 μm
Reaction gas:	5:1, H_2 /acetylene
Graphite substrate:	Poco ZXF-50 silicon; (100) orientation from Monsanto; p-doped with boron; resistivity 3 $\Omega\mu\text{m}$ (Lot #9808 SN 190.063312)
Furnace purge gas:	Ar/H_2 (see Ref. 1)
Furnace profile:	See Ref. 1
Reaction temperature:	700, 750, 800, 850, 900, 950, 1000, ± 5 K

Table 2. X-ray diffraction data for graphite from ASTM card file.

(hkl)	002	100	101	102	004
d (Å)	3.37	2.132	2.036	1.80	1.682
I/I _o	100	2	3	1	8

Table 3. Values of d_{002} for filaments as a function of growth temperature.

Growth temperature (°C)	700	750	800	850	900
d_{002} (Å)	3.448	not observed	3.380	3.395	not observed

Figure Captions

Fig. 1. X-ray lines for the filaments grown at 700°C.

Fig. 2. X-ray lines for the filaments grown at 850°C.

Fig. 3. X-ray lines for the filaments grown at 900°C.

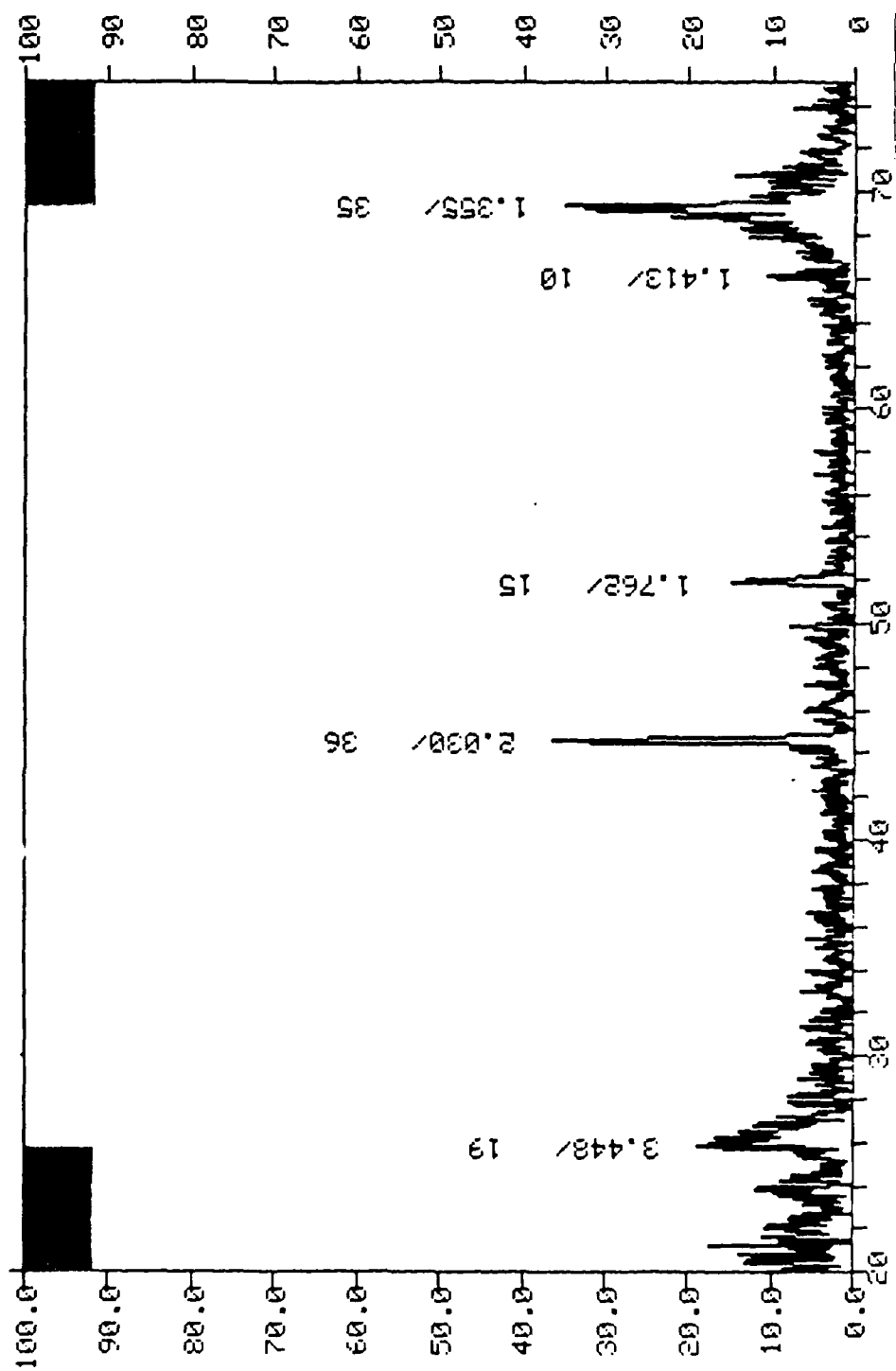


Fig. 1. X-ray lines for the filaments grown at 700°C.

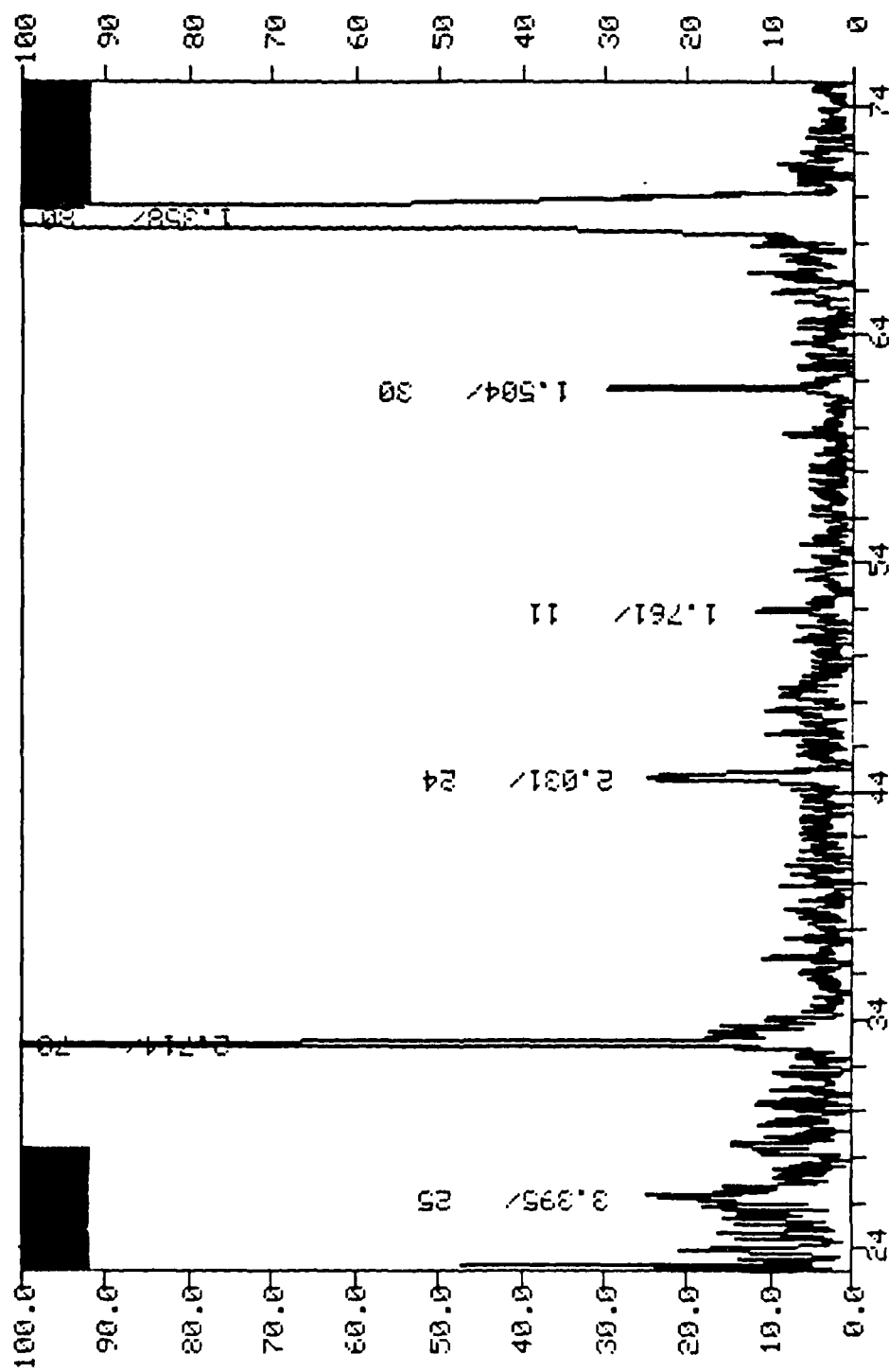


Fig. 2. X-ray lines for the filaments grown at 850°C.

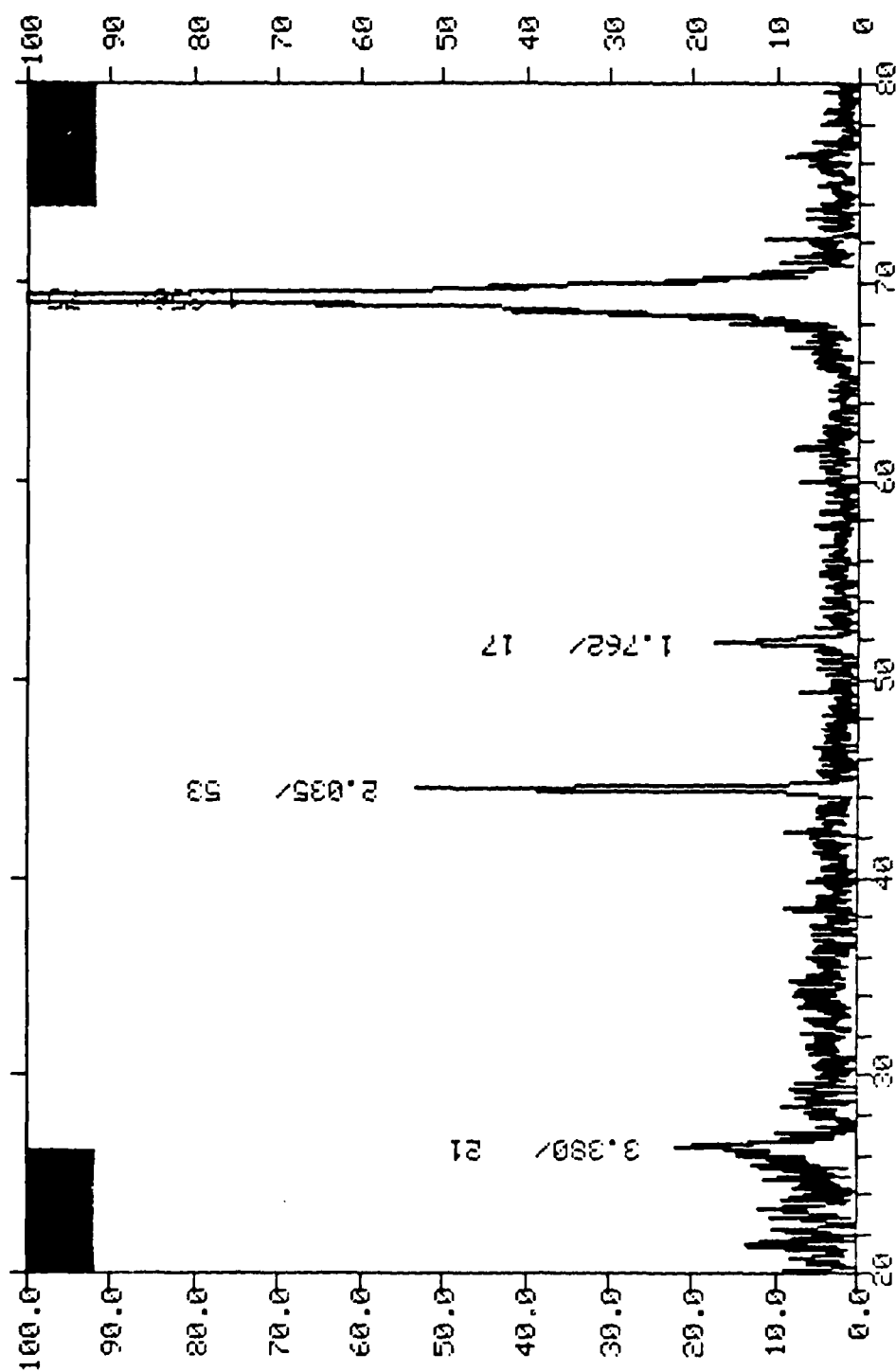


Fig. 3. X-ray lines for the filaments grown at 900°C.

II.6 THICKENING OF EX-PAN CARBON FIBERS BY CVD TECHNIQUES

Frank Dillon, Carol McConica and Ian L. Spain

Departments of Physics and Agricultural and Chemical
Engineering
Colorado State University
Fort Collins, Colorado 80523

1. Abstract

Ex-PAN carbon fibers were thickened to varying degrees by CVD of hydrogen/acetylene gaseous mixtures. This pyrolysis of the mixture can produce two distinct forms of carbon: (1) lamellar pyrolytic carbon and (2) colloidal soot. Lamellar carbon is favored when the partial pressure of acetylene is low. The reaction conditions (partial pressure of acetylene, total gas flow and time) were varied to optimize the thickening rate and minimize nonuniform thickening along the length of the fiber. The same reaction mechanisms controlling the thickening of CCVD filaments appears to control the CVD thickening of ex-PAN carbon fibers. The carbon microstructure revealed by detailed SEM observations of the fracture surfaces of CCVD filaments and thickened ex-PAN carbon fibers appears to be similar. Both are composed of concentric rings of pyrolytic carbon.

2. Introduction

Catalytic chemical vapor deposited (CCVD) filaments have superior structural characteristics relative to polymer-based (e.g., PAN) carbon fibers (Dresselhaus et al., 1987). They can, however, only be produced in finite lengths whereas polymer-based carbon fibers can be produced in continuous lengths. This limitation on the length of the CCVD filament restricts its utilization in a variety of applications.

Recently, workers such as Matsumura et al. (1985) and Shioya et al. (1987) have produced composite carbon fibers (i.e., a polymer-based carbon fiber coated with pyrolytic carbon) by CVD and plasma-assisted CVD, respectively. The carbon is deposited from a gaseous reaction mixture of hydrogen and hydrocarbon (e.g., benzene and cyanoacetylene). The pyrolytic carbon is deposited in concentric rings around the polymer-based carbon fiber. The rate of deposition is primarily controlled by the partial pressure of the hydrocarbon, the ratio between the surface area of the carbon fibers and the volume occupied by the pyrolyzing gas, the temperature and by the overall gas flow.

The pyrolysis of a hydrogen-hydrocarbon gaseous mixture results in a complex series of chemical reactions (dehydrogenation, condensation and aromatization) which, depending on the reaction conditions, can produce two distinct forms of carbon, lamellar pyrolytic carbon and

colloidal soot. During the CVD process, an entire series of molecular species are generated ranging in size through aromatics to complex transitional molecules of low hydrogen content and high molecular weight (Bokros, 1969). Colloidal soot is formed when the pyrolyzing atmosphere becomes supersaturated with high molecular weight macromolecular species which homogeneously nucleate to produce gas-borne carbon particles. The lamellar pyrolytic carbon is formed when the carbon macromolecular species condense directly onto the deposition surface, in this case ex-PAN carbon fibers.

During this work, single ex-PAN carbon fibers were coated to varying thicknesses with pyrolytic carbon by CVD of hydrogen/acetylene mixtures. The reaction conditions such as the partial pressure of acetylene, the overall gas flow, and the reaction time were varied in order to optimize the production and deposition of pyrolytic carbon.

Koyama and Endo (1974) state that the development of CCVD filaments occurs in two distinct phases:

- (1) An initial growth stage which produces thin filaments, and
- (2) A thickening stage where the filaments thicken due to pyrolytic carbon deposition on the filament sides.

There is a critical temperature, 1040°C, above which the thickening process becomes important and below which the growth of the filament is favored (Endo and Koyama, 1977).

However, Oberlin et al. (1976) believe that it is impossible to separate both stages in the development of CCVD filaments because they are statistically concomitant, though successive for a given part of the filament. It seems conceivable that the secondary stage can be utilized in the CVD thickening of ex-PAN carbon fibers. Consequently the heat treatment temperature (HTT) for the CVD process during this work was set at 1100°C, which is above the temperature at which thickening starts to become important in CCVD.

II. Experimental Details

CVD thickening of single ex-PAN carbon fibers

Single ex-PAN carbon fibers were fixed with a colloidal graphite adhesive (LADD colloidal graphite) to a graphite (nuclear grade) substrate. The fibers were heat treated in a resistance furnace in a steady stream of hydrogen gas (99.999 percent) to 1100°C at a heating rate of $\sim 1^\circ \text{sec}^{-1}$. At 1100°C, a known quantity of acetylene gas (99.7 percent) was allowed to flow into the system, mixing with the hydrogen to form the gaseous reaction mixture. The flow rates of hydrogen and acetylene were controlled by individually calibrated Cole-Palmer gas flowmeters. The temperature of the furnace was controlled by a Leeds Northrup temperature controller so the CVD was carried out at atmospheric pressure (~ 632 torr in Colorado) and for periods of time ranging from 60-180 minutes.

SEM observations were carried out using a Phillips series 505 scanning electron microscope, typically operating at an acceleration voltage of 20 kV. The thickened fibers were gold coated (plasma deposited) prior to SEM analysis.

III. Experimental Results

III-1 Fiber Growth Conditions

According to Koyama et al. (1972), the optimum partial pressure of the hydrocarbon (benzene) for the development of CCVD filaments is 180 torr. Therefore the partial pressure of acetylene in the first two runs was set at approximately 180 torr (see Table 1 for exact partial pressures). At this partial pressure, the pyrolyzing atmosphere became supersaturated with carbon macromolecular species which nucleated to form soot so that the ex-PAN carbon givers in Runs 1 and 2 were coated with colloidal soot and lamellar pyrolytic carbon (Figure 1).

In the next series of runs (3, 4 and 5), the partial pressure of acetylene was reduced approximately by half to avoid the supersaturation of carbon macromolecular species in the pyrolyzing atmosphere. This reduction in the partial pressure of acetylene eliminated the production of soot and enhanced the deposition of pyrolytic carbon (Figures 2, 3 and 4). The reaction conditions in Runs 3-5 were kept constant except for the reaction time which ranged from 60 minutes in Run 3 to 180 minutes in Run 5. In all of the

Table 1. CVD thickening of ex-PAN carbon fibers.

	Runs							
	1	2	3	4	5	6	7	8
Gases Used	H ₂ C ₂ H ₂	H ₂ C ₂ H ₂	H ₂ C ₂ H ₂	H ₂ C ₂ H ₂	H ₂ C ₂ H ₂	H ₂ C ₂ H ₂	H ₂ C ₂ H ₂	H ₂ C ₂ H ₂
Z Gas Mixture								
H ₂	71	71	85.8	89.8	89.8	89.4	89.4	89.4
C ₂ H ₂	29	10.2	10.2	10.2	10.2	10.6	10.6	10.6
Partial Pressure (torr)								
H ₂	451.6	450.8	566.6	563.9	569.3	570.4	569.5	564.0
C ₂ H ₂	184.4	184.2	64.4	64.1	64.7	67.6	67.5	67
Gas Flow								
H ₂	120	120	120	120	120	228	228	228
C ₂ H ₂	49	49	49	13.6	13.6	27	27	27
Pressure (torr) [*]	636	635	631	628	634	638	637	637
HTT (°C)	1100	1100	1100	1100	1100	1100	1100	1100
Run Time (min)	60	120	60	120	180	60	120	180
Type of Carbon Deposited	soot P.C.	soot P.C.	P.C.	P.C.	P.C.	P.C.	P.C.	P.C.
Amount of Thickening (μm) ^{**}	n/a	n/a	1	4.0	4.8	15	22	---

* Atmospheric pressure (-632 torr in Colorado).

** Determined from detailed SEM observations.

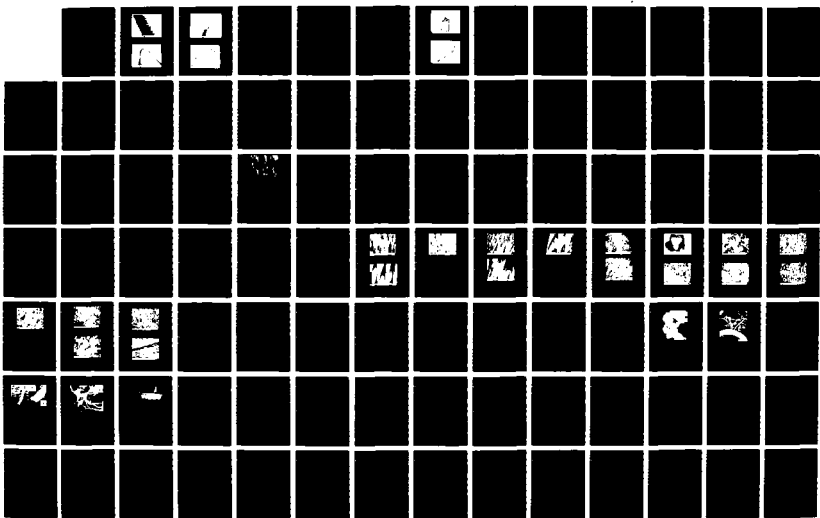
NO-REISO 878

SUB-MICRON CARBON FILAMENTS FOR OPTICAL APPLICATIONS
(U) COLORADO STATE UNIV FORT COLLINS I L SPAIN ET AL.
NOV 87 AFOSR-TR-88-0290 F49620-86-C-0003

2/3

UNCLASSIFIED

F/G 11/2.1 NL



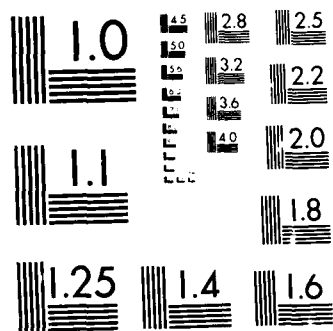




FIGURE 1. Photomicrograph showing an ex-PAN carbon fiber coated with colloidal soot. There is also a thin veneer of pyrolytic carbon deposited around the fiber.



FIGURE 2. Photomicrograph of two ex-PAN carbon fibers that have been thickened by a vitreous pyrolytic carbon.



FIGURE 3. Photomicrograph showing a single ex-PAN carbon fiber thickened by concentric rings or pyrolytic carbon. Note the "droplets" on the surface of the pyrolytic carbon. These droplets represent the intermediate stage between direct deposition of pyrolytic carbons and the formation of soot.

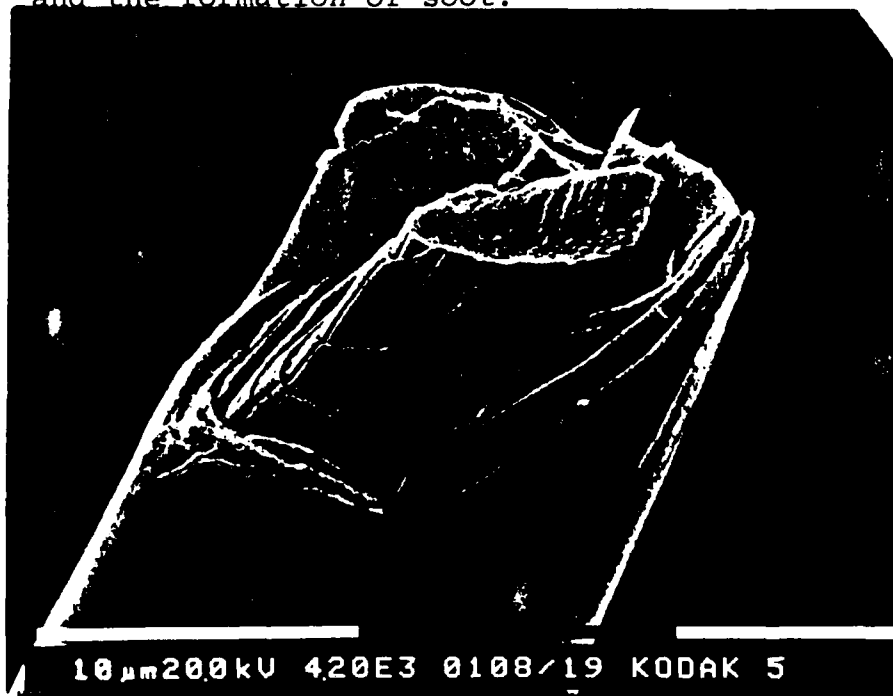


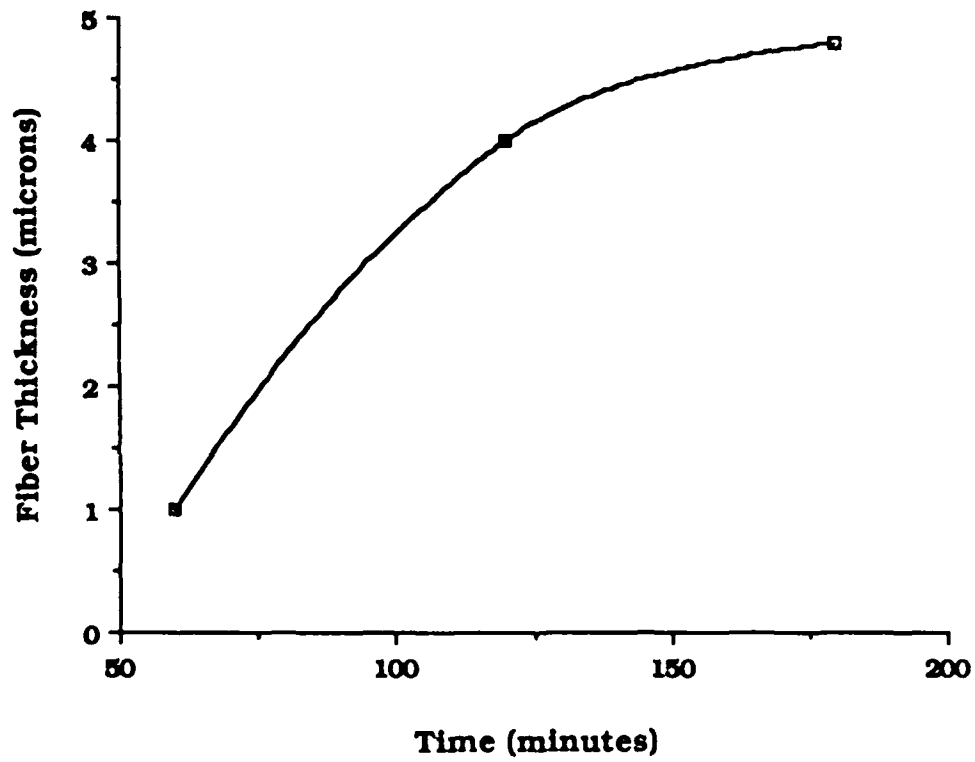
FIGURE 4. Photomicrograph clearly shows the concentric rings of pyrolytic carbon surrounding the ex-PAN carbon fiber.

runs, the CVD process was dominated by the production and deposition of pyrolytic carbon. There is a rapid initial rate of thickening (Figure 5). This rate tails off at about 4 μm (120 minutes) reaction time. A possible explanation of this phenomenon is that as the thickness of the pyrolytic carbon deposit increases so does the surface area available for deposition. Hence, if the surface area is increasing, but the amount of hydrocarbon and thus carbon available for deposition remains constant, there is a consequent reduction in the rate of thickening.

From detailed SEM observations of the thickened fibers from Runs 3, 4 and 5, it appears that there is nonuniform deposition of pyrolytic carbon along the length of the fibers. The nonuniform deposition is due to a concentration gradient of pyrolysis products in the reaction chamber, the pyrolysis products being more concentrated at the gas inlet portion of the reaction chamber. By increasing the overall gas flow, this concentration gradient can be considerably reduced and hence the CVD, along the length of the fibers. It also increased the rate of thickening substantially (Table 1).

The surface texture of the thickened fiber can be altered by increasing the partial pressure of hydrocarbon or by increasing the total flow rate of gas. At lower partial pressures of hydrocarbon or low flow rates, the CVD carbon surface is smooth and essentially featureless. As the partial pressure of hydrocarbon or the total flow rate of

FIG. 5
FIBER THICKNESS VERSUS TIME



gas is increased, the CVD carbon surface becomes roughened and the surface of the thickened ex-PAN carbon fiber takes on a granular appearance (see Figures 6 and 7). This is potentially a very useful feature if the thickened ex-PAN carbon fibers were to be used in composites. The surface irregularity increases the surface area available for wetting thereby enhancing the mechanical bonding between the fiber and the matrix material.

As the structural order of carbon materials improves so does the oxidation resistance (McKee and Mimeault, 1973). This is simply due to the reduced number of exposed prismatic edges present in the more ordered carbon materials. The prismatic edges are orders of magnitude more reactive to oxygen than the basal planes. Therefore, if the pyrolytic carbon coating surrounding the ex-PAN carbon fiber is more ordered than the outer layers of carbon in the ex-PAN carbon fiber, there will be a consequent improvement in oxidation resistance. Another reason for an improvement in the oxidation resistance of thickened ex-PAN carbon fibers is that the pyrolytic carbon does not contain the trace transition element impurities inherent in ex-PAN (and pitch) carbon fibers. It is well known that trace transition element impurities act as catalysts in the oxidation of carbonaceous materials (McKee, 1970a; McKee, 1970b). Since the pyrolytic carbon can be produced with virtually no trace elements present, it acts as a protective shield against catalytic oxidation. It must be stressed,



FIGURE 6. Photomicrograph of a thickened ex-PAN carbon fiber. The surface of the pyrolytic carbon is smooth. (For reaction condition see Run 5, Table 1.)



FIGURE 7. Photomicrograph of a thickened ex-PAN carbon fiber. The surface of the pyrolytic carbon deposit is roughened. (For reaction conditions see Run 6, Table 1).

however, that pyrolytic carbon coating is not a solution to high temperature ($>2000^{\circ}\text{C}$) oxidation resistance. Other coatings such as SiC and BN have been developed for such purposes (Dresselhaus et al., 1988).

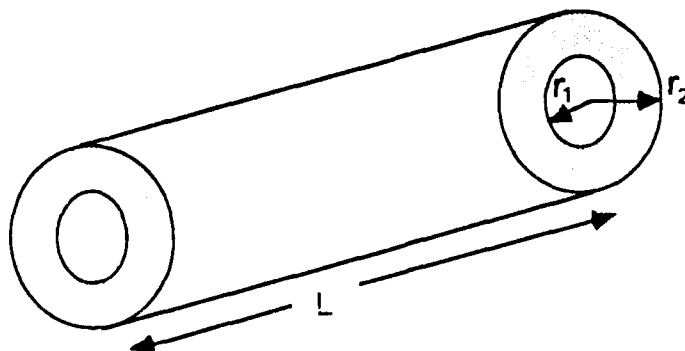
III-2 Kinetics of the CVD Thickening Process

Two experiments were carried out to determine how flow rate and acetylene influence the observed thickening rate of the filaments:

- (1) Where the partial pressure of acetylene was varied in each run while maintaining a constant overall gas flow ($108.5 \text{ cm}^3 \text{ min}^{-1}$) (see Table 2), and
- (2) Where the partial pressure of acetylene was varied in each run in an excess of hydrogen. The gas flow rate of hydrogen was kept constant at $1000 \text{ cm}^3 \text{ min}^{-1}$, in each of the CVD runs (see Table 3).

Calculation of the rate from thickness of CVD carbons

The rate of the CVD thickening reaction is calculated from the thickness of CVD carbon:



$$\begin{aligned}\text{Volume of pyrolytic carbon deposited} &= L[\pi r_2^2 - \pi r_1^2] \\ &= L[\pi(r_2^2 - r_1^2)]\end{aligned}$$

where $r_1 = 3.5 \times 10^{-6} \text{ m}$.

$$\text{Rate} = \frac{S \text{ moles}}{St} = \frac{S \text{ volume}}{St} \times \frac{\text{moles}}{\text{volume}}$$

$$= \frac{Sv}{St} \times \frac{\rho_{\text{carbon}}}{M_{\text{carbon}}}$$

$$= L[\pi(r_2^2 - r_1^2)] \frac{\rho_c}{M_c} \frac{1}{t}$$

$$L = L(\text{cm})$$

$$r = r(\text{m})$$

$$\rho_c = 2.25 \text{ g/cm}^3$$

$$M_c = 12 \text{ g/mole}$$

$$t = 120 \text{ min}$$

$$\text{rate} = \frac{L \cdot \pi \cdot \rho_c}{t M_c} (r_2^2 - r_1^2) \times \frac{10^4 \text{ cm}^2}{\text{m}^2}$$

The data are given in Tables 2 and 3. Plots of rate versus acetylene are given in Figures 8 and 9.

TABLE 2. Carbon deposition rate at low total flow.

Expt	P_{H_2} (torr)	$P_{C_2H_2}$ (torr)	$r_2 - r_1$ ($\times 10^6$ m)	rate $\times 10^{10}$ (moles/min)
1	608	24	0.4	5
2	582	50	1.5	22
3	563	69	17.0	697
4	531	101	23.5	1224

All depositions at 1100°C, 108.5 cm³/min total flow and 120 min.

Pseudo 4th order rate constant = $4.1 \times 10^{18} \text{ l}^4 \text{ mole}^{-3} \text{ min}^{-1}$

TABLE 3. Carbon deposition data at high total flow.

Expt	P_{H_2} (torr)	$P_{C_2H_2}$ (torr)	$r_2 - r_1$ ($\times 10^6$ m)	rate $\times 10^{10}$ (moles/min)
1	618	14	0.5	6.3
2	604	28	14.5	533
3	590	42	16.5	663
4	564	68	33.5	2317

1100°C, 1023 - 1121 cm³/min total flow, 120 min.

Pseudo 4th order rate constant = $41 \times 10^{18} \text{ l}^4 \text{ mole}^{-3} \text{ min}^{-1}$

FIG. 8
DEPOSITION RATE AT LOW TOTAL FLOWS

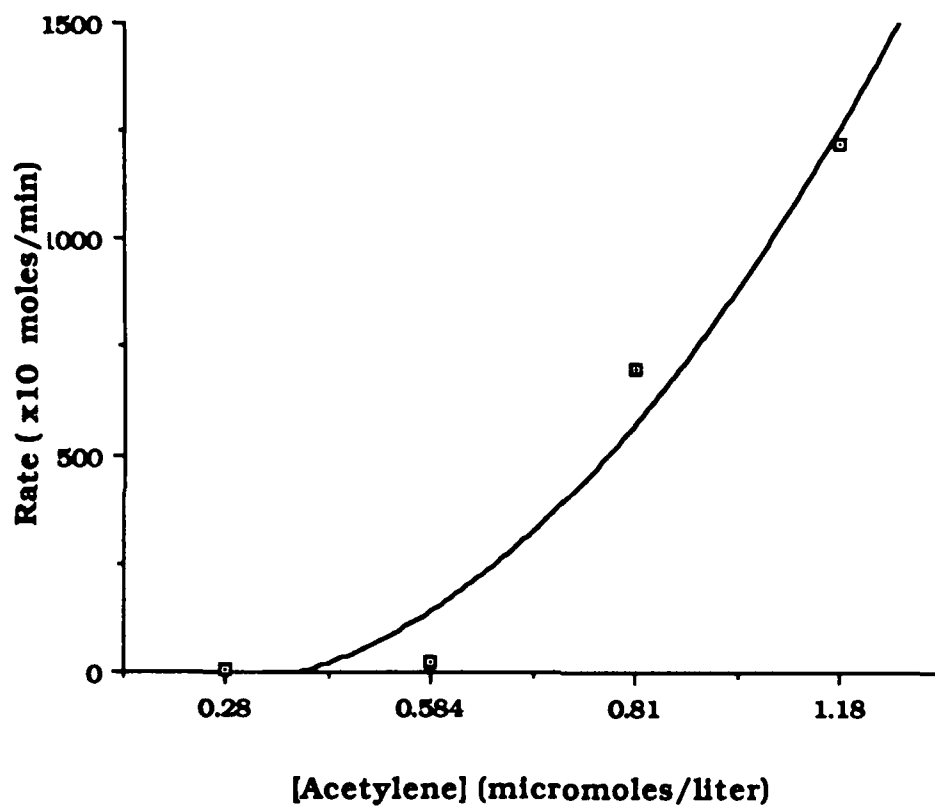
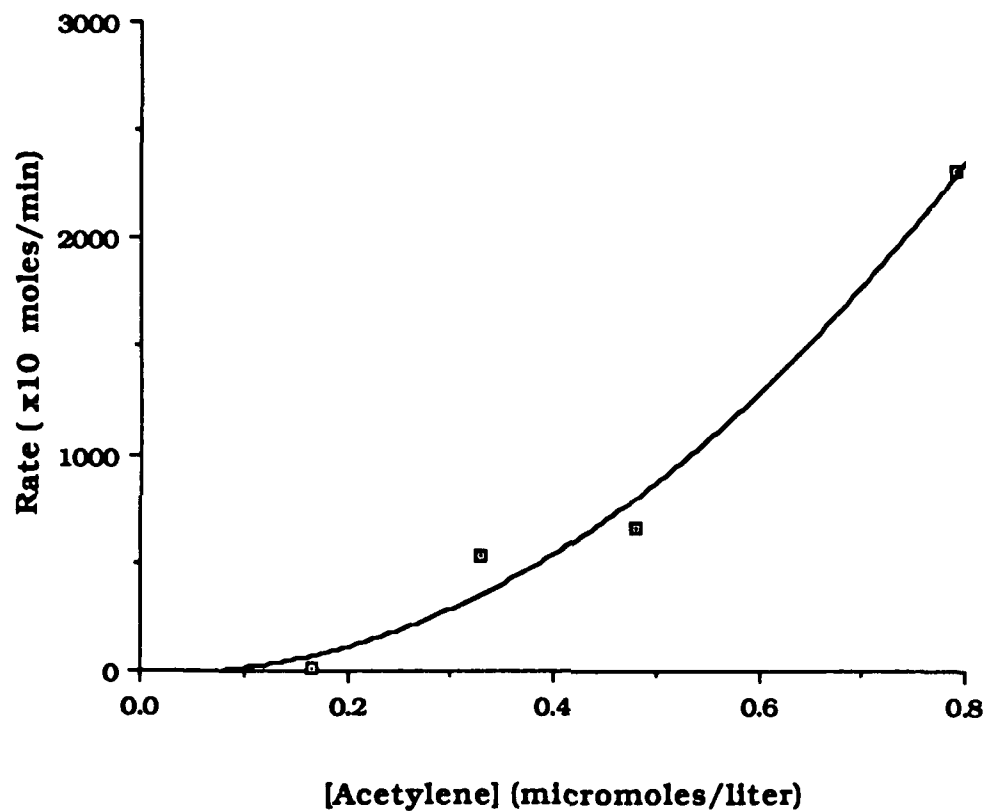


FIG. 9
DEPOSITION RATE AT HIGH TOTAL FLOWS



From a plot of \ln rate against $\ln[C_2H_2]$, a straight line with a slope of n (pseudo reaction order) is obtained. For experiments 1 and 2, orders of 4.1 and 3.7 were obtained, respectively (see Figures 10 and 11).

The most significant result from the two experiments is that increasing total flow increases the deposition rate indicating a strong mass transfer effect. A pseudo rate constant can be found by assuming 4th order kinetics. Increasing the total flow by a factor of ten also increases the pseudo reaction rate constant by a factor of ten.

It seems likely that a gas-phase precursor is involved in the CVD reaction, but it is not apparent from the reaction kinetics in this case. To establish if indeed a gas-phase precursor is involved in the CVD reaction, a series of CVD runs must be carried out where the total flow rate of gases increases while the partial pressure of hydrocarbon and hydrogen remains constant. Ultimately there will be a stage at which, due to the high gas flow rates, there will not be enough residence time in the reaction chamber for a gas-phase precursor to be formed and the only reaction involved will be confined to the surface.

To establish even an empirical reaction mechanism of the CVD process is extremely difficult. There are many complex chemical reactions involved and a variety of products depending on the reaction condition. Before a reaction mechanism can be postulated, more experiments will be needed to first verify that the above measured rates

FIG. 10
LN RATE vs LN [ACETYLENE] AT LOW FLOW

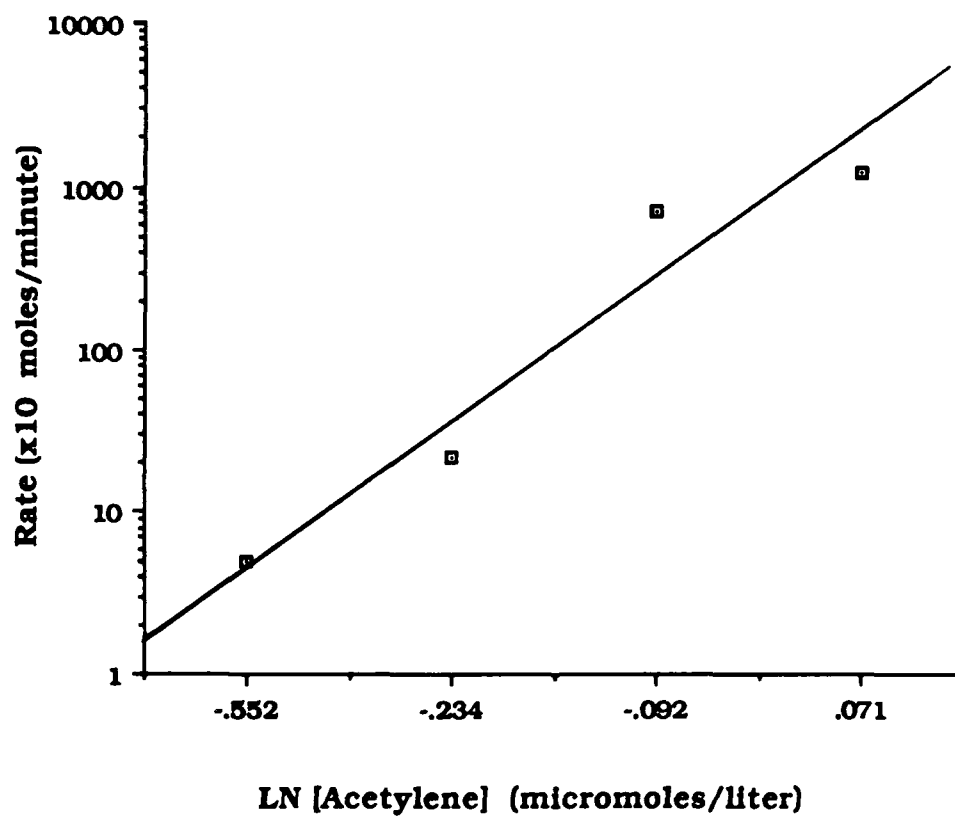
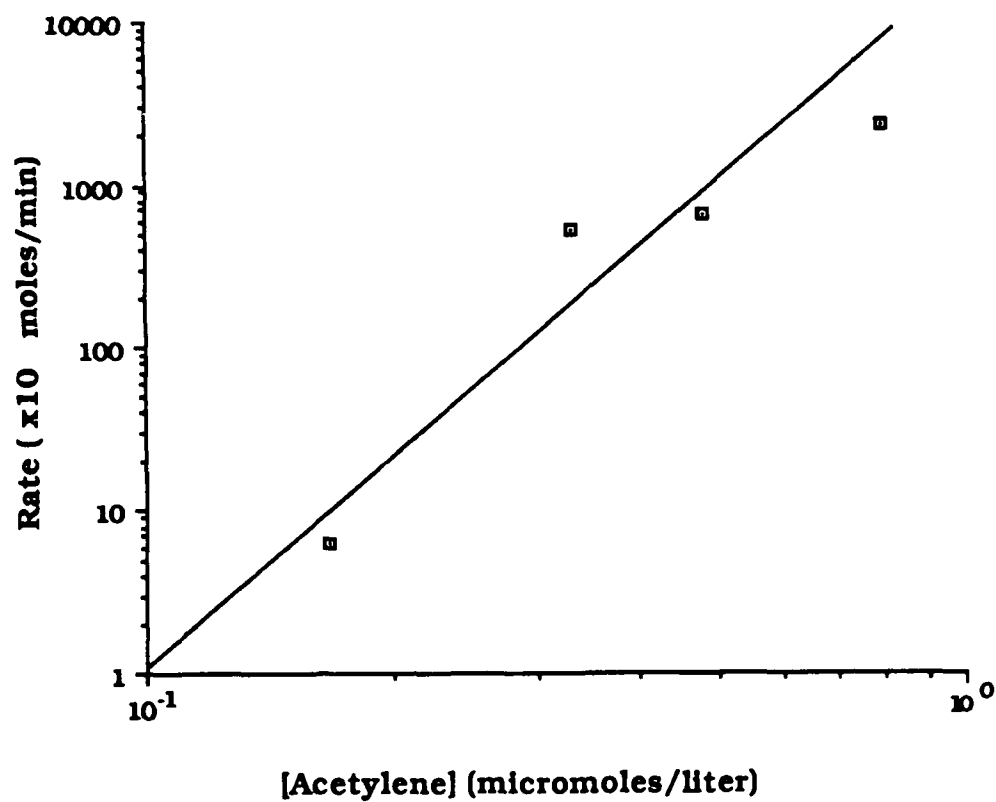


FIG. 11
LN RATE vs LN [ACETYLENE] AT HIGH FLOW



represent kinetics rather than mass-transfer or flow rate limitations, and secondly to clearly correlate the thickening rate with the in situ gas composition.

IV. Conclusion

Ex-PAN carbon fibers can be uniformly thickened by CVD from a gaseous reaction mixture of hydrogen/acetylene. The rate of thickening can be enhanced by increasing the partial pressure of the acetylene and the flow rate of the gaseous reaction mixture. This can be explained when one considers that as the overall gas flow rate is increased, the nucleation time for the development and subsequent growth of soot is greatly reduced. Thus there are more carbon macromolecular species available in the reaction chamber for direct deposition onto the ex-PAN carbon fibers. The increased flow rate also counteracts the natural tendency for a concentration gradient of pyrolysis products to be set up in the reaction chamber. By increasing the flow rate of gases, the concentration gradient is reduced and deposition along the reaction chamber and therefore along the length of the ex-PAN carbon fibers is more uniform.

There are two possible routes for the pyrolysis process. At high partial pressures of acetylene (above the supersaturation point), colloidal soot will be formed. At lower partial pressures of acetylene, lamellus pyrolytic carbon will be formed. In order that the CVD thickening of

ex-PAN carbon fibers is as efficient as possible, the partial pressure of acetylene must be set just below the supersaturation point.

It seems likely that the mechanism controlling the thickening stage in the growth and development of CCVD filaments also controls the CVD thickening of ex-PAN carbon fibers. Tentative proof that such a relationship exists was found when CCVD filaments were developed from the nuclear grade graphite substrate during the CVD thickening of ex-PAN carbon fibers. The CCVD filaments were straight and uniform in diameter (5 μm). Detailed SEM observation of the CCVD filaments fracture surfaces revealed a very similar carbon microstructure to that of the pyrolytic carbon deposit surrounding the thickened ex-PAN carbon fibers (Figures 14 and 15). Both are composed of concentric rings of pyrolytic carbon. The type of catalyst responsible for the growth and development of the CCVD filaments has not as yet been identified. It seems likely, however, that the catalysts were Fe particles generated from an iron containing contaminant in the reaction chamber. In subsequent experiments, the reaction chamber was heat-treated in air to oxidize any metallic contaminant before each CVD run. As a result, there was no further CCVD filament growth.

V. Future Work

The characterization of the thickened ex-PAN carbon fibers will be carried out using x-ray diffraction and

resistivity measurements. Both techniques yield information on the structure of the pyrolytic carbon.

Single filament tensile tests will be performed to assess the effect of varying thicknesses of pyrolytic carbon on the strength of the ex-PAN carbon fiber.

Further CVD reactions will be carried out to determine the kinetics of the CVD reaction and propose a reaction mechanism.

VI. References

- Bokros, K. 1969. In: Chemistry and Physics of Carbon. 5.
- Dresselhaus, M. S., G. Dresselhaus, K. Sugihara, I. L. Spain, and H. Goldberg. 1987. Carbon Fibers and Filaments. to be published by Springer Verlag, Berlin.
- Endo, M. and T. Koyama. 1977. Katai Buturi (Japan). 12,. 1 (in Japanese).
- Koyama, T. and M. Endo. 1974. Japan. J. Appl. Phys. 13, 1175.
- Koyama, T., M. Endo and Y. Onuma. 1972. Japan J. Appl. Phys. 11, 445-449.
- Matsumura, K., A. Takahashi and J. Tsukamoto. 1985. Synthetic Metals. 11, 9.
- McKee, D. W. and V. J. Mimeault. 1973. In: Chemistry and Physics of Carbon. 8.
- McKee, D. W. 1970a. Carbon. 8, 131.
- McKee, D. W. 1970b. Carbon. 8, 623.
- Oberlin, A., M. Endo and T. Koyama. 1976. J. Cryst. Growth. 32, 335.
- Shioya, J., H. Matsubara and S. Murakami. 1986. Synthetic Metals. 14, 113.

II.7. SOME SPECULATIONS CONCERNING GROWTH FEATURES ON CARBON SURFACES DUE TO ION-BOMBARDMENT

William A. Solberg and Ian L. Spain
Department of Physics
Colorado State University
Fort Collins, CO 80523

Abstract

Cones with long filaments at the tip grow on carbon surfaces when bombarded with argon ions of energy in the ~ 1 keV range. A recent model for their nucleation and growth uses the concepts of rapid surface diffusion and supersaturation of sites. This model does not explain the increase of the surface density as the substrate temperature increases. It is proposed that this feature can be explained by postulating that nucleation sites are poisoned at lower temperature by an impurity such as hydrogen. Also, the growth occurs in three stages--firstly nucleation, followed secondly by redeposition of sputtered atoms on the initial growth features, with filaments growing thirdly by a process which may be associated with rapid surface diffusion, possibly enhanced by the presence of high electric fields at the filament tips. The results of simple calculations supporting the contention that redeposition is an important process are reported, followed by suggestions for further experimental work.

Growth of sub-micron sized carbon whiskers have been observed on a graphite surface after directed ion bombardment with energetic argon ions (~500 eV) (1,2,3). The growth features often have conical bases with filament-like tips with a high aspect ratio as shown in Fig. 1, indicating a growth phenomenon rather than an erosion process.

An extensive study by Floro, Rossnagel, and Robinson (3) was carried out on the growth of carbon whiskers by ion bombardment of polycrystalline carbon surfaces. Ion bombardment times and ion energies were systematically varied to observe the effects on whisker growth. The lengths and diameters of the whiskers were examined with increasing bombardment time. The results showed that an initial smoothing of the substrate surface preceeded a rapid growth spurt after a dose of -1.8×10^{19} ions/cm², and that a slower increase in the length and the diameter followed. It was also noted that second-generation whiskers started growing with first-generation whiskers being destroyed, keeping the whisker surface density constant in time. The volume of the whiskers versus increasing ion beam energy was also studied (3). The results showed a decrease in the whisker surface density and an increase in volume per whisker with increasing beam energy. The combined effects resulted in a linear increase of the volume of whiskers per unit substrate area with increasing beam energy.

A model, based partly on the experimental results of the current study for the nucleation and growth of the carbon whiskers (4) was proposed by Van Vechten (5). The model was based on kink-site saturation, a concept used to explain molecular beam epitaxial growth of AlGaAs alloys (6). The kink-site saturation model supposes the carbon supply to arrive from mobile surface atoms produced by the ion

bombardment of the graphite surface, rather than sputtered carbon atoms. A critical ion current density was postulated to supply carbon atoms at a fast enough rate to achieve saturation of the kink-sites before the atoms can reattach to the graphite lattice. The critical ion current density has not yet been observed experimentally. Also, after a mobile carbon atom attaches to the kink-site, a time is required for it to release its energy before another carbon atom may attach. The saturation of kink-sites then leads to the nucleation of cone-like structures. These kink-sites are proposed to be screw dislocations to provide a perpetual growth step. The whiskers then grow from the tips of the cones. Other kink-sites, such as edge atoms, provide attachment-sites for the initial smoothing of the surface as observed (3). Also, the observation that seeding the substrate with impurities inhibits whisker growth (3) can be explained by this model because the impurities provide more sites for attachment, so that saturation of the kink-sites cannot be achieved.

The emphasis of recent experiments (4) was to study the temperature dependence of the surface density. All substrates were pyrolytic graphite, bombarded with 700 eV argon ions at a current density of 0.75 mA/cm^2 for 60 minutes. This provided an ion dose of $1.7 \times 10^{19} \text{ ions/cm}^2$. The substrate temperature was varied over a range of -150°C to 450°C . As shown in Fig. 2, the surface density of whiskers increased from approximately 10^5 to $10^8 \text{ whiskers/cm}^2$ at approximately 250°C with no whisker growth below -30°C .

This increase in surface density with temperature is opposite to that observed for the density of (erosion) surface features caused by ion-bombardment of metallic surfaces in the presence of impurity

seeding. A diffusion-controlled phenomenon was postulated to explain these phenomena, whose activation energy can be obtained from analysis of the temperature dependence of the surface density (7).

A possible mechanism to explain the increase in whisker density with increasing temperature in the present case is that a gaseous contaminant poisons the kink sites, and is released from the substrate upon heating. A gaseous contaminant that is difficult to control and detect is hydrogen. It has been shown that there is an enhanced reactivity of graphite with hydrogen under electron bombardment, as observed by enhanced methane production (8,9), for reaction temperatures above -230°C . This is approximately the same temperature where a substantial rise in whisker density is detected. It is postulated that hydrogen at the kink-sites is then released, providing a site for carbon attachment. A rise in whisker density with increasing temperature would then result.

Although Van Vechten's model for the initial growth features appears to fit the experimental data qualitatively (5), it cannot account for the continued growth of the cones and whiskers, since the required surface diffusion distance of the ions from the bases of the features to the tips would be too great. Accordingly, an alternative method for the supply of carbon atoms to the whiskers by sputter redeposition rather than by surface diffusion alone was investigated. After the initial diffusion to the kink-site as described earlier (5), a microstructure is formed on the surface. Once a surface feature appears, there is some probability that sputtered carbon atoms may impinge this microstructure and reattach.

An approximate calculation shows that sputtering can supply the needed number of carbon atoms. The sputter-rate of carbon has been measured to be 40 Å/minute for an ion beam energy of 500 eV and current density of 1 mA/cm² (10). Thus, approximately 5×10^{17} carbon atoms/cm² are sputtered off a surface after bombardment during the time interval 4-15 minutes at 700 eV and 0.75 mA/cm². For this time interval experimental data give the volume change of the growth features as corresponding to about 8×10^{16} /cm² atoms. This is approximately 15% of those sputtered.

A calculation was made assuming a cosine θ distribution for the sputtered atoms, where θ is the angle made by the sputtered atom with the normal to the surface (Fig. 3). The rate of arrival of atoms, I , at a point on a conical feature of radius $W/2$ from a point on the surface distance r from the original nucleation site (Fig. 3) is then:

$$I = 4\pi\Phi \int_0^R \int_0^{\pi/2} (r + W/2) \cos \theta \arcsin \left(\frac{\frac{W}{2r}}{\sin \theta} + W \right) d\theta dr$$

where Φ is the sputtered flux and W is the width of the base. This expression was integrated numerically assuming a cone-like shape for the growth-feature, neglecting any whisker at the tip, but taking into account the obscuration effect of other growth-features through the parameter R . The cone-like shape was approximated as progressively smaller stacked cylinders. The results are presented in Table 1 for two possible structures of carbon, namely diamond and graphite, although neither is appropriate to the growth-features obtained experimentally.

However, the density of disordered carbon in the cones is probably intermediate between the two cases.

As shown in Table 1, there is enough carbon arriving via redeposition ($>100\%$), although a smaller proportion for the first four minutes of bombardment. This may suggest a different mechanism for the initial growth such as the kink-site saturation mechanism (5). This supports previous work (3) showing an initial growth spurt for whiskers grown on polycrystalline graphite. The table shows that there are enough carbon atoms supplied by sputtering alone, although the whiskers could not grow in length if there was not some movement of carbon atoms to the tip of the whisker. The over-estimation of carbon arriving may be due to some sputtering and diffusing of atoms off the whisker. The cone-like shape of the whiskers at high temperatures ($>300^{\circ}\text{C}$) could be explained because more carbon is redeposited at the base of the whiskers than at the tip. This would cause the whiskers to be cone-like in shape. The appearance of the long filaments at the tip of some whiskers may occur because the carbon redeposition to the sides of the whiskers have enough energy to migrate to the tip and find an attachment site.

The above mechanisms of growth do not explain why filaments grow from the tips of some cones. One possibility is that high electric fields in the plasma near the tips cause ions on the surface to drift towards the tips. However, this possibility is not consistent with the growth of filaments at an angle to the surface, but parallel to the ion-bombardment direction, when the beam is at an angle to the surface normal (3). In this case the electric field remains parallel to the normal. Nor is it consistent with the observation (see Section III-8) that filaments sometimes grow on rounded cones, or even on the surface.

It is possible that the diffusion length of mobile carbon atoms on the surface of the cones is sufficiently long for growth to occur by diffusion. For instance, diffusion lengths of 10 μm are possible for surface atoms on a bombarded surface.

Another feature which needs to be explained is the change of shape of the growth features as temperature changes. Below about 200°C more cylindrical structures are observed, while more conical features with filamentary tips occur at higher temperature. This may also be related to a diffusion-related phenomenon, where higher mobility at higher temperature allows carbon atoms to arrive at higher rates at the bases. There are no experimental data for the rate of ion-enhanced diffusion for carbon, so that this cannot be modeled at the present time. It is possible that the presence of surface hydrogen is crucial for the arrest of surface diffusion below 200°C. Thus, the change of shape and surface density of the filaments with temperature may be interrelated.

Several experiments can be suggested to test some of the ideas expressed in these models.

1. A critical parameter in the nucleation phase is the ion current density, which must be greater than a critical value for supersaturation to occur (5). This has not been observed, possibly because this parameter has not been varied over a sufficient range.
2. It should be possible to detect the evolution of hydrogen from the nucleation sites during the initial bombardment by using a residual-gas analyzer. The release of hydrogen could be signaled by the detection of methane, or other hydrocarbons, due to reaction of the hydrogen at the nucleation site.

Evolved gas should increase significantly as the temperature is increased around 230°C (9).

3. A test of the sputter-deposition postulate could be carried out by initially bombarding the surface at a temperature such as 400°C, creating many sites for growth of features, then cooling the surface to a temperature such as -30°C at which no growth was observed when the bombardment was carried out completely under these conditions. Once the initial growth features are established at high temperature, they should continue to grow at low temperature by sputter-redeposition.
4. It would be of interest to carry out experiments in controlled atmospheres of hydrogen. Thus, the influence of hydrogen on the nucleation density and diffusion rates (shape) could be tested.
5. The above conjectures can be tested with computer simulations of growth. This work is planned in the next contract period.

Acknowledgements

Thanks are to the Air Force Office of Scientific Research for support through contracts #F49620-84-K-0006 and #F49620-86-C-0083. Thanks are also due to Prof. J. A. Van Vechten for helpful discussions.

References

1. J. J. Cuomo and J. M. E. Harper, IBM Tech. Disclosure Bull. 20, 775 (1977).
2. R. S. Robinson and S. M. Rossnagel, J. Vac. Sci. Technol. 21, 790 (1982).

3. J. A. Floro, S. M. Rossnagel, and R. S. Robinson, J. Vac. Sci. Technol. A1, 1398 (1983).
4. W. A. Solberg, M.S. Thesis, Colorado State University, 1986.
5. J. A. Van Vechten, W. A. Solberg, P. E. Batson, J. J. Cuomo, and S. M. Rossnagel, IBM Res. Rep. (C12010, 1986).
6. J. A. Van Vechten, J. Crystal Growth 71, 326 (1985).
7. H. R. Kaufman and R. S. Robinson, J. Vac. Sci. Technol. 16, 175 (1979).
8. C. I. H. Ashby, Appl. Phys. Lett. 42, 609 (1983).
9. D. K. Brice and C. I. H. Ashby, J. Chem. Phys. 81, 6244 (1984).
10. Data from "Chart of Sputter Rates," (Ion Tech, Inc., Fort Collins, CO).

Table 1. Atoms redeposited compared with atoms needed for growth.

Growth Time (min)	Atoms Redeposited	Diamond		Graphite		H (μm)	W (μm)
		Str. Atoms for Growth	%	Str. Atoms for Growth	%		
0-4	5.3×10^7	3.0×10^7	180	1.9×10^8	280	0.1	0.1
4-15	1.5×10^9	4.3×10^8	350	2.8×10^8	540	1.5	0.1
15-60	4.9×10^{10}	1.6×10^{10}	310	9.7×10^9	500	5.4	0.4
60-120	6.9×10^{10}	3.9×10^{10}	180	2.5×10^{10}	280	5.0	0.5

Figure Captions

- Fig. 1. Micrograph and illustration of cone and filament parts of high temperature whisker sample.
- Fig. 2. Whisker density vs. adjusted temperature.
- Fig. 3. A sketch of a filament and cone showing notation used in the text.

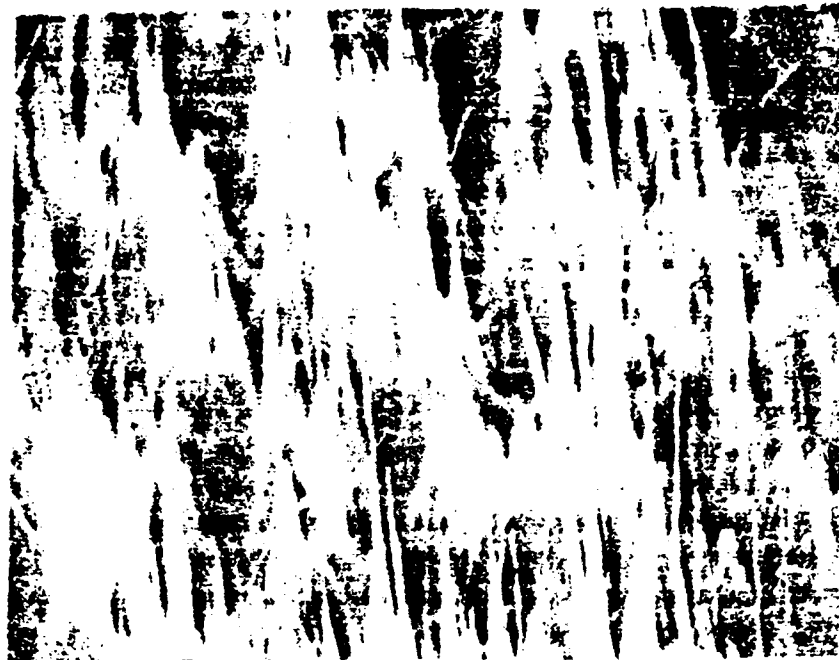


Fig. 1. Micrograph and illustration of cone and filament parts of high temperature whisker sample.

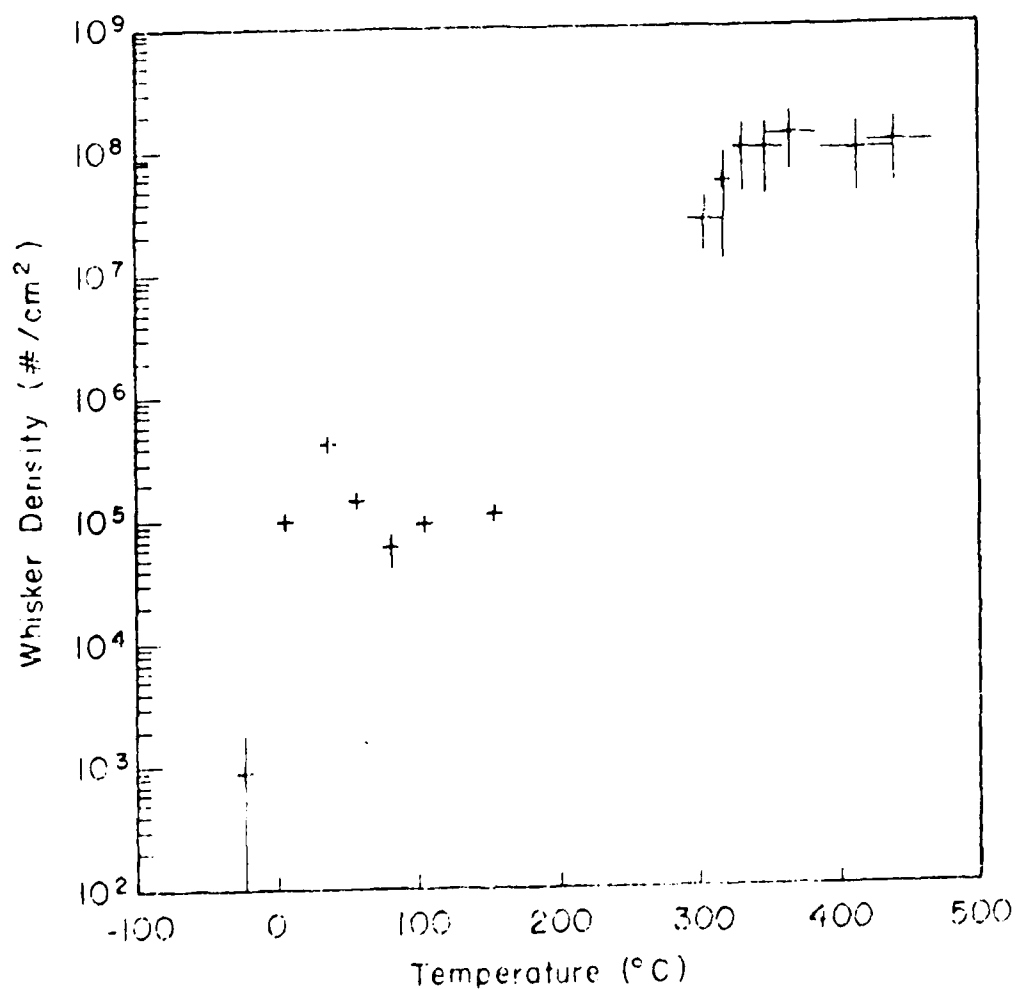


Fig. 2. Whisker density vs. adjusted temperature.

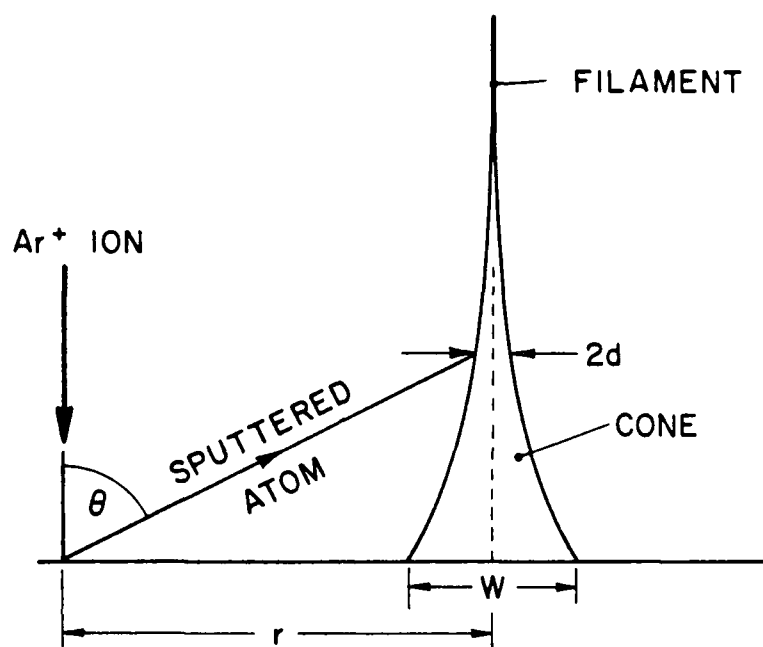


Fig. 3. A sketch of a filament and cone showing notation used in the text.

II.8 GROWTH FEATURES FROM ION-BOMBARDMENT OF CARBON AND SILICON SUBSTRATES FROM PLASMAS

John H. Bradshaw
Optoline
15 Stevens Street
Andover, MA 01810

and

Charles W. Bowers^{*} and Ian L. Spain
Department of Physics
Colorado State University
Fort Collins, CO 80523

Abstract

Growth features produced by ion bombardment from a plasma on three types of carbon and one silicon substrate have been studied. Plasmas were struck in pure Ar, Ar/H₂, Ar/propane, and Ar/methane mixtures at 5% and 10% concentrations. It was found that the cone/filament features grown were dependent on the substrate and the plasma composition. In some instances filaments were found to grow directly from the substrate. No straight filaments were observed. The experiments are discussed briefly in terms of models for the growth processes.

^{*}Permanent address: Hughes Aircraft Co., P.O. Box 902, El Segundo, CA 90245.

Introduction

Carbon filaments can be grown by bombarding carbon surfaces with energetic ions, such as 1 keV Ar^+ ions. The first observation of this growth was in an Ar^+ plasma (1), but all subsequent work has been carried out in systems with ion guns (2-4). There appear to be some differences in the results obtained by the two methods. Most importantly for obscuration applications is the difference in the shapes of the filaments grown in the plasma (1), which were reported to be of constant diameter, whereas those grown with ion guns are tapered, with conical bases.

It has been conjectured (4) that a higher concentration of hydrogen in the ion gun induced plasmas may be responsible for the conical structures, although the mechanism has not been discussed in the literature. It was proposed that hydrogen poisons the nucleation sites (5), possibly screw dislocations (4), thereby limiting the density and shape of the filaments. Hydrogen is always present in vacuum systems, both in elemental form and in molecular form. Stainless steel vacuum tubing, unless specially electropolished, constantly outgasses hydrogen that permeates through the tubing walls. However, the largest source of hydrogen within a high vacuum system is water. Water will decompose within the plasma and form large quantities of elemental and ionic hydrogen. High temperature vacuum baking ($>400^\circ\text{C}$) and electropolishing will reduce the quantity of hydrogen within a vacuum system, but it can never be eliminated completely. Metallic impurities have also been shown to inhibit filament growth (3). Some investigators believe this

is due to the creation of an overabundance of nucleation sites and a lack of sufficient mobile carbon atoms to supersaturate them (4).

The only controlled experiments which have resulted in shape changes were those in which the substrate temperature was varied. Conical growth features with filaments on the ends were obtained at higher temperature, and more cylindrical features at lower temperature (4). These experiments, carried out with bombardment from ion guns (4), did not result in the growth of filaments with uniform submicron diameters.

This report describes the results of some experiments to grow carbon filaments from plasmas. Experiments similar to those of Cuomo and Harper (1) were carried out to ascertain whether straight filaments could be grown reliably by this method. In addition, further experiments were conducted in which hydrogen was introduced intentionally into the plasma, and others in which a hydrocarbon was introduced. Different carbon substrates were employed, as well as one of Si.

II. EXPERIMENTAL DETAILS

Experiments were carried out in a large rectangular plasma system enabling a flat-plate area of $\sim 75 \times 400$ mm to be bombarded. The chamber was pumped to 10^{-6} torr before introducing gas, and operated at $3.8 \mu\text{m}$ pressure. Plasma input power was 600-800 W at 2-3 A, so that the bombardment energy was 200-300 eV or less after collisions. High purity Ar, H_2 , methane, and propane were used in the plasma. Details of the runs are given in Table 1.

Several substrates were bombarded simultaneously in the chamber. Details of the carbon/graphite and silicon substrates are given in Table 2. Each was in the form of rectangles of size $\sim 50 \times 100$ mm. Samples 1 and 2 are nuclear-grade graphites for which the crystallite dimensions are 4 and $< 1 \mu\text{m}$ respectively. These polycrystalline materials ensured that both basal and prismatic surfaces of crystallites were exposed to the ion-bombardment. On the other hand, Sample 3 was prepared from pyrolytic carbon, in which the c-axes were aligned parallel to the surface. Accordingly, only prismatic surfaces (the ends of the hexagon planes) were exposed to the ions. These samples appeared to have delamination cracks running along the surfaces. They were of interest for practical reasons as well as scientific, since this material is used to coat the Princeton Tokamak chamber.

Samples were examined before and after bombardment in a Phillips 505 scanning electron microscope using beam energies of typically 25-30 keV. Chemical composition was studied in some instances using an EDAX technique with a Be window.

Experimental Results

Argon Plasma

The first experiment was carried out to follow as closely as possible the conditions of the original experiment of Cuomo and Harper (1). The radio-frequency plasma was struck without a DC bias. No filaments were found on the substrate. It is probable that a DC bias is needed to excite the bombarding ions to greater energies than those used in the present experiment.

All subsequent experiments were carried out with DC plasmas. The second experiment, in which a DC plasma was struck in pure Ar with a small concentration of H_2 contaminant from the chamber, indicated that a surface density of cones $\sim 10^{11} \text{ m}^{-2}$ was obtained on Substrates 1 and 2, but that very few filaments were obtained (Fig. 1). This contrasts with the results in Ref. 1, where no cones were reported, and a high density of straight, uniform filaments. Figure 2 illustrates the inhomogeneous growth on Substrate 3, where higher growth density is observed at the edge of a crack. It is noted that filaments are growing from the smaller, rounded features rather than sharp cones.

It is emphasized that the conditions used in the experiment of Cuomo and Harper need to be duplicated exactly in order to investigate their filaments of uniform diameter. Small differences in the conditions may lead to different results. Unfortunately, their apparatus is no longer available, so that further work will be needed to investigate their result. It is planned to carry out this experiment in the next contract period, and Cuomo and Harper are attempting to define the conditions used in their experiments more closely.

Ar/ H_2 Plasmas

The second experiment used a mixture of 95% Ar and 5% H_2 for the plasma. A higher density of cones with filamentary tips were found on the carbon substrates, but not on the Si, as follows:

- (a) Graphite Substrate 1: Figure 3 shows that a high density of cones (about $10^{12}/\text{m}^2$) was formed on the substrate. These cones are of different heights, and only the smaller ones have filaments of

diameter $\sim 1 \mu\text{m}$ growing from the tips. The larger ones have rounded tips.

- (b) Graphite Substrate 2: Similar results were obtained on this substrate, and Fig. 4 illustrates a rounded cone end with a radius of curvature of about $0.5 \mu\text{m}$.
- (c) Graphite Substrate 3: In this case it was found that the growth was inhomogeneous, as illustrated in Fig. 5. Examination of the smaller cones growing in the region of sparse growth indicated filaments growing from the tips (Fig. 5a). They are not straight, and have diameters of $\sim 0.1 \mu\text{m}$, about 10% of the dimensions of those above.
- (d) Si Substrate: A growth feature of $\sim 30 \mu\text{m}$ diameter was found on the surface, as illustrated in Fig. 6. At the time of these experiments it was not possible to carry out windowless EDAX measurements, so that the composition of the feature cannot be determined.

Another set of experiments was carried out with 90% Ar and 10% H_2 . Similar results were obtained as above, summarized by stating that the densities of cones were higher in these two experiments than in others (below), and inhomogeneous growth was observed in the case of Substrate 1, as seen in Fig. 7. Again, no filament growth was observed on the larger cones. No growth was observed on the Si substrate. Since no other growth features were obtained on Si surfaces, these experiments will not be discussed further in this report.

Ar/Propane Plasmas

The first experiments were carried out with 90.25% Ar/9.75% propane plasma. Figure 8 illustrates the soot-like deposits found on all of the substrates.

A second set of experiments was carried out with 95% Ar/5% propane gas. The results depended strikingly on the substrate. Only a low density of cones ($\sim 4 \times 10^{10}/\text{m}^2$) was found for Substrate 1, with some filaments. Some rounded cones were found for Substrate 2, but filaments grew directly from the substrate, as illustrated in Fig. 9. Pointed cones grew from Substrate 3, with filaments between them, as illustrated in Fig. 10. This type of inhomogeneous growth was even more pronounced with Substrate 3, where a few conical features were observed (separated by tens of microns), with filaments growing directly from the surface in the areas between the cones ($\sim 10^{12}/\text{m}^2$).

Ar/Methane Plasma

Runs carried out with methane in the plasma gas gave different results from those with propane. The first experiments were carried out with 10% methane. Pointed cones with long, curled filaments grew from Substrate 1 (Fig. 11), while cones with larger cone angle grew with similar filaments from Substrate 2 (Fig. 12). Substrate 3 again supported less homogeneous growth (Fig. 13) in which a small number of cones were separated by filaments growing from the substrate.

When the methane concentration was dropped to 5%, the surface features changed. Substrates 1 and 3 grew cones of low surface density (~ 4 and $10 \times 10^{10}/\text{m}^2$ respectively) without long filaments (Fig. 14), whereas Substrate 2 showed a higher density ($\sim 4 \times 10^{11}/\text{m}^2$) with many

filaments (Fig. 15). There is the suggestion in this photograph that several cones grow together to form larger cones.

Discussion of Results

The results obtained in the present study are important because they indicate that the growth of filaments and cones from ion-bombardment of carbon surfaces is more complex than thought previously. The major results of the experiments can be summarized as:

1. The substrate is an important factor in the formation of surface features. Previous workers had shown that growth could not occur on diamond or glassy carbon (3), but the above results indicate that their shape and density are dependent on the type of graphitic carbon.
2. Hydrogen introduced into the plasma does not inhibit the growth of cones, producing straight filaments, nor does it effectively poison sites. Rather, the results show that the surface density of cones is increased, and the filaments are crooked.
3. The present results show that filaments can be grown from Ar/hydrocarbon plasmas, and that the growth depends on the hydrocarbon type and fraction. If the hydrocarbon fraction is too great, then sooty deposits form.
4. Filaments were observed to grow directly from the substrate without a supporting cone. However, these filaments were not straight.
5. The original experiment of Cuomo and Harper (1) could not be reproduced by us. It is evident that the present experimental

conditions differed from those in the original experiment, but we are unable to identify the relevant factors at the present time.

6. The original contract to Colorado State University and IBM was based on the observation of Cuomo and Harper (1) that sub-micron filaments of uniform diameter and high length-to-diameter ratios could be grown, with application to electromagnetic obscuration. However, none of the filaments that have been grown in our laboratory from ion-bombardment with either ion-guns or from plasmas have fulfilled these criteria. (Such filaments have been grown by us using chemical-vapor-deposition techniques.)

It is hard to reconcile the present results with the current model for the growth processes (4,5). This supposes that the ion beam initially smooths the surface, exposing nucleation sites (possibly screw dislocations). If the density of these sites is sufficiently low, and the ion beam density sufficiently high, then mobile atoms on the substrate surface become attached to these sites, supersaturate, and form growth features. (These surface atoms have much higher diffusion rates than normal due to the ion bombardment.) These features continue to grow through the continued attachment of mobile atoms on the surface, and by redeposition of sputtered atoms. In order to explain the increased density of growth features with increased temperature, it was postulated that sites are poisoned by a contaminant, probably H_2 and enhanced reactivity at higher temperature (methanation-type reactions) resulting in higher densities of active sites.

Some of the above principles appear to be contradicted by the present experiments:

1. The introduction of H_2 onto the plasma did not reduce the density of growth features but increased it. It is possible that atomic hydrogen above a critical concentration in the plasma assists the cleansing of the surface, thereby exposing further nucleation sites.
2. The shapes of the growth features were dependent on the substrate and the plasma. For instance, sharp and rounded cones were observed on different substrates, all other preparation parameters being the same.
3. The present results also suggest that filaments can grow directly from the substrate without a supporting cone. It is noted that this suggests that the electric field between the plasma and the substrate is not important in filament formation, since the field would be much higher at the tips of conical features than at the surface. Unfortunately, the present experiments do not give clues as to the conditions necessary for this phenomenon to occur. If this condition could be obtained, and straight filaments of uniform diameter grown, then the plasma method would be a useful technique for growing filaments for obscuration applications.

The above problems have not been resolved in terms of models. It is possible that computer simulations of the growth, which are about to be undertaken as part of the present program, will help to solve them.

References

1. J. J. Cuomo and J. M. E. Harper, IBM Tech. Discl. Bull. 20, 775 (1975).
2. R. S. Robinson and S. M. Rossnagel, J. Vac. Sci. and Technol. 21, 790 (1982).

3. J. A. Floro, S. M. Rossnagel, and R. S. Robinson. J. Vac. Sci. and Technol. A1, 1398 (1983).
4. J. A. Van Vechten, W. A. Solberg, P. E. Batson, J. J. Cuomo, and S. M. Rossnagel, IBM Res. Rep. C12010 (1986), to be published in J. Cryst. Growth.
5. W. A. Solberg, I. L. Spain, and N. E. Pedersen, Extended Abstracts. Biennial Conf. Carbon, p. 215 (1987).

Table 1. Experimental conditions for preparation of filaments using DC glow discharges.

Run	Plasma Gas	Plasma Condition
1	Ar	Voltage = 300-400 V Current = 4 A Time = 3-4 hours Gas Pressure = 3.8 μ m
2	Ar/10% H ₂	
3	Ar/5% H ₂	
4	Ar/9.25% propane	
5	Ar/5% propane	
6	Ar/10% methane	
7	Ar/5% methane	

Table 2. Substrates used.

Substrate	Material	Type	Manufacturer
1	Graphite	Poco AXF-5Q	Poco Inc.
2	Graphite	Poco ZXF-5Q	Poco Inc.
3	Graphite	Pyrolytic carbon	Pfizer
4	Si	Single crystal [(100) surface]	Monsanto

Figure Captions

- Fig. 1. SEM photographs of structure grown on Substrate 1 with pure Ar plasma: (a) 11,000x, (b) 45,000x magnification.
- Fig. 2. SEM photograph of growth features on Substrate 3 with pure argon plasma (9,100x).
- Fig. 3. SEM photograph of growth features on Substrate 1 from 95% Ar/5% H_2 plasma: (a) 5,000x, (b) 20,000x.
- Fig. 4. SEM photograph of growth features on Substrate 2 from 95% Ar/5% H_2 plasma at magnification of 20,000x, showing rounded cone tip and submicron diameter filaments.
- Fig. 5. SEM photograph of growth features on Substrate 3 from 95% Ar/5% H_2 plasma: (a) 1,300x, (b) 10,000x view of the transition region from (a).
- Fig. 6. SEM photograph of the large growth feature on Si from 95% Ar/5% H_2 plasma at 2,500x.
- Fig. 7. SEM photograph of the growth features from Substrate 3 using 90% Ar/5% H_2 plasma at 1,100x. The features only grow along the edges of the cracks.
- Fig. 8. SEM photograph of the soot-like features grown from 90.25% Ar/9.25% propane plasmas at 710x. Similar deposits were found on all substrates.
- Fig. 9. SEM photograph of filaments growing from the surface of Substrate 1 from 95% Ar/5% propane plasma at 36,600x.
- Fig. 10. SEM photograph of sharp cones and filaments growing from Substrate 2, 95% Ar/5% propane plasma, at 4,700x.
- Fig. 11. SEM photograph of sharp cones and filaments growing from Substrate 1, 90% Ar/10% methane plasma, at 5,000x.
- Fig. 12. SEM photograph of squat cones and curly filaments growing from Substrate 2, 90% Ar/10% methane plasma, at 10,000x.
- Fig. 13. SEM photographs of cones and filaments growing from Substrate 3, 90% Ar/10% methane plasma, at (a) 5,000x, (b) 20,000x, of filaments growing from surface.
- Fig. 14. SEM photograph of sharp cones growing from Substrate 3 from 95% Ar/5% methane plasma, at 1,000x.
- Fig. 15. SEM photograph of cones and filaments growing from Substrate 2, 95% Ar/5% methane plasma, at 10,000x.

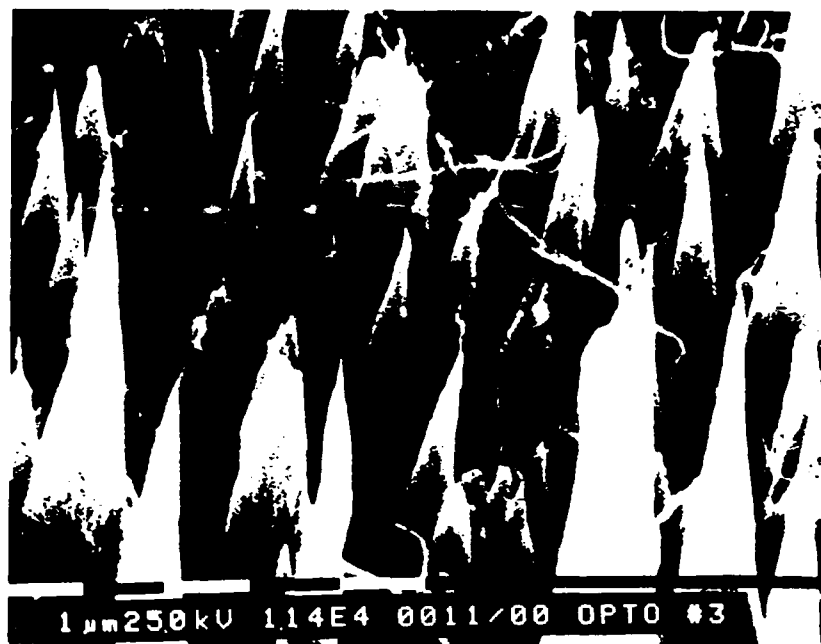


Fig. 1. SEM photographs of structure grown on Substrate 1 with pure Ar plasma: (a) 11,000x, (b) 45,000x magnification.

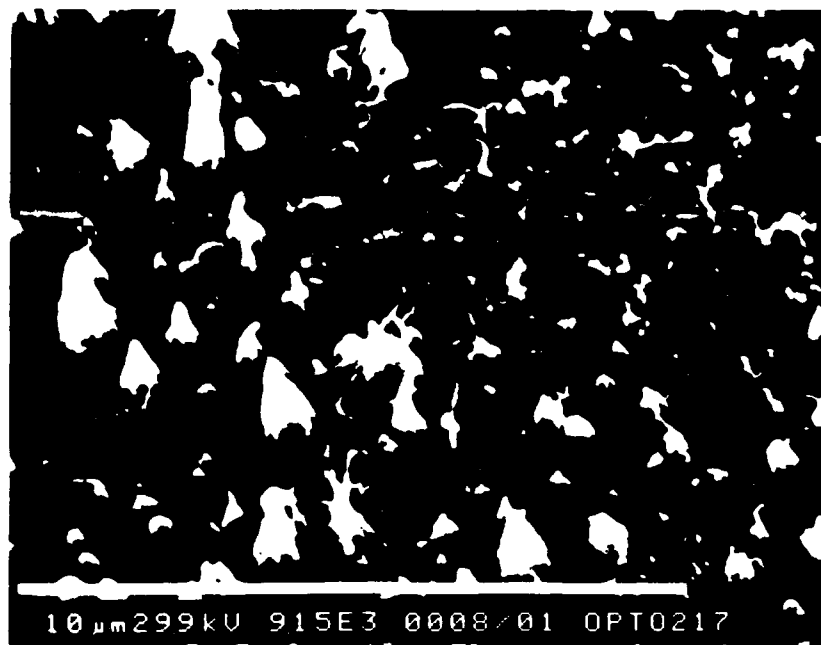


Fig. 2. SEM photograph of growth features on Substrate 3 with pure argon plasma (9,100x).

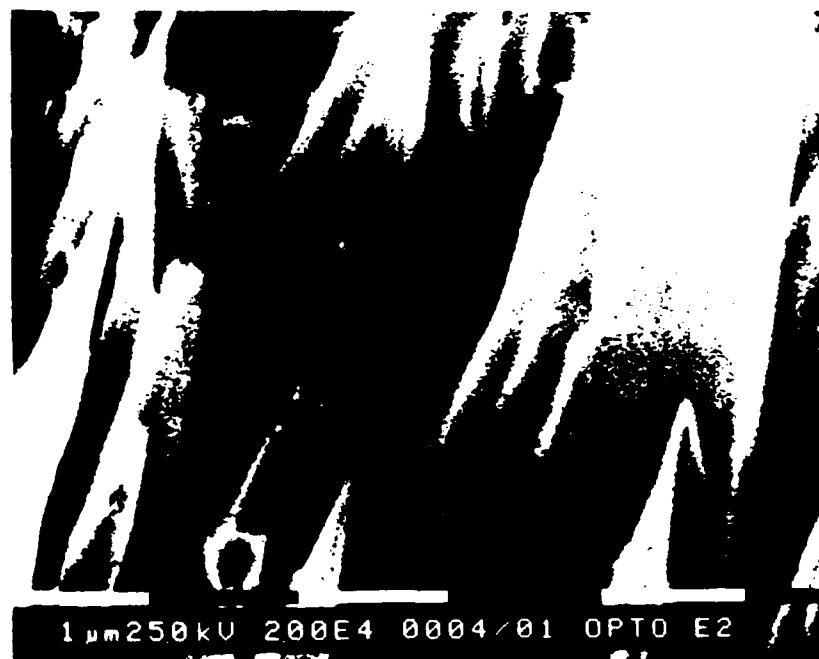


Fig. 3. SEM photograph of growth features on Substrate 1 from 95% Ar/5% H₂ plasma: (a) 5,000x, (b) 20,000x.



Fig. 4. SEM photograph of growth features on Substrate 2 from 95% Ar/5% H₂ plasma at magnification of 20,000x, showing rounded cone tip and submicron diameter filaments.

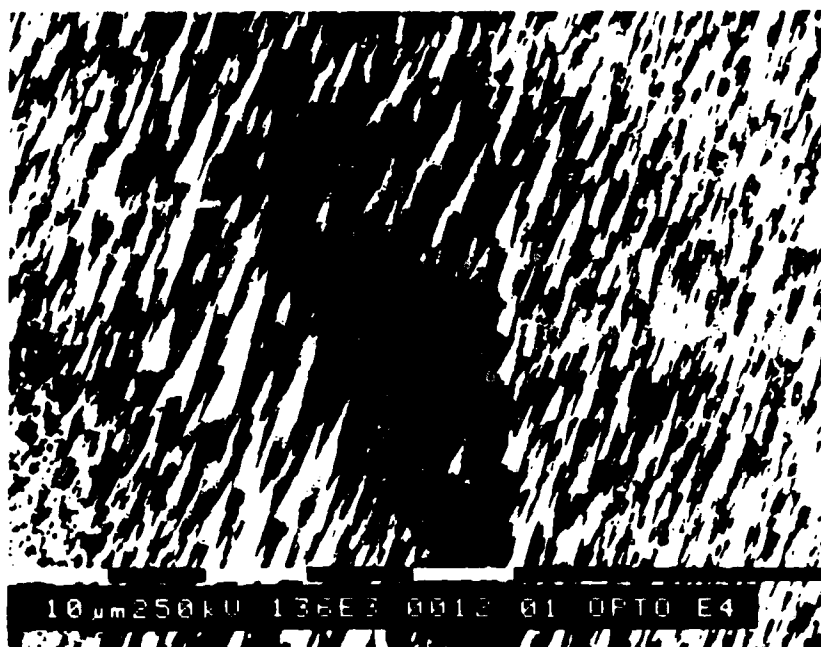


Fig. 5. SEM photograph of growth features on Substrate 3 from 95% Ar/5% H₂ plasma: (a) 1,300x, (b) 10,000x view of the transition region from (a).

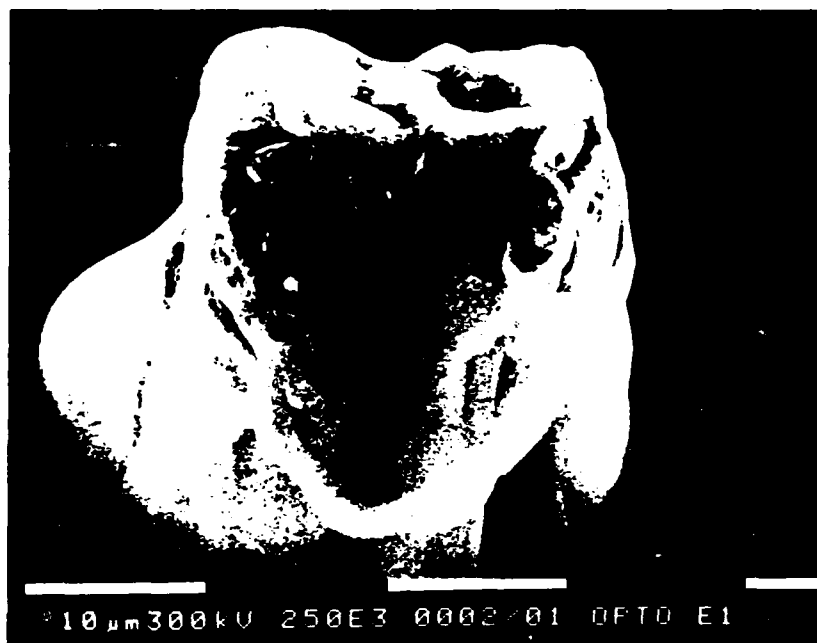


Fig. 6. SEM photograph of the large growth feature on Si from 95% Ar/5% H₂ plasma at 2,500x.



Fig. 7. SEM photograph of the growth features from Substrate 3 using 90% Ar/5% H₂ plasma at 1,100x. The features only grow along the edges of the cracks.



Fig. 8. SEM photograph of the soot-like features grown from 90.25% Ar/9.25% propane plasmas at 710x. Similar deposits were found on all substrates.



Fig. 9. SEM photograph of filaments growing from the surface of Substrate 1 from 95% Ar/5% propane plasma at 36,600x.



Fig. 10. SEM photograph of sharp cones and filaments growing from Substrate 2, 95% Ar/5% propane plasma, at 4,700x.

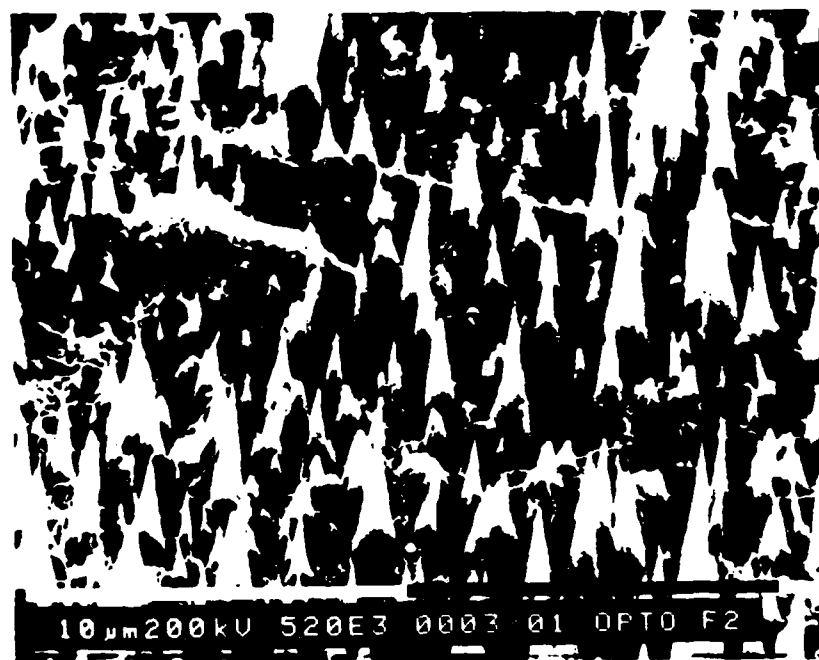


Fig. 11. SEM photograph of sharp cones and filaments growing from Substrate 1, 90% Ar/10% methane plasma, at 5,000x.

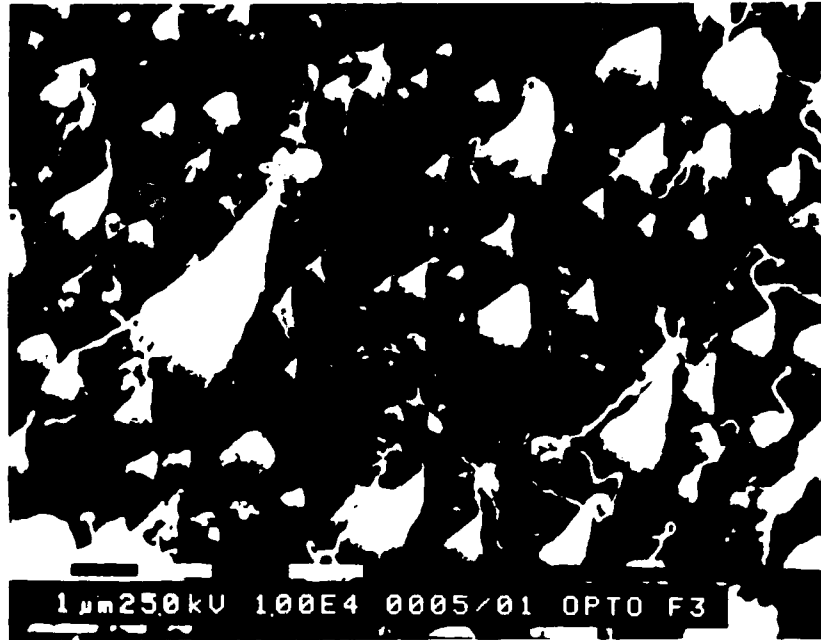


Fig. 12. SEM photograph of squat cones and curly filaments growing from Substrate 2, 90% Ar/10% methane plasma, at 10,000x.

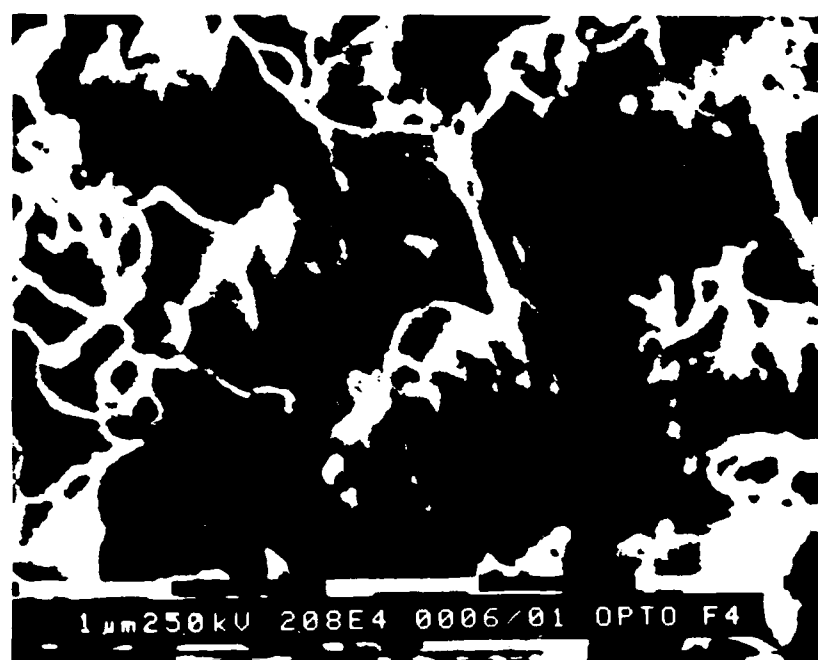
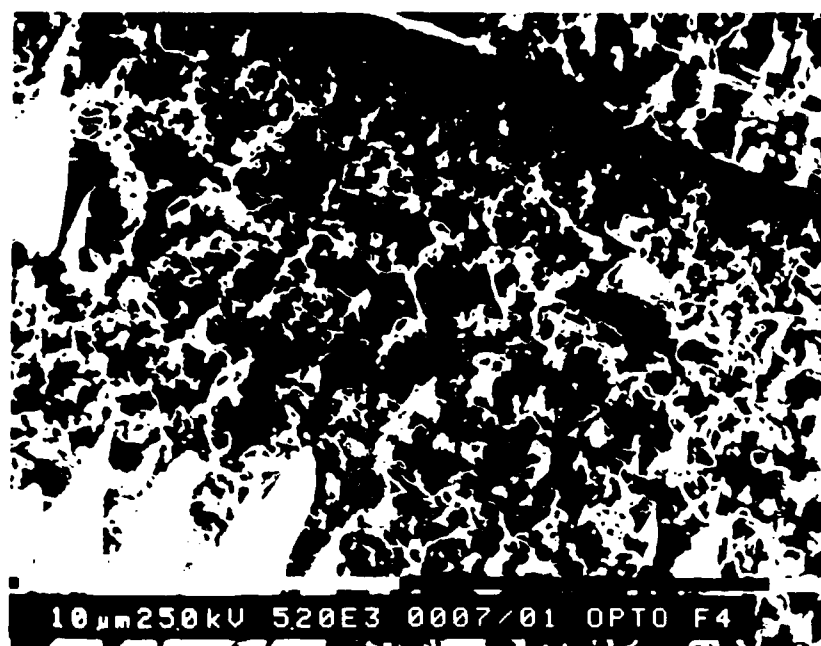


Fig. 13. SEM photographs of cones and filaments growing from Substrate 3, 90% Ar/10% methane plasma, at (a) 5,000x, (b) 20,000x, of filaments growing from surface.



Fig. 14. SEM photograph of sharp cones growing from Substrate 3 from 95% Ar/5% methane plasma, at 1,000x.

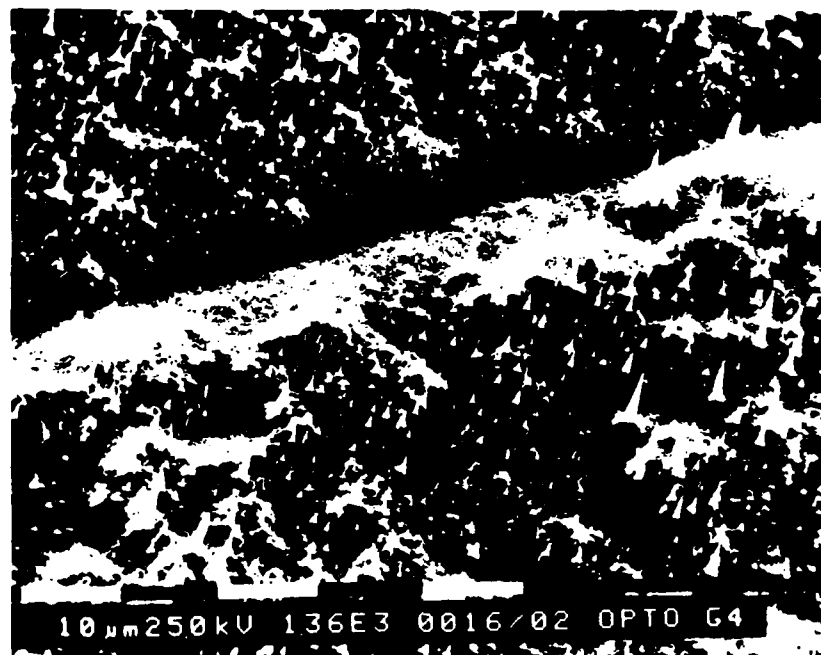


Fig. 15. SEM photograph of cones and filaments growing from Substrate 2, 95% Ar/5% methane plasma, at 10,000x.

III.1 ELECTRON MICROSCOPE STUDIES OF CARBON FILAMENTS

K. Baughman and C. M. McConica
Department of Chemical Engineering
Colorado State University
Fort Collins, CO 80523

T. McCormick
Electron Microscope Facility
Department of Anatomy
Colorado State University
Fort Collins, CO 80523

and

I. L. Spain
Department of Physics
Colorado State University
Fort Collins, CO 80523

Abstract

A program of study is underway to obtain structural information on CCVD carbon filaments. Experimental methods include scanning electron microscopy, energy-dispersive x-ray spectrometry, high-resolution transmission electron microscopy, electron diffraction in both selected-area and convergent-beam modes, and lattice-fringe imaging. This preliminary report discusses techniques and some results on filaments grown at 700 and 850°C.

Introduction

A number of different morphologies of carbon fibers have been described in the literature (e.g., Baird et al., 1971, Endo et al., 1977, Boellaard et al., 1985), and several different mechanisms of growth have been proposed. It is clear that structure is strongly controlled by growth conditions including catalyst particle, substrate, temperature, gas composition, flow rate, etc. A discussion and some results were given in the previous AFOSR Report (Spain, 1986). It is of interest to determine the relationship between structure of the carbon fibers and their growth conditions. It was decided to study the structure of the fibers in finer detail than can be seen in the scanning electron microscope (SEM) to compare different fibers grown under different, known, growth conditions.

The present report is of work in progress. One of the objectives was to train a graduate student (Kit Baughman) in techniques of transmission electron microscopy (TEM) and electron diffraction. This report outlines the steps we have taken to meet these objectives, the types of equipment and techniques employed, and some preliminary results.

Experimental Techniques

Structural characterization was undertaken using both scanning and transmission electron microscopy. The SEM used was a Philips 505, fitted with secondary and backscattered electron detectors and a Kevex Quantum (thin polymer window) solid state detector and Kevex 8000 multichannel analyzer for energy-dispersive x-ray spectrometry (EDS).

Substrates upon which fibers were grown were generally mounted on aluminum stubs and sputter-coated with gold for optimum imaging resolution. Most of the photomicrographs were taken using accelerating voltages of 25 kV and filament current of 0.03 mA. SEM was used primarily to determine the size characteristics of fibers after specific growth experiments, and results are described by Schmitt et al. in Section II.2 of this report.

The TEM used was a Philips 400T fitted with a scanning transmission (STEM) attachment and an EDAX solid state detector and Kevex 8000 multichannel analyzer for EDS. Most of the studies were undertaken with a 100 kV accelerating voltage. Images were recorded using low- and high-magnification modes, and high-resolution TEM (HRTEM) was performed to obtain structural information by lattice-fringe imaging. Electron diffraction patterns were obtained both in selected-area (SAED) and convergent-beam (CBED) modes. Selected-area diffraction employs parallel illumination and an aperture to eliminate diffracted electrons from outside the area of interest and can typically yield diffraction information from areas of 1 micron or more in diameter. In the CBED mode, a focussed probe was used together with a small condenser aperture to increase the resolution of the diffraction spots. A probe diameter of about 70 nm allowed diffraction patterns to be obtained from areas less than 100 nm across. Dark-field imaging uses one or more diffracted beams to form the image and was used to determine the region of the sample contributing to a particular diffraction pattern.

Filaments studied in transmission were prepared as follows: Material grown under known conditions was scraped off the substrate into absolute ethanol and put in an ultrasonic bath for several seconds to

several minutes. A drop of the suspension was then evaporated on a holey carbon support film on a 3-mm-diameter grid for TEM investigation. Five different samples were studied by TEM, and descriptions of each of these samples are given in the following section.

Experimental Results and Discussion

Standards

A number of standards were studied first to allow training of a graduate student (Kit Baughman) who will continue to work in this area. Polycrystalline aluminum and gold and single crystal graphite were among the materials studied to allow the microscopist to gain familiarity with TEM operation, diffraction techniques, and interpretation.

Fibers on Silicon Substrates

Material grown on silicon substrates at 700 and 860°C (Bowers et al., 1988) were examined by TEM. Much of the material on the substrate after the runs was flocculent material (Fig. 1) that showed diffraction patterns consistent with silicon carbide. Although EDS analysis has not yet been performed on the fibers grown on the silicon substrate, diffraction patterns from the fibers resemble turbostratic carbon and not crystalline silicon carbide. Further investigation of these fibers using EDS analysis and x-ray and electron diffraction is currently underway.

Fibers on Graphite Substrates: Sample RK #1

Typical distribution of size and morphology of CCVD filaments in this sample are shown in Fig. 2. These were grown previously (Spain, 1986, p. 41) at 850°C on a graphite substrate using a Technical grade acetylene and hydrogen 1:7 mixture for 20 minutes (total flow = 80 cc/min). The presence of acetone impurities in the acetylene may have had an effect on the growth.

In addition to relatively straight, feathery-structured filaments, there are a number of filaments that exhibit helical morphologies. They appear to have a uniform width of approximately 0.2 microns, but some of the fibers are helical along parts of their length and straight along other parts (Fig. 3). It has been surmised that twisting can occur as a result of a tilted, solid, catalyst particle (see Baker and Harris, 1978, for a review). Diffraction patterns showed these fibers to be turbostratic but with no preferred orientation.

The feathery-structured fibers in this sample are composed of turbostratic carbon showing strong preferred orientation. Figure 4 shows typical fibers of this type together with microdiffraction patterns (CBED) of either side of the fiber. Analyses of diffraction patterns indicate that graphitic c-axes are oriented more or less parallel to the "branches." These results are consistent with observations of Boellaard et al. (1985). Many of the fibers show v-shaped fractured ends, also observed by Boellaard et al. and interpreted to be (002) cleavage surfaces. Separation of the "branches" is also evident in many of the fibers, particularly at the edges. The fibers also commonly show a core of less dense material, or possibly a hollow core. No catalyst particles were observed in these fibers.

Boellaard et al. (1985) proposed a model for growth of these feathery type of fibers whereby carbon is excreted at the interface between the fiber and a solid, conical-shaped catalyst particle so that conical graphitic layers are parallel to this interface. Since the growth direction is oblique to the graphite planes, edge dislocations are introduced. Therefore, these areas of well-ordered graphitic carbon may be separated by areas in which there is local structural disorder. The separation of the branches at the edges of the fibers may result from structural weakness in these disordered zones.

Graphite Substrate: Sample #A1

This sample (see Section II.1 of this report) was prepared by passing a 50:1 hydrogen/acetylene mixture at 600°C over a AXF-5Q graphite substrate. SEM did not reveal any fiber growth, so TEM was used to determine the presence of fibers. Very short fibers were observed in flocculent material on the substrate.

Silica Substrate: Sample #4

This sample was prepared (see Section II.1 of this report) by passing a 10:1 hydrogen/acetylene mixture over powdered silica with Ni catalyst at 850°C. No fibers were observed in the TEM, and only flocculent material was present.

Graphite Substrate: Sample #3-I

Fibers were grown on AXF-5Q graphite substrate using Ni as a catalyst (see Section II.1 of this report) by passing a 10:1 hydrogen/acetylene mixture over the substrate at 850°C. Very thin and

long fibers are present in this sample (Fig. 5), along with graphitic non-fibrous carbon. The fibers are typically about 25-35 nm wide and appear to have hollow cores 20-30 nm in diameter. The outer parts of the fibers are seen in Fig. 5 to have variable contrast resulting from a range of orientations, the darker parts being in a strong diffraction condition. This suggests that the fibers have crystalline edges with strong preferred orientation. Due to the reduced thickness of these fibers, HRTEM was possible. Graphitic fringes (0.34 nm) are shown in Fig. 6 to be parallel to the length of the fiber. Some of the graphite layers can also be seen peeling away from the wall of the fiber toward the center. These fibers are similar to those described by Baird et al. (1971). No catalyst particles were seen in this sample, although further work is currently in progress.

References

- Baird, T., J. R. Fryer, and B. Grant (1971) Structure of Fibrous Carbon. *Nature* 233, 329-330.
- Baker, R. T. K. and P. S. Harris (1978) Chemistry and Physics of Carbon 14, 83.
- Boellaard, E., P. K. de Bokx, A. J. H. M. Kock, and J. W. Geus (1985) The Formation of Filamentous Carbon on Iron and Nickel Catalysts--III. Morphology. *J. Catalysis* 96, 481-490.
- Endo, M., A. Oberlin, and T. Koyama (1977) High Resolution Electron Microscopy of Graphitization Carbon Fiber Prepared by Benzene Decomposition. *Japan. J. Appl. Phys.* 16, 1519.
- Spain, I. L. (1986) Final Report to AFOSR, "Carbon Whisker Study" (Contract #F49620-34-K-0006).
- Zhao, Y. X., C. W. Bowers, and I. L. Spain (1988) "Graphitic Nature of Chemical Vapor-Deposited Carbon Filaments Grown on Silicon Surfaces from Acetylene" to be published in *Carbon* (and p. 50 in Spain, 1986).

Figure Captions

- Fig. 1. TEM image of flocculent material on silicon substrate. Scale bar = 5000 Å.
- Fig. 2. TEM image showing the range of fiber morphologies grown on graphite substrate. Scale bar = 2 microns.
- Fig. 3. TEM image of a single straight carbon fiber with helical ends. Scale bar = 5 microns.
- Fig. 4. Feathery type of carbon fibers. (a) TEM image showing (002) cleavage on fractured end (upper left) and branching structure of fibers. A paler line running down the center of the fibers suggests a hollow core. Scale bar = 5000 Å. (b) Higher magnification TEM image of fiber in (a). Microdiffraction pattern from upper left of the fiber is shown in the upper left corner, microdiffraction from the lower, right side of the fiber is shown in the lower right. Scale bar = 1000 Å.
- Fig. 5. Thin carbon filaments on graphite substrate together with non-fibrous graphitic carbon. Scale bar = 1000 Å.
- Fig. 6. HRTEM image of carbon filament showing 3.4 Å fringes on the edges of the fiber. Scale bar = 100 Å.



Fig. 1. TEM image of flocculent material on silicon substrate. Scale bar - 5000 Å.



Fig. 2. TEM image showing the range of fiber morphologies grown on graphite substrate. Scale bar - 2 microns.



Fig. 3. TEM image of a single straight carbon fiber with helical ends.
Scale bar = 5 microns.



Fig. 4. Feathery type of carbon fibers. (a) TEM image showing (002) cleavage on fractured end (upper left) and branching structure of fibers. A paler line running down the center of the fibers suggests a hollow core. Scale bar = 5000 Å. (b) Higher magnification TEM image of fiber in (a). Microdiffraction pattern from upper left of the fiber is shown in the upper left corner, microdiffraction from the lower, right side of the fiber is shown in the lower right. Scale bar = 1000 Å.



Fig. 5. Thin carbon filaments on graphite substrate together with non-fibrous graphitic carbon. Scale bar = 1000 Å.

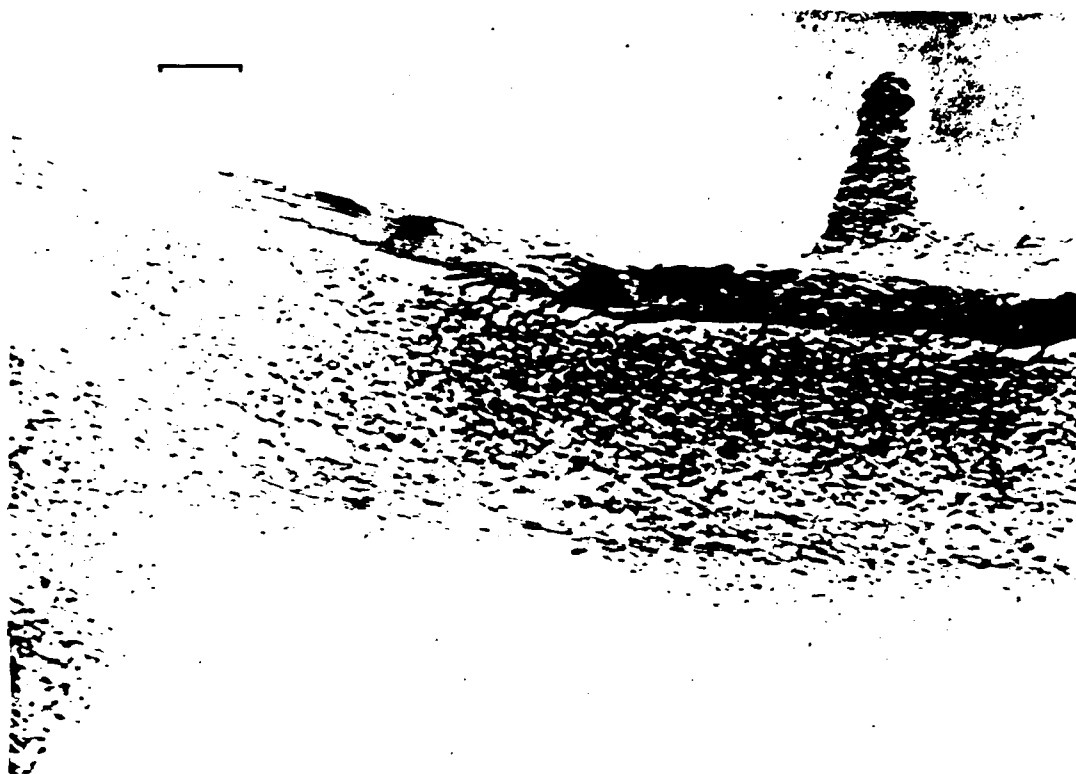


Fig. 6. HRTEM image of carbon filament showing 3.4 Å fringes on the edges of the fiber. Scale bar =100 Å.

III.2 RELATIONSHIP BETWEEN STRUCTURAL, ELASTIC AND PIEZO-ELECTRIC PROPERTIES OF CARBON FIBERS

Harris A. Goldberg, F. Haimbach, and James Stamatoff
Celanese Research Company
86 Morris Avenue
Summit, New Jersey 87901

and

Ian L. Spain
Department of Physics
Colorado State University
Fort Collins, Colorado 80523

Abstract

The piezo-resistance coefficient of several ex-PAN and ex-pitch carbon fibers has been obtained at room temperature. The coefficient is positive for poorly graphitized fibers with low values of Young's modulus, and falls to increasingly negative values as the graphitization index and Young's modulus increases. A model which qualitatively explains the observed trends is presented, based on geometrical and electronic contributions to the coefficient. Structural and mechanical data are also presented, allowing the parameters of interest to the above model to be evaluated.

Introduction

The electrical resistance of carbon fibers was considered by us in a previous paper (1). The present paper considers the piezo-resistance (PR), which is defined as the change of the resistance which occurs when the fiber is strained longitudinally. The piezo-electric coefficient (PRC) is then the relative change of the resistance per unit longitudinal strain. This coefficient depends on the fiber's structural and elastic properties, so that this paper will also consider these data and their interrelationships.

Consideration was given in ref. 1 to fibers prepared by the heat-treatment of polyacrylonitrile (ex-PAN fibers). This type of carbon fiber accounts for most of the present commercial production. Several other types of carbon fibers are reviewed in ref. 2. Among them are those prepared from a liquid-crystal state (mesophase) of pitch fractions, called ex-mesophase pitch fibers. The present paper will also consider the PR properties of these fibers.

Early work on the PR of ex-PAN fibers (3-6) indicated a complex behavior. Firstly, the changes in resistance occurring at strains less than about 0.1% were erratic, indicating that irreversible changes in contacts between carbon ribbons were occurring. (This is similar to behavior found in the c-axis resistance of highly-oriented pyrolytic graphite when subjected to hydrostatic pressure (7)). Most of the fibers showed an approximately linear change of resistance above 0.1% strain. More recent data obtained on ex-mesophase pitch fibers (8) showed that the PR was reversible and reproducible until strains approaching the breaking strain were approached. This was attributed to

the formation of microcracks just prior to failure. Only the reproducible effect between these strain limits will be considered in this paper.

One possible cause of the piezo-resistance is that the dimensions of the fibers change as a function of applied stress. This effect would contribute a positive term to the PR, and the experimental results show that the PR coefficient only tends to be positive for low-modulus fibers, and is negative for those with high modulus. This is the case for ex-PAN, ex-mesophase pitch and catalytic-chemical-vapor-deposited fibers (9). Other explanations for the change in the resistance can be related to inter-particle contacts (6), changes of the orientation of fibers under stress (10), or electronic effects (11).

In order to separate these effects it is necessary to consider the structure of the fibers, the relationship of the structure to the elastic behavior, and then calculate the PR using models. This is basically the approach adopted in this paper. X-ray data will be presented first, allowing the orientation distribution function and the degree of graphitization of the carbon ribbons to be determined. Then, data on the Young's modulus, E_Y , of the fibers are presented, and fitted with the uniform-stress model. Finally, the PR data are presented and compared to models using these structural and mechanical data.

Preliminary Discussion of Fibers Tested

As mentioned above, two types of fiber were examined in this work. Firstly, ex-PAN fibers were selected with a wide range of E_Y values described in Table 1. The moduli are mainly controlled by increasing

the temperature of heat-treatment (T_{HT}) from about 1300°C ($E_Y = 230$ GPa), to >3000°C ($E_Y = 690$ GPa). Table 1 also includes values of the moduli which are somewhat higher than values usually quoted, since they are corrected for the porosity of the fibers as well as the compliance of the testing equipment. These data are discussed in Section III. It is important to note that other factors than T_{HT} are important in determining the structure and the mechanical properties, such as the orientation, microstructure, and chemical composition of the PAN fiber before carbonization and subsequent heat-treatment. For this reason, it is not possible to specify a fiber from its precursor type and T_{HT} . This causes much confusion in the literature, since the properties of fibers prepared by even the same manufacturer can change over a period of years as small improvements are made to processing procedures.

The structural parameter that controls E_Y is the alignment of the ribbons. The aromatic macromolecules in ex-pitch fibers align during the formation of the mesophase and extrusion processes more readily than the polymer chains in ex-PAN fibers. This alignment increases in both fiber types with T_{HT} , so that E_Y increases, although ex-mesophase pitch fibers typically have higher elastic moduli than ex-PAN fibers which have seen the same T_{HT} .

The structure of both types of fibers is now understood reasonably well, and is reviewed in refs. 12 and 13 (ex-PAN) and 14 (ex-pitch). Ribbons of carbon atoms in hexagonal form, called graphene planes, are roughly aligned with the fiber axis. These ribbons are more extensive along the fiber axis, but less so perpendicular to it. For example, high strength ex-PAN fibers ($T_{HT} = 1300^\circ\text{C}$) have ribbons at least several

μm long and tenths of μm wide. These dimensions tend to increase with T_{HT} . The ribbons undulate slightly along their lengths and more so perpendicular to the axis (see refs. 15 and 16 for models). X-ray diffraction experiments can be interpreted to give "crystallite dimensions" which are considerably less than those obtained from electron microscope studies (lattice fringe images), and are interpreted as giving information about the lengths of relatively straight portions of the ribbons. However, the stacking height of the ribbons obtained from x-ray studies, called L_c , gives values in agreement with those from electron microscope studies. Typical values are in the range of 20-200 Å as T_{HT} increases from 1000-3000°C.

The manner in which the ribbons are arranged across the fiber section varies considerably from one fiber type to another. Ex-PAN fibers are characteristically disordered in this section, whereas ex-mesophase pitch fibers often have a radial or onion-skin arrangement (17). This distribution can be modified by stirring the pitch blend prior to extrusion (18), but such fibers will not be considered here. The manner in which the graphene planes are stacked in all of these fibers is consistent with a lack of complete c-axis stacking correlation (19). Complete lack of correlation is termed turbostratic packing. The correlation increases with T_{HT} more readily in ex-mesophase pitch fibers than ex-PAN fibers, but a completely graphitic stacking sequence (perfect ABAB...stacking) is not achieved in ex-mesophase pitch fibers even though T_{HT} is as high as 3500°C (17). Partially turbostratic layer stacking can be characterized from the average separation of the planes, obtained from the d_{002} spacing, taking

values from 3.354 Å for graphite to 3.44 Å for turbostratic carbon (for a review see Ref. 20).

These ribbons enclose a complicated network of elongated pores. Information about pore sizes can be obtained from low-angle x-ray scattering (21,22), and are similar for ex-PAN and mesophase pitch fibers with similar T_{HT} values (23). The pores are elongated along the fiber axis, with much greater lengths than widths (typical ratios are 10), while the sections are also non-circular, as expected for pores which are bounded by flat graphene planes (23). Although the pore size increases with T_{HT} , the density, which is well below the value for graphite, increases. The density of ex-mesophase pitch fibers is generally higher than that for ex-PAN with the same T_{HT} .

Although the structure is understood reasonably well, it is emphasized that there are differences between different fibers produced by different manufacturers, and even by the same manufacturer, as noted above. It is for this reason that all data used in modeling fiber properties in the present paper have been obtained experimentally.

Structural Analysis of Carbon Fibers

Experimental Techniques and Results

The structure of several ex-PAN and ex-mesophase pitch fibers were studied using x-ray diffraction and low-angle scattering methods. The fibers were mounted in thin glass capillaries, and rotated in the incident beam about an axis at right angles to it. Diffraction data were obtained using flat photographic plates, and intensity data then read using a Joyce-Lobel microdensitometer. These profiles were

transmitted to a computer and analyzed to give information about the alignment of c-axes, the c-axis stacking height, L_C , and the degree of graphitization, as described below.

Typical experimental diffraction data for ex-PAN fibers with Young's moduli of approximately 30, 50, 70, and 100 Msi respectively (approximately 200, 350, 500 and 700 GPa) are shown in Fig. 1, and for ex-pitch fibers with Young's moduli of 50, 70, and 100 Msi (350, 500 and 700 GPa) in Fig. 2. The photographs are exposed to high density in order to reveal the higher-order diffractions. The data for the ex-PAN fibers are typical of heat-treated carbons which do not completely graphitize, while the ex-pitch fibers tend to graphitize somewhat more readily, but not completely, even for values of T_{HT} as high as 3500°C (17).

Graphitization

Several of the features seen in the diffraction photographs are due to the poor interlayer correlations. Considering a short length of the fiber in the beam (Fig. 3), all orientations of the c-axes are present within the perpendicular plane. In addition all possible orientations of the a-axes are present, due to the presence of defects in the graphene planes. If the fibers were graphitic (i.e., with well-developed interplanar correlations) these reflections would be spread into rings, with intensity falling from the equator to zero at the poles (Fig. 3b). If the fiber were turbostratic (no interlayer correlations), the (hkl) reciprocal lattice spots would be replaced by rods parallel to the (001) axis. One such rod would pass through the (110) and (112) reciprocal lattice points, so that these reflections could not be

resolved. These rods would form cylinders as a result of the a-axis disorder, and these cylinders would be rotated about the $(00l)$ axis, since all c-axis orientations about the fiber axis are present. Thus, (hkl) reflections are smeared out, with asymmetric line shapes (Fig. 3d) and an increasing degree of turbostratic disorder can be monitored by the disappearance of (hkl) reflections, which cannot be resolved for turbostratic carbon.

The most basic information about the degree of graphitization can be derived from the increase of the interlayer separation, obtained from the (002) reflection. Fig. 4 summarizes the data of interlayer separations obtained here, and compares them with previous work. These data suggest that ex-pitch fibers graphitize more readily than ex-PAN, as noted by many previous studies (see 2).

This trend is also supported by traces of the (110) and (112) reflections along the equatorial plane, which are illustrated in Fig. 5. The diffraction profile of a completely turbostratic fiber would be similar to that shown in Fig. 5 for the ex-PAN fiber with $E_Y = 120$ GPa. Note, however, that these reflections are resolved in the 690 GPa fiber, although the graphitization process is not complete, since the intensity of the (112) reflection should be higher than that of the (110) . Similar curves were obtained for the ex-pitch fibers.

Measurement of the widths of higher order $(00l)$ reflections of pyrolytic carbons (25) suggest that they are broadened by liquid-like disorder (i.e., disorder of the second kind, or paracrystalline disorder) as well as from effects due to crystallite size, L_C (see below). This type of behavior is also seen in the $(00l)$ linewidths of fibers. Fig. 6 summarizes the equatorial linewidths of (002) and (004)

reflections of the four types of ex-PAN fibers plotted against ΔK , where ΔK is the magnitude of the wavevector difference between scattered and incident x-rays ($K_d - K_o$). It can be seen that the liquid-like disorder, as monitored by the slopes of these curves (24), increases as E_Y increases (19).

These structural results are consistent with a model in which the interlayer correlation function approaches that of perfect graphite gradually and homogeneously through the entire fiber. The data are not consistent with a model in which regions attain perfect crystallinity, and that the volume fraction of these crystallites then increases as T_{HT} increases. (The present data cannot rule out the possibility that some small regions are graphitic, as discussed in Refs. 26 and 27 to account for the fracture of fibers. We are unable at the present time to put a figure on the maximum possible volume fraction of such regions which would remain consistent with the present data.) This feature of gradual, homogeneous approach to the graphitic state is suggested by the model of Ruland (28) in which the interlayer correlations are expressed by an order parameter, σ_{12} , which represents the mean-squared fluctuation in the registry of adjacent layer planes. It might be expected that the intensity of the (112) reflection would be proportional to σ_{12} , but the present data are not sufficient to test this.

Alignment of Ribbons

It is noted that the (00 l) reflections are not affected by turbostratic disorder, but are broadened by lattice disorder, and smeared into arcs by the angular distribution of the c-axes about the

perpendicular planes (Fig. 3c). A distribution function $P(\phi)$ expresses the probability that the c-axis of a local region occurs at an angle ϕ to the perpendicular to the fiber axis. Thus, ϕ is the angle that the graphene plane makes with the fiber axis (Fig. 7). This distribution function is one of the parameters of interest to the present measurements, and is measured by scanning the (00 l) diffraction profiles in the meridions. Experimental data for (002) profiles, which are normalized to constant integral intensity, are shown in Fig. 8. It is also noted that the d-spacings decrease with increasing T_{HT} , as noted above.

It is usual to analyze this distribution for carbons using a function of the form (27)

$$P(\phi) = \text{Constant} \cos^m \phi \quad [1]$$

where m is a constant. However, this distribution is characterized by the equality of the full width at half maximum (FWHM) and the full width at half integral intensity (FWHII), whereas the experimental results did not support this (Table 1). A better fit was obtained using a Gaussian expression, for which $\text{FWHM} = 1.74 \text{ FWHII}$. (It is noted that Ruland used a similar expression of the form of a Poisson kernel (28).

The expression $\text{FWHM} = 2\langle\phi\rangle$ is often used to give an estimate of the mean c-axis misorientation $\langle\phi\rangle$. A trend of decreasing $\langle\phi\rangle$ with increased T_{HT} has been observed for ex-PAN fibers over a more limited range of E_Y values (29), and for ex-pitch fibers (17). These and the

present data are compared in Fig. 9. It will be seen in Section IV that it is this parameter that controls the increase of E_Y with T_{HT} .

Ribbon Stacking Height

(00 ℓ) reflection profiles in the equatorial plane were analyzed to give the stacking height of the graphene planes, L_C , using the Scherrer formula

$$L_C = \frac{\lambda}{B_{002}(2\theta) \cos\theta} \quad [2]$$

where $B_{002}(2\theta)$ is the full width at half integral intensity (FWHII) of the (002) reflection, with Bragg angle θ , and λ is the incident x-ray wavelength.

Figure 10 summarizes the variation of L_C with T_{HT} for the present work, compared with other data. These data illustrate the point made earlier that properties of ex-PAN fibers, for instance, can vary from one manufacturer to another. Note that the L_C values of Johnson (30) are somewhat lower than the present, probably due to differences in precursor polymer and other details of the preparations.

Mechanical Properties

The extensional moduli, E_Y , of the fibers were measured using standard techniques. Values obtained are given in Table 1. These values are somewhat higher than those normally quoted, for similar fibers, since the compliance of the testing fixture was corrected for. Also, these values were corrected for the porosity of the fibers using

measured values of the density, also recorded in Table 1. In these corrections it was assumed that the ideal density of the fiber could be obtained from the x-ray values of the interlayer spacing, assuming perfect graphene planes.

There are two basic problems that have to be solved in modeling the elastic behavior of fibers. The first is to relate the elastic constants of the ribbons to those of the fiber using structural models. The second is obtaining reasonable values of the elastic parameters of the ribbons. Neither of these problems has been solved completely.

Two different models have been proposed to explain the dependence of E_Y on the mean misorientation angle $\langle\phi\rangle$. Ruland (27) proposed an "elastic unwrinkling" model, in which the long, undulating ribbons of the fiber straighten with applied stress. Contiguous ribbons exert a stress on each other, which resists this straightening. E_Y was written as

$$\frac{1}{E_Y} = \ell_Z S_{11} + m_Z k_e \quad [3a]$$

$$\ell_Z = \int I(\theta) \sin^2 \theta d\theta / \int I(\theta) \sin \theta d\theta \quad [3b]$$

$$m_Z = \int I(\theta) \cos^2 \theta d\theta / \int I(\theta) \cos \theta d\theta \quad [3c]$$

where $\theta = 90^\circ - \phi$, and $I(\theta)$ is the x-ray distribution function. The elastic compliance parameter, k_e , was not defined in terms of measurable parameters, but was empirically found to be approximately independent of

fiber type (28). Although this model is physically appealing due to its simplicity, it will not be considered further, since k_e is not defined.

Another approach is to use uniform stress (Ruess) or uniform strain (Voigt) averages over the crystallites of the fiber. Expressions for these cases were obtained by Price (31) and Goggin and Reynolds (32) for graphite. These are upper and lower bounds for the elastic energy of the system, respectively, and would be expected to differ appreciably for an anisotropic system such as graphite. It would be anticipated, however, that the uniform stress model would be more appropriate to a fiber than uniform strain, since the ribbons are nearly aligned along the fiber axis, and extend considerable distance. This model has been found to account well for the measured values of E_Y (27), and to explain the considerable stiffening that occurs in this parameter with applied stress (10). This model will be used to analyze the present data.

In principle, a simple model should also allow the torsional modulus of the fiber to be fitted. However, this parameter is very sensitive to the manner in which the ribbons are packed together across the fiber section. This can be understood simply by considering the torsional modulus of strips of metal. One value would be obtained if the strips were held loosely parallel, another if they were brazed together, yet another if they were brazed to form a square section, etc. Many different arrangements of the ribbons can occur, as discussed briefly in Section II. In addition, the curvature, or wrinkling of the ribbons across the section can stiffen the torsional modulus considerably. As a result of the structure-sensitivity of this parameter no measurable models have yet been developed.

The second problem is to choose a reasonable set of parameters to express the elasticity of the crystallites. There are five independent elastic stiffnesses needed to specify the elastic behavior of graphite, C_{11} , C_{12} , C_{13} , C_{33} , C_{44} , and their corresponding compliances, S_{ij} (see ref. 32 for a review). Currently accepted values of the elastic parameters of single crystal graphite are listed in Table 2. In graphite fibers one would expect the following:

C_{11} and C_{12} (S_{11} and S_{12}) are not expected to depend strongly on structural details such as the degree of interplanar correlation. A decrease of about 10% might be anticipated as a result of vacancies and vacancy loops in the graphene planes.

C_{13} (S_{13}) is expected to be sensitive to defects, but it would be difficult to ascertain the trend. This parameter is not known with precision, and it is fortunate that E_y is not sensitive to it.

C_{33} (S_{33}) is expected to be sensitive to c-axis stacking order, since it is a measure of the strength of the interplanar bonds. It is probable that a scaling relationship can be established with the interplanar separation, \bar{c} . A fiber with $\bar{c} = 0.340$ A was found to have a value of C_{33} which was 15% below that of single crystal graphite (35). Even smaller values might be anticipated for fully turbostratic fibers with $\bar{c} = 0.344$ A (higher values of \bar{c} can occur due to the presence of interstitials).

C_{44} (S_{44}) is known to be extremely sensitive to the density of basal dislocation pins (36), and should therefore be sensitive to defects in fibers. Other factors affecting this parameter will be the value of \bar{c} , and the curvature of the graphene planes (in such a case it is inappropriate to use elastic constants for a hexagonal system). It

will be seen that the value of S_{44} is important in determining the value of E_Y .

The Uniform Stress Model

The elastic parameters of the fiber are calculated by considering the relationship between stress and strain for a crystallite oriented at an angle ϕ to the fiber axis, then averaged over all crystallites using a suitable average. In the case of uniform stress, every crystallite is subjected to the applied stress, and the strain is then averaged using the crystallite orientation function derived from the x-ray diffraction measurements. It is instructive to rederive the expression for E_Y using a different method to those in Refs. 31 and 32, and to derive other quantities of interest for the first time.

For simplicity, we will define the primed coordinates pertaining to the whole fiber as follows:

- the 2' axis is parallel to the fiber axis;
- the 3' axis is perpendicular to the fiber surface;
- the 1' axis is in the basal plane of the crystallite and is identical to the 1 axis.

The unprimed coordinates are defined in terms of the crystalline axes as follows:

- the 1 and 2 axes are in the basal plane of the crystallite;
- the 3 axis is parallel to the c axis of the crystallite.

The relationship between the stresses and strains is found by rotating the stress and strain tensors through an angle ϕ about the 1 axis; i.e.

$$\epsilon_{i'j'} = \sum_{i,j} R_{i'i}(\phi) \epsilon_{ij} R_{jj'}(-\phi) \quad [4]$$

where

$$R(\phi) = \begin{pmatrix} 1 & 0 & 0 \\ 0 & \cos \phi & \sin \phi \\ 0 & -\sin \phi & \cos \phi \end{pmatrix} \quad [5]$$

(Note that the more general case of rotations to a completely arbitrary orientation of a crystallite must be used for some problems--such as understanding the effects of not having azimuthal symmetry in a fiber.)

Similarly for the stress tensor, we have the relation:

$$\sigma_{Ti'j'} = \sum_{i,j} R_{i'i}(\phi) \sigma_{Tij} R_{jj'}(-\phi) \quad [6]$$

and thus it follows that

$$\epsilon_{ij} = \sum_{kl} S_{ijkl} \sigma_{Tkl} = \sum_{klk',l'} S_{ijkl} R_{kk'}(\phi) \sigma_{Tk'l'} R_{l'l}(-\phi). \quad [7]$$

In tensile stress experiments, $\sigma_T = 0$ except for $\sigma_{T2'2'}$, so that in this case:

$$\epsilon_{ij} = \sigma_{T2'2'} \sum_{kl} S_{ijkl} R_{k2}(\phi) R_{2l}(-\phi). \quad [8]$$

Using this model, Young's modulus is given by:

$$\begin{aligned} 1/E_Y &= \langle \epsilon_{2'2'} \rangle / \sigma_{T2'2'} = \sum_{ij} \langle R_{2i}(\phi) \epsilon_{ij} R_{j2}(-\phi) \rangle \\ &= \langle \sum_{ijkl} S_{ijkl} R_{2i}(-\phi) R_{j2}(\phi) R_{k2}(\phi) R_{l2}(-\phi) \rangle, \end{aligned} \quad [9]$$

so that

$$\begin{aligned} 1/E_Y = S_{11} + (2S_{13} + S_{44} - 2S_{11})\langle \sin^2 \phi \rangle \\ + (S_{11} + S_{33} - 2S_{13} - S_{44})\langle \sin^4 \phi \rangle \end{aligned} \quad [10]$$

We can also derive an expression for the change in cross sectional area of a fiber under uniaxial tension (i.e., the Poisson ratio ν)

$$2\nu = \frac{\text{change in area/area}}{\text{longitudinal strain}} = (\epsilon_{1'1'} + \epsilon_{3'3'})/\epsilon_{2'2'} \quad [11]$$

to obtain

$$\begin{aligned} 2\nu = E_Y [S_{12} + S_{13} + (S_{11} + S_{33} - S_{44} - S_{12} - S_{13})\langle \sin^2 \phi \rangle \\ + (2S_{13} - S_{33} + S_{44} - S_{11})\langle \sin^4 \phi \rangle] \end{aligned} \quad [12]$$

The torsional modulus will depend on the details of the azimuthal distribution of crystallites as discussed above. When that distribution is completely random, one obtains for the torsional modulus (32):

$$\begin{aligned} 1/G = (0.5S_{44} + S_{11} - S_{12}) + (S_{11} + 2S_{33} + 12S_{13} - 1.5S_{44})\langle \sin^2 \phi \rangle \\ - (2S_{11} + 2S_{33} - 4S_{13} - 2S_{44})\langle \sin^4 \phi \rangle. \end{aligned} \quad [13]$$

The above solutions (i.e., Eqs. 10 and 12) can be simplified for the case of perfectly aligned crystallites ($\phi = 0^\circ$), for which

$$E_Y = S_{11}^{-1} \quad \sim 1020 \text{ GPa}$$

$$2\nu = E_Y(S_{12} + S_{13}). \quad [14]$$

The angular averages in Eqs. 10 and 12 are defined (31) simply in terms of the measured crystallite orientation functions $I(\phi)$

$$\langle \sin^n \phi \rangle = \int_{-\pi/2}^{\pi/2} I(\phi) \sin^n \phi \cos \phi \, d\phi / \int_{-\pi/2}^{\pi/2} I(\phi) \cos \phi \, d\phi. \quad [15]$$

The angular averages are sensitive to the tails of the distribution functions. The tails are difficult to determine with precision from the experimental data as discussed in Section III. Thus, analytic expressions are used. Moreton and Reynolds (27) used Eq. 1, while a Gaussian was found more appropriate by us. Also, the present data were analyzed after correction for porosity. This is consistent with the basis of the uniform stress model. Finally, Reynolds and Moreton analyzed their data to give the exponent m in Eq. 1, which they then compared with theory, whereas the present data were fitted to an expression for the distribution function allowing S_{44} to be estimated.

Figure 11 exhibits several curves for the calculated values of E_Y as a function of $\langle \phi \rangle$ in which S_{44} takes several values. Single-crystal values of S_{11} , S_{12} , and S_{33} and the Gaussian form for $P(\phi)$ were used. The importance of both $\langle \phi \rangle$ and S_{44} can be seen clearly. Similar calculations confirmed that the value of S_{13} was not important within reasonable bounds (see below). These curves allowed the values of S_{44} for each of the fibers tested to be evaluated, listed in Table 1.

These data are displayed in Fig. 12, and compared to similar calculations of Moreton and Reynolds (27) (including recent modifications communicated by Dr. Reynolds), and values of S_{44} are a measure of their "stiffness." It is clear that the values of $1/S_{44}$ are much stiffer than those of single crystal graphite. Two possible reasons for this are (1) that covalent bonds are linking the planes (this would be predominantly at ribbon edges and vacancy loops) and (2) that the ribbons are undulating across their sections, as suggested by magnetic susceptibility measurements (37) and structural characterizations (12,13,14). The response of bent graphene layer stacks to a shear deformation would be restricted compared to that of planar stacks. This would also be consistent with the relatively higher values of $1/S_{44}$ obtained for ex-PAN compared to ex-pitch fibers.

It is noteworthy that the values of $1/S_{44}$ calculated here increase with E_Y , as noted in Fig. 12, whereas those of Ref. 27 decrease. The different approaches used in calculating the values of E_Y have been noted above. These authors also used a different approach to calculate $1/S_{44}$, noting that according to Eq. 13, $G = 2/S_{44}$. This approximation was used in their paper, so that the two results cannot be compared directly. On the supposition that the increase obtained in the present calculations has a physical origin, it is possible that it arises from the increase of the ribbon width with T_{HT} noted by others (see Ref. 2 for a review). If the ribbons so formed undulate across the section, it is conceivable that the increased ribbon width can act to increase the force needed to shear the planes. Models are needed to test this.

Figure 12 also records experimental data for G obtained on ex-PAN (38) and ex-pitch (39,40) fibers. It would be anticipated that

S_{44} would be the most important elastic compliance controlling this parameter, as is the case for Eq. 13. It can be seen that the results presented in Fig. 11 do not support this. This remains a problem that needs to be solved. As discussed above, it may be necessary to obtain G using computer models.

Poisson's ratio is important for determining the PRC. Equation 12 shows that ν also depends on S_{13} . Since S_{13} can be comparable to S_{44} , the uncertainty in this parameter can affect the computed value of ν significantly. Calculations were carried out for the two extreme values of S_{13} and S_{44} given in Table 2. The results are presented in Fig. 13. The importance of S_{13} can be seen clearly in this plot. However, the most important feature of the curves is the increase of ν with E_Y , which is a consequence of the increased alignment of the fibers.

Another important parameter for the PRC is the ratio of the interlayer contraction caused by the application of a tension along the fiber axis, to the longitudinal strain. (This controls the electronic contribution to the PRC discussed in the next section.) Figure 14 plots this parameter ν' as a function of the FWHM, illustrating that it is sensitive to the values of S_{13} and S_{44} , and tends to decrease with increasing E_Y .

Although ν and ν' can be obtained within the framework of the uniform-stress model, it is emphasized that the arrangement of the ribbons across the fiber section is important in determining the local elastic behavior. Accordingly, the above results should only be interpreted as giving a guide to trends.

The Piezo-Electric Coefficient

Piezo-electric effects were measured by passing current via the grips, applying longitudinal stress, and measuring the voltage with two leads attached to the fiber with conducting epoxy (see ref. 1). Results are shown in Figs. 15 and 16 for ex-PAN and ex-pitch fibers respectively. The change in resistance of low modulus fibers is linear, and positive. It will be shown below that the effect is probably related to the elongation and areal contraction (geometric effect). Higher modulus fibers have resistance-strain curves which are non-linear, with negative slopes which are higher at low strains. Since the geometrical effect should increase with higher modulus, the negative coefficient must arise from other effects. It is postulated that electronic effects are responsible. The trend from negative to positive values of the PRC is also observed in catalytic-chemical-vapor-deposited fibers (9), although much larger positive PRCs can be observed. Figure 16 illustrates the experimental data plotted as the PRC (2) versus E_Y (Table 1).

As discussed in the introduction, there are several possible explanations which can be put forward to explain PR. However, the geometric effect must be important in all of them. The change in resistance can then be written as

$$\delta R/R_0 = \delta L/L_0 + \delta A/A_0 + \delta \rho(0\Phi/\rho) \quad [16]$$

where L is the length, A the area, and ρ the resistivity. Using the notation in III, this can be written:

$$\frac{\delta R}{R_o} = \epsilon_{2,2'} - \nu \epsilon_{2,2'} + \delta \nu / \rho_o \quad [17]$$

Dividing by $\epsilon_{2,2'}$, gives the PR coefficient, Z:

$$Z = \frac{1}{\epsilon_{2,2'}} \frac{\delta R}{R_o} = (1 - \gamma) + \frac{1}{\epsilon_{2,2'}} \frac{\delta \rho}{\rho_o} \quad [18]$$

One possible reason for a negative PRC is that the ribbons straighten with applied stress (10). The electrons follow the path of the ribbons, so that this effect would reduce the resistance, since the electric field component along the fibrils would be increased. Note that the path length of the electrons would not be changed. However, the effect would not be the same order of magnitude as the geometrical effect, and it would be anticipated that it would be higher for low modulus fibers, which is contrary to the observations.

The alignment of the ribbons with stress could also lead to a decrease in resistance as a result of reduced electron scattering at boundaries between ribbons and crystallites (6). For example, the applied stress would bring the ribbons closer together, and increase the stress between contiguous areas. However, it would be expected that boundary scattering would be relatively more important in low-modulus fibers, so that the trend would again be contrary to the experimental data.

For these reasons, it was conjectured that changes in the electron density, n , could be responsible for the reduced resistance (11). The origin of this effect is the decrease in the diameter of the fiber and the interlayer spacing as the fiber is strained. This increases the

π -electron overlap between the graphene planes, producing an increase in the electron density, and a proportional increase in the conductivity. The increase of n with c -axis strain is known for graphite from high pressure measurements (see Ref. 40 for a review). On the other hand, n would not increase with c -axis strain for turbostratic carbon, since the overlap of conduction and valence bands is zero (39), and the carrier density is controlled by the density of defects. As three dimensional ordering increases, as outlined in Section II, the coefficient $\delta\rho/\epsilon_{2,2},\rho_0$ should increase. This produces a trend from negative to positive PRC as E_Y increases.

$\delta\rho/\epsilon_{2,2},\rho_0$ would be expected to increase from zero to a value appropriate for single crystal graphite. This latter value can be estimated as follows: n is proportional to the product of the band overlap integrals γ_1 and γ_2 . Furthermore, the hydrostatic stress (P) dependencies these quantities are related by $\partial\ln\gamma_2/\partial P = 2\partial\ln\gamma_1/\partial P$, and have been evaluated as 0.19 and 0.38 GPa (see Ref. 40). Thus, the strain-dependence of the carrier density can be evaluated from these quantities and the c -axis elastic modulus (28.5 GPa (see Ref. 33)), giving

$$\frac{d \ln n}{d\epsilon_{33}} = 20 \quad [19]$$

Thus, neglecting any changes in the mobility with strain,

$$\frac{1}{\rho_0} \frac{d\rho}{d\epsilon_{2,2}} = 20\nu' \quad [20]$$

for a perfectly graphitic fiber at $T = 0$ K. The effects of finite temperature and turbostratic layer order can be taken into account by introducing a dimensionless parameter q , varying from 0 (fully turbostratic at any temperature) to 1 (graphite, $T = 0$ K)

$$\frac{1}{\rho_0} \frac{d\rho}{dE_{2,2'}} = 20q\nu' \quad [21]$$

The vanishing of $d \ln/d\epsilon_{33}$ for turbostratic carbon follows from theoretical work of McClure and Ruvalds (42) who showed that the conduction and valence bands do not overlap in this case (i.e., $\gamma_1, \gamma_2 \rightarrow 0$). This equation does not include changes in electron mobility due to crystallite strain, which is justified for the present fibers, since defect-scattering controls the mobility. Additional terms would be necessary for vapor-grown filaments heat-treated to $\sim 3000^\circ\text{C}$.

The average compression of the graphene planes can be estimated using the uniform stress model, as outlined above, where ν' is the ratio of interlayer strain to applied strain. The values of the elastic parameters and the average ribbon misorientation angle are obtained from the previous section. The parameter that cannot be estimated at the present time is q . It would be affected by several factors other than the overlap of the π -orbitals due to changes in interlayer correlations. Firstly, the effective value of q will be reduced by the thermal excitation of carriers, which increases n from its value at $T = 0$. Secondly, the carrier scattering times are sufficiently short that lifetime broadening results in an increase in n (11). This also

effectively reduces q . Thirdly, defects act as acceptors, lowering the Fermi energy below the bottom of the valence band. This also reduces q .

Accordingly, the approach used here is to use two different values of q corresponding to the turbostratic (two-dimensional) case ($q = 0$), and a partially graphitic fiber with $E_Y \approx 700$ GPa, for which a value of $q = 0.3$ might be appropriate at room temperature. Calculated curves of the piezoresistance coefficient, as a function of Young's modulus, are plotted in Fig. 16 for different values of S_{13} and S_{44} .

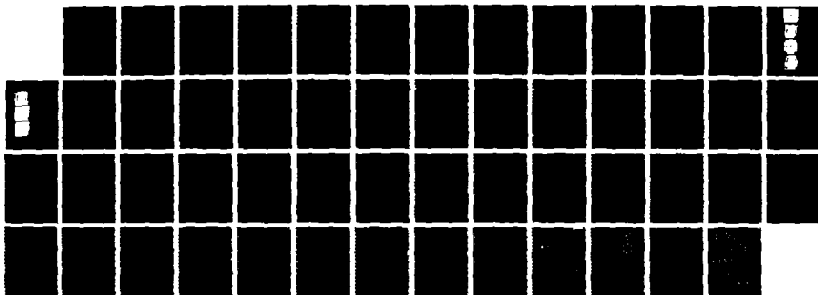
The strain ratio ν' depends sensitively on the values of the parameters S_{13} and S_{44} , so that the magnitude of the electronic contribution is also sensitive to them, and can be positive or negative. However, the curves show that the PRC can have the property of taking increasingly negative values with increase of E_Y similar to the experimental data due to the transition from a turbostratic to partially graphitic structure. This is shown well in Figs. 17a, b, and d. The present data could be fitted with several combinations of these elastic compliances, but in the absence of firm values for q , this would not be a useful exercise.

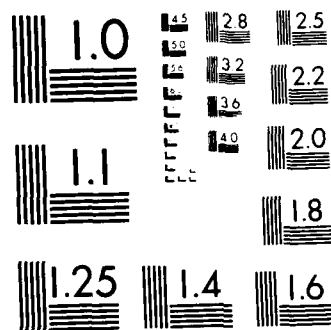
It is also noted, however, that the data fall within the limits predicted by the model when $S_{13} = -1.8 \times 10^{-12}/\text{Pa}$, and does not easily fall within those limits when $S_{13} = -0.33 \times 10^{-12}/\text{Pa}$. The most recent evaluation of S_{13} (34) yields $-0.52 \times 10^{-12}/\text{Pa}$, for which the present PR data can be fitted only with difficulty.

NO 4150 878 SUB-MICRON CARBON FILAMENTS FOR OPTICAL APPLICATIONS 2/3
(U) COLORADO STATE UNIV FORT COLLINS I L SPAIN ET AL
NOV 87 AFOSR-TR-88-0230 F49620-86-C-0083

UNCLASSIFIED

F/G 11/2.1 ML





The Effect of Hydrostatic Pressure on Fiber Resistance

Earlier workers found that the resistance decreased with pressure for low-modulus fibers and increased for high-modulus. The uniform-stress model can be developed to give the change of resistance under hydrostatic pressure due to geometrical effects, as outlined in Table 3. The electronic effect due to the change of carrier concentration with interlayer spacing can also be incorporated, as is done for the case of a graphitic fiber in this table. The compliances S_{13} and S_{33} control the pressure coefficient.

Experimental data were obtained on the pressure-coefficient, $(\partial R/\partial P)_T/R_0$ at room and liquid nitrogen temperatures, up to 0.7 GPa. The results could be summarized as follows:

1. It was found that the resistance did not cycle reversibly. Initially, this was caused by insufficient control of temperature (the resistance change caused by 1 GPa pressure was of the same order of magnitude as caused by a temperature change of 1-10 K). More precise measurements confirmed the mechanical origin of the irreversibility. It was conjectured that the compressing medium was penetrating some of the pores, and causing ribbon-ribbon contacts to be modified. Values of the reduced resistance obtained from each run could be analyzed on increase of pressure to give a pressure coefficient of resistance that was approximately constant for successive runs. Pressure coefficients could be obtained with a precision and repeatability of 0.5%/GPa.

2. In order to explore this further, experiments were carried out with both oil and helium as the pressure transmitting media. Irreversible phenomena were found in both cases.

3. Pressure effects measured in the two above pressure-transmitting media gave different effects. It was conjectured that the helium was penetrating the pores completely, whereas the oil was only penetrating larger ones. This effect was considerably larger than the precision of measurement.

4. There was scatter in the pressure coefficients from one fiber to another obtained from the same bundle. For instance, the pressure coefficient in oil of an ex-pitch fiber with $E_Y = 730$ GPa was found to be $-9.6\%/GPa$ for one fiber, and $-1.4\%/GPa$ for another. By contrast, the pressure coefficient for an ex-PAN fiber with similar E_Y was found to be $-0.146\%/GPa$ and $-0.88\%/GPa$ for another. In addition, the low-pressure data appeared to be more highly scattered than that at higher pressure.

5. The results could not be correlated with E_Y .

For these reasons, it was difficult to draw definite conclusions from the data. It appears that the resistance is very sensitive to the inter-ribbon conformation, and that irreversible phenomena mask the physical effects that are being studied.

Conclusions

The structural, elastic, and piezo-electric properties of ex-PAN and ex-mesophase pitch fibers have been studied experimentally. The fibers were chosen with a wide range of Young's moduli, so that the progression from turbostratic to partially graphitic structures could be followed to the best advantage.

The elastic properties have been compared to the predictions of the uniform-stress model, using an approach in which the shear compliance

S_{44} was adjusted to give the best fit to E_y , while other elastic compliances S_{11} , S_{12} , and S_{33} took their single crystal values. The corresponding values of S_{44} did not bear a simple relationship to the torsional modulus. This may be due to the layer bending within the cross-section of the fiber. The present results have also been compared to previous work using this model.

The PRC was found to be weakly positive for turbostratic fibers, falling to increasingly negative values as Young's modulus increased. This was attributed to an electronic contribution to the PRC which becomes more important as the graphitization of the fiber increases. The uniform stress model was developed for the PRC and the effect of hydrostatic stress on the resistivity.

The above experiments and analysis indicate that the uniform-stress model can be adapted to explain the elastic and piezo-electric properties qualitatively. However, the complicated structure of the fibers across the fiber section needs to be taken into account explicitly, particularly effects due to ribbon bending. This is of technological importance, since ribbon bending is important in arresting crack propagation. It is possible that computer simulations may be capable of computing the elastic moduli.

Acknowledgements

The authors wish to thank several colleagues for assistance in various parts of this work, particularly Ilmar Kalnin, G. Breckenridge, F. Warner, G. Babcock, and K. A. Volin. This research was supported by contracts from ARO to Celanese Research Company (#DAAG29-81-C-0016) and AFOSR to Colorado State University (#F49620-86-C-0083).

References

1. I. L. Spain, K. A. Volin, H. A. Goldberg, and I. L. Kalnin, *J. Phys. Chem. Solids* 44, 839 (1983).
2. M. S. Dresselhaus, G. Fresselhaus, H. A. Goldberg, K. Sugihara, and I. L. Spain, "Carbon Fibers and Filaments," to be published by Springer Verlag.
3. P. C. Connor and C. N. Owston, *Nature (London)* 233, 1146 (1969).
4. C. A. Berg, H. Cumpston, A. Rinsky, *J. Textile Res.* 42, 486 (1972).
5. C. N. Owston, *J. Phys. D3*, 1615 (1970).
6. D. B. F. Fishbach, K. Komaki, and S. Srinivasgopalan, Final report to ARO, DAAG29-76-G0169, 1980.
7. M. Yeoman and D. A. Young, *J. Phys. C2*, 1742 (1969).
8. C. P. Beetz, Extended Abstracts 15th Biennial Conf. Carbon, p. 302 (American Carbon Society, University Park, PA).
9. M. Endo and T. Koyama (private communication).
10. G. J. Curtis, J. M. Milne, and W. N. Reynolds, *Nature* 220, 1024 (1968).
11. H. A. Goldberg, Final report to ARO DAAG29-81-C-0016, 1985.
12. W. N. Reynolds, p. 1 in *Chemistry and Physics of Carbon*, Vol. 11 (1973) (ed. P. L. Walker, Jr., and P. A. Thrower) (Marcel Dekker, New York).
13. D. J. Johnson, p. 1 in *Chemistry and Physics of Carbon*, Vol. 20 (1987) (ed. P. A. Thrower) (Marcel Dekker, New York).
14. R. Bacon, p. 1 in *Chemistry and Physics of Carbon*, Vol. 9 (ed. P. L. Walker, Jr., and P. A. Thrower) (Marcel Dekker, New York).
15. B. J. Wicks, *J. Nucl. Matls.* 56, 287 (1975).
16. M. Guigon, A. Oberlin, G. Desarmot, *Fibre Sci. and Tech.* 20, 55 (1984).
17. A. A. Bright and L. S. Singer, *Carbon* 11, 418 (1979).
18. T. Hamada, T. Nishida, Y. Sajiki, M. Matsumoto, and M. Endo, *J. Mat. Sci.* 4, xxxx (1987).
19. J. Stamatoff, H. Goldberg, and I. Kalnin, p. 61 in *Proc. of Materials Research Society Symposium on Intercalated Graphite* (1982).

20. J. M. Hutcheon, p. 1 in Modern Aspects of Graphite Technology (1970) (ed. L. C. F. Blackman) (Academic Press, New York).
21. R. Perret and W. Ruland, J. Appl. Cryst. 3, 525 (1970).
22. A. Fourdeau, R. Perret, and W. Ruland, Proc. 1st Int. Conf. on Carbon Fibers, London, The Plastics Institute, 1971.
23. H. Tilgner and W. Ruland, p. 28 in Extended Abstract of 18th Biennial Conf. on Carbon (1987) (American Carbon Society, University Park, PA).
24. M. Endo, T. Koyama, and Y. Hishiyama, Jap. J. Appl. Phys. 15, 2073 (1976).
25. W. Vogel and R. Hausman, Carbon 17, 41 (1979).
26. W. N. Reynolds and J. V. Sharp, Carbon 12, 103 (1974).
27. W. N. Reynolds and R. Moreton, Phil. Trans. Roy. Soc., London, A294, 451 (1980).
28. W. Ruland, Appl. Polymer Symp. 9, 293 (1969).
29. L. Fischer and W. Ruland, Colloid and Polymer Sci. 258, 917 (1969).
30. D. J. Johnson, Phil. Trans. Roy. Soc., London, A294, 443 (1980).
31. R. J. Price, Phil. Mag. 12, 564 (1965).
32. P. R. Goggin and W. N. Reynolds, Phil. Mag. 16, 317 (1967).
33. B. T. Kelly, "The Physics of Graphite" (Applied Science Publishers, Ltd., Barking, UK, 1981).
34. Y. X. Zhao and I. L. Spain, to be published in Carbon (see Section III.3 of the Final Report).
35. M. F. Collins and B. C. Haywood, Carbon 7, 663 (1970).
36. J. B. Ayasse, C. Ayache, B. Jager, E. Bonjour, and I. L. Spain, Solid State Commun. 29, 659 (1979) and references therein.
37. J. W. McClure and B. B. Hickman, Carbon 20, 373 (1982).
38. G. D. Dean and P. Turner, Composites 4, 174 (1971).
39. S. Srinivasgopalan, Ph.D. Thesis, University of Washington (available from University Microfilms, University of Michigan).
40. D. B. Fishbach and S. Srinivasgopalan, p. 389, Proc. 5th Int. Conf. Carbon and Graphite London (1979).

41. I. L. Spain, p. 1 in Chemistry and Physics of Carbon 8, (1973) (ed. P. L. Walker, Jr., and P. A. Thrower (Marcel Dekker, New York).
42. J. W. McClure and J. Ruvalds, Symposium on Carbon, Tokyo (1964).

Table 1. Summary of properties of fibers tested.

Fiber	ϕ (FWHM) (°)	(FWHII) (°)	Ratio	L_C (nm)	\tilde{c} (nm)	Nominal Corrected E_Y (GPa)	S_{44} (10^{-12} /Pa)
+celion	R (FWHM)	(FWHII)	Ratio	(nm)	(nm)	(GPa)	(10^{-1} /Pa)
+Celion	32.5	20.6	1.6	2.8	0.354	210	19
+G-50	17.6	11.4	1.5	5.8	0.342	560	22
+GY-70	10.8	7.5	1.4	11.3	0.342	480	19
+GR-21	9.4	5.8	1.6	22.6	0.339	690	12
†VSB	13.5	8.0	1.7			350	66
†VSC	10.4	5.9	1.8			480	54
†P-100	7.1	4.0	1.8			690	21

†Ex-PAN fibers.

†Ex-mesophase pitch fibers.

Table 2. Elastic constants of graphite crystals (33).

Elastic Moduli (GPa)	Elastic Compliance ($\times 10^{-12} \text{ Pa}^{-1}$)
$C_{11} = 1060 \pm 20$	$S_{11} = 0.98 \pm 0.03$
$C_{12} = 180 \pm 20$	$S_{12} = -0.16 \pm 0.06$
$C_{13} = 15 \pm 5$	$S_{13} = -0.33 \pm 0.08$
$C_{33} = 36.5 \pm 1$	$S_{33} = 27.5 \pm 1.0$
$C_{44} = 4.5 \pm 1$	$S_{44} = 240 \pm 60$

Thermal expansion data are consistent with a value of S_{13} between $0-1.8 \times 10^{-12} / \text{Pa}$, but recent compressibility data give a value $(0.52 \pm 0.05) \times 10^{-12} \text{ GPa}$ (34).

Table 3. Hydrostatic pressure.

$$w = \sin \phi$$

$$\epsilon_{y'y'} = -\frac{P}{3} \left[(1-\langle w^2 \rangle)(S_{11}+S_{12}+S_{13}) + \langle w^2 \rangle(2S_{13}+S_{33}) \right]$$

$$\epsilon_{x'x'} + \epsilon_{z'z'} = -\frac{P}{3} \left[(1+\langle w^2 \rangle)(S_{11}+S_{12}+S_{13}) + (1-\langle w^2 \rangle)(2S_{13}+S_{33}) \right]$$

$$\epsilon_{zz} = -\frac{P}{3} \left[2S_{13}+S_{33} \right]$$

2-D resistance change with pressure (turbostratic)

$$\frac{1}{P} \frac{\Delta R}{R} = \frac{1}{3} \left[(1-2\langle w^2 \rangle)(2S_{13}+S_{33}) + 2\langle w^2 \rangle(S_{11}+S_{12}+S_{13}) \right]$$

which for well oriented fibers gives

$$\frac{1}{P} \frac{\Delta R}{R} = \frac{1}{3} (2S_{13}+S_{33})$$

3-D resistance change with pressure (graphitic)

$$\frac{1}{P} \frac{\Delta R}{R} = \frac{1}{3} (2S_{13}+S_{33})(1-2lq)$$

Figure Captions

- Fig. 1. Diffraction photographs of ex-PAN fibers: (a) 210 GPa, (b) 350 GPa, (c) 480 GPa, (d) 690 GPa.
- Fig. 2. Diffraction photographs of ex-pitch fibers: (a) 350 GPa, (b) 480 GPa, (c) 690 GPa.
- Fig. 3. Schematic of x-ray diffraction patterns of carbon fibers: (a) experimental geometry, (b) graphitic fiber with highly oriented ribbons, (c) graphitic fiber with partially aligned ribbons, (d) turbostratic fiber.
- Fig. 4. Comparison of data for the interlayer spacing, \bar{c} , of ex-PAN--o, benzene-derived fibers--•, and anthracene chars--Δ, as a function of T_{HT} (from ref. 24), compared to the present data for ex-PAN--□ and ex-pitch--x fibers.
- Fig. 5. Scans of the (11) reflections, showing the growth of the (112) reflection for ex-PAN and ex-pitch fibers.
- Fig. 6. Widths of the (001) reflections as a function of reciprocal lattice vector squared (ΔK^2), for several ex-PAN fibers.
- Fig. 7. A sketch defining the misorientation angle of a ribbon, ϕ , and the corresponding angle θ which is used by many workers.
- Fig. 8. Profiles of the (002) reflection along the meridians: (a) experimental scan of the lineshape for ex-PAN fibers, (b) resulting rocking curves for ex-PAN, and (c) ex-mesophase pitch fibers.
- Fig. 9. Comparison of experimental values of the mean misorientation angle $\langle\phi\rangle$ (full width at half maximum) as a function of T_{HT} : o--ex-pitch fibers, radial structure (17), •--ex-pitch, random structure (17), □--present data, ex-PAN, x--present data, ex-pitch.
- Fig. 10. Comparison of ribbon stack-height, L_c , as a function of E_{HT} : o--ex-PAN (29), •--ex-pitch (average of several types (17)), □--present results, ex-PAN, x--present results, ex-pitch.
- Fig. 11. Calculated values of E_Y as a function of $\langle\phi\rangle$ for several values of S_{44} .
- Fig. 12. Summary of experimental and theoretical data for the torsional modulus G and the reciprocal elastic compliances for the crystallites, $(1/S_{44})$. Δ experimental data for G (27), •-- experimental data for G , ex-pitch fibers; ■ calculated values for $(1/S_{44})$, ex-PAN (27); calculated values for $(1/S_{44})$ • ex-pitch, □ ex-PAN fibers (27). Curves are drawn as guides to the eye.

- Fig. 13. Plots of Poisson's ratio, ν , as a function of mean orientation angle, $\langle\phi\rangle$, for different values of S_{13} and S_{44} .
- Fig. 14. Plots of the strain ratio, ν' , as a function of $\langle\phi\rangle$ for different values of S_{13} and S_{44} .
- Fig. 15. Experimental curves of the change of resistance with longitudinal strain for ex-PAN fibers.
- Fig. 16. Experimental curves of the relative change of resistance with strain for ex-pitch fibers.
- Fig. 17. Calculated values of the PRC as a function E_y for different values of S_{13} and S_{44} , compared to experimental data: \square --ex-PAN and \times --ex-pitch.

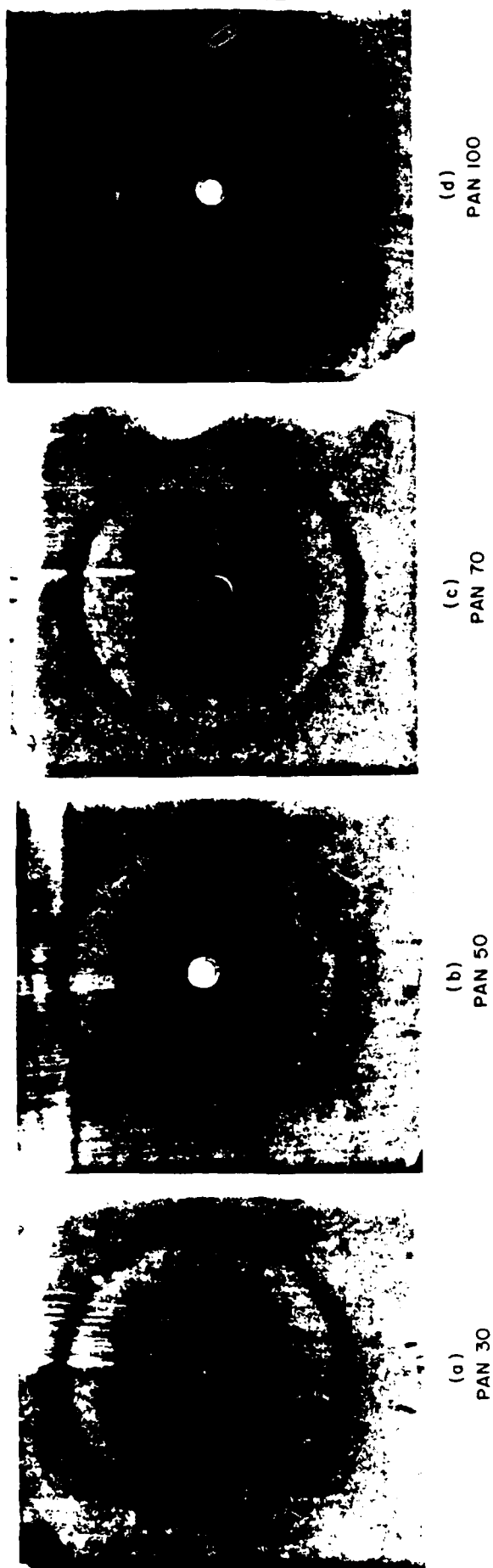


Fig. 1. Diffraction photographs of ex-PAN fibers: (a) 210 GPa, (b) 350 GPa, (c) 480 GPa, (d) 690 GPa.

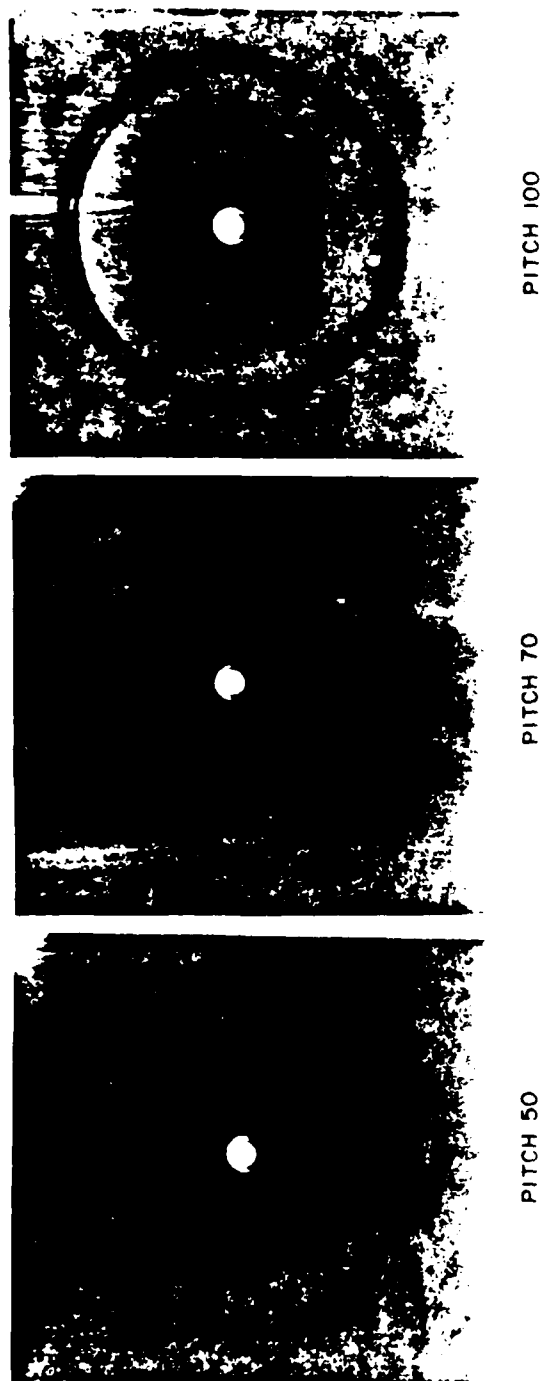


Fig. 2. Diffraction photographs of ex-pitch fibers: (a) 350 GPa, (b) 480 GPa, (c) 690 GPa.

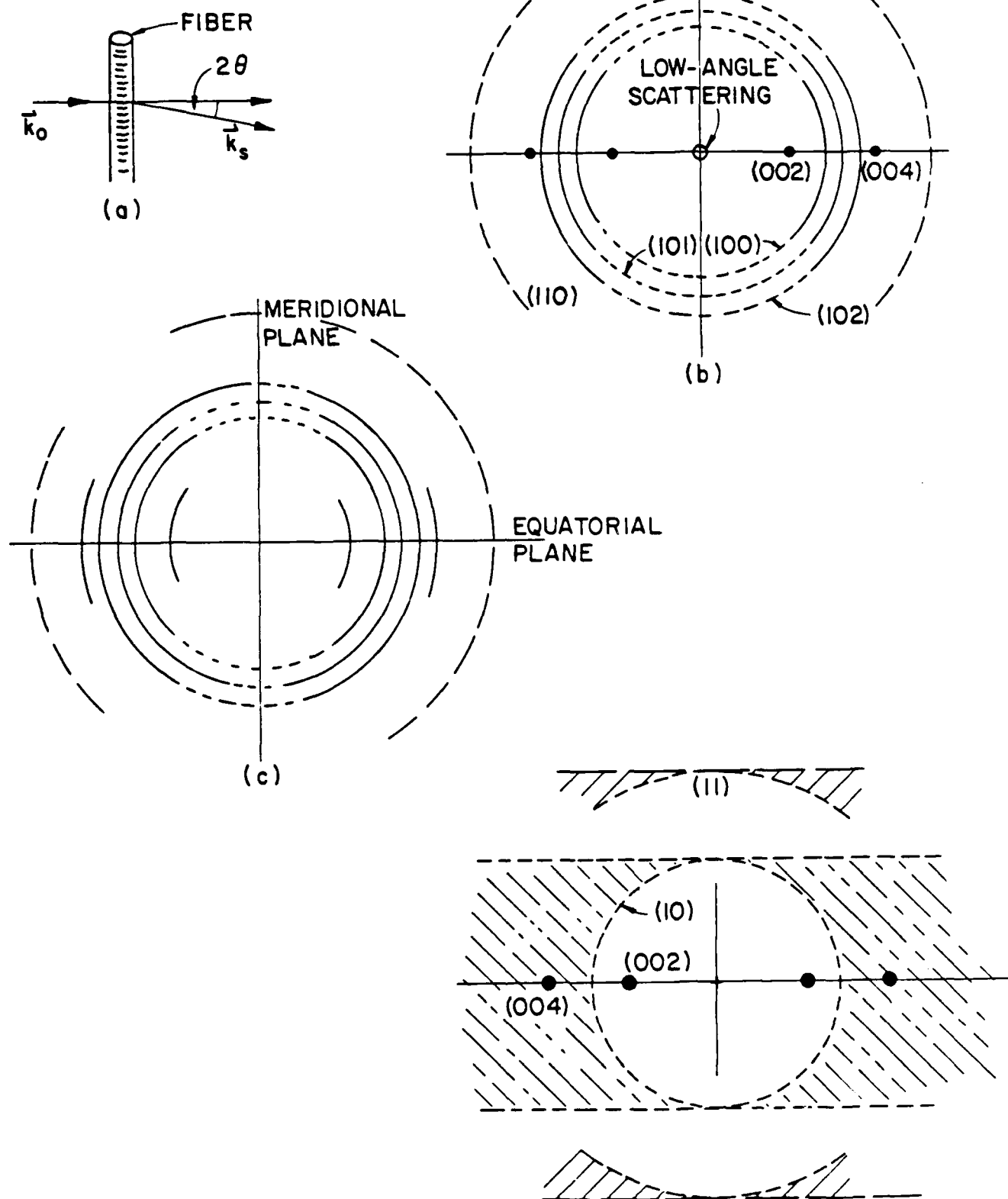


Fig. 3. Schematic of x-ray diffraction patterns of carbon fibers: (a) experimental geometry, (b) graphitic fiber with highly oriented ribbons, (c) graphitic fiber with partially aligned ribbons, (d) turbostratic fiber.

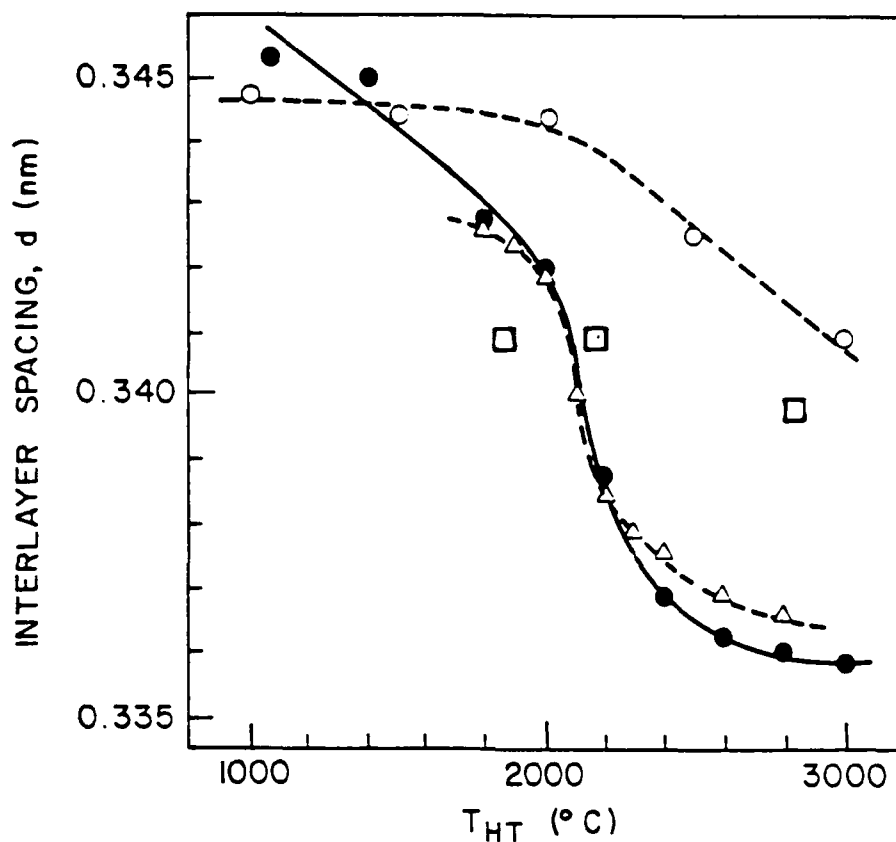


Fig. 4. Comparison of data for the interlayer spacing, \tilde{c} , of ex-PAN--○, benzene-derived fibers--●, and anthracene chars--△, as a function of T_{HT} (from ref. 24), compared to the present data for ex-PAN--□.

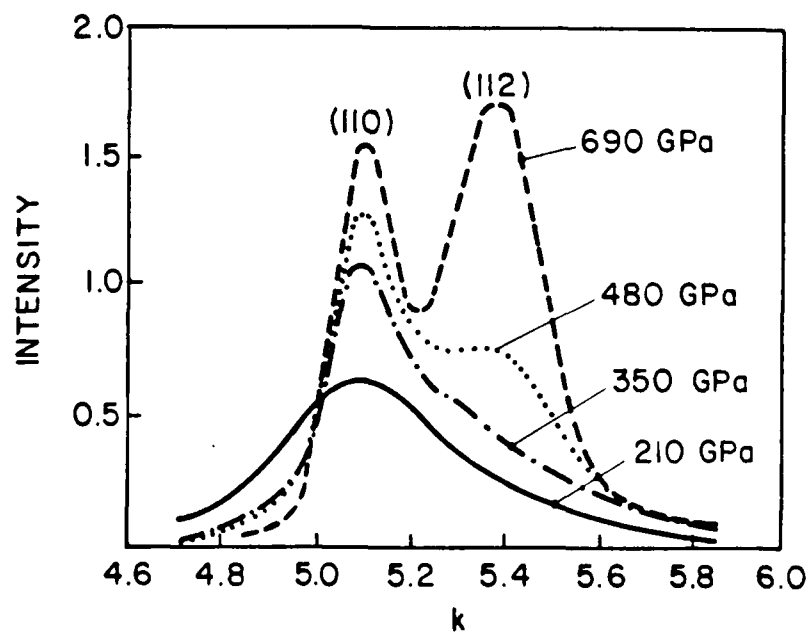


Fig. 5. Scans of the (11) reflections, showing the growth of the (112) reflection for ex-PAN.

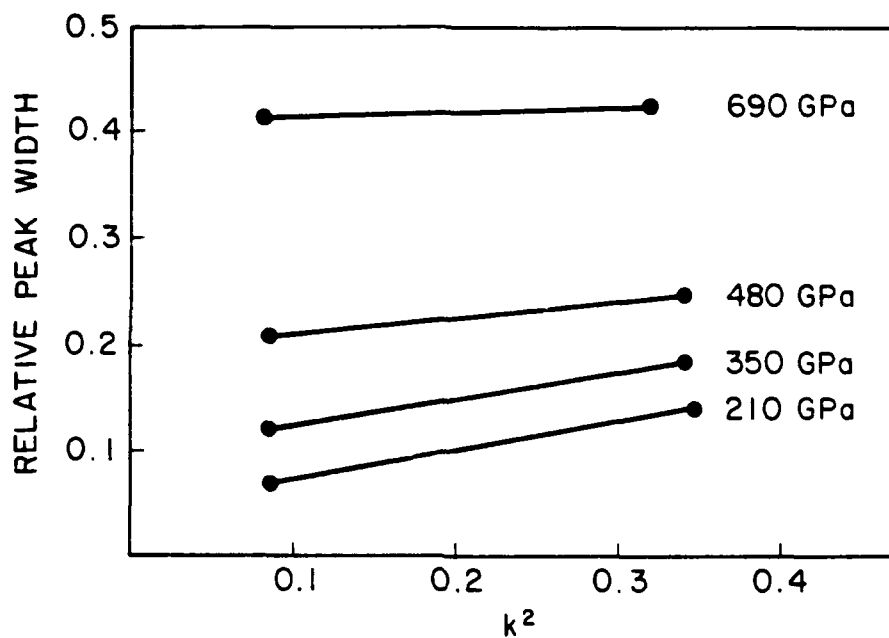


Fig. 6. Widths of the (001) reflections as a function of reciprocal lattice vector squared (ΔK^2), for several ex-PAN fibers.

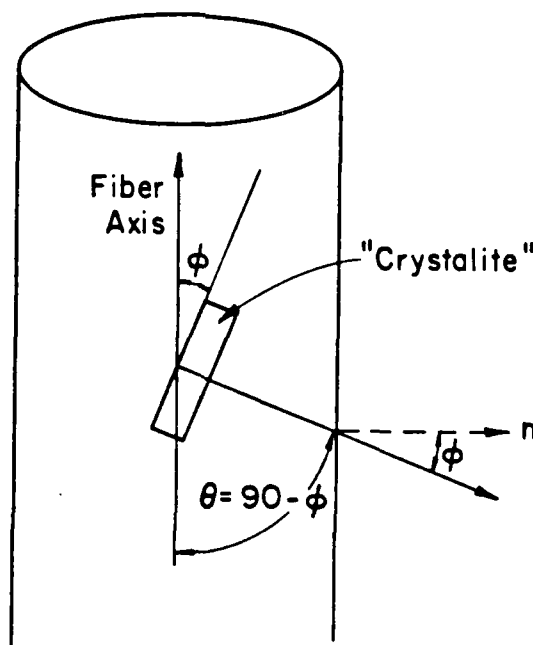


Fig. 7. A sketch defining the misorientation angle of a ribbon, ϕ , and the corresponding angle θ which is used by many workers.

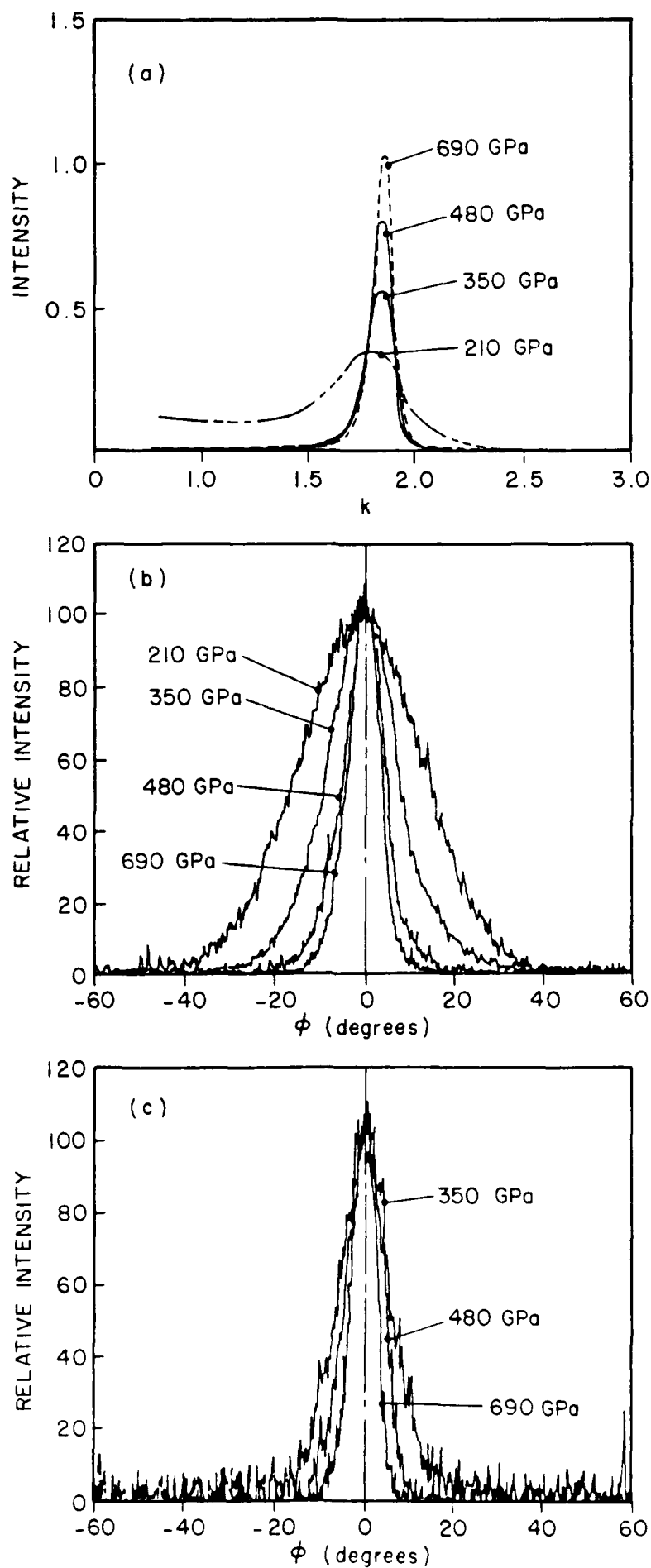


Fig. 8. Profiles of the (002) reflection along the meridians: (a) experimental scan of the lineshape for ex-PAN fibers, (b) resulting rocking curves for ex-PAN, and (c) ex-mesophase pitch fibers

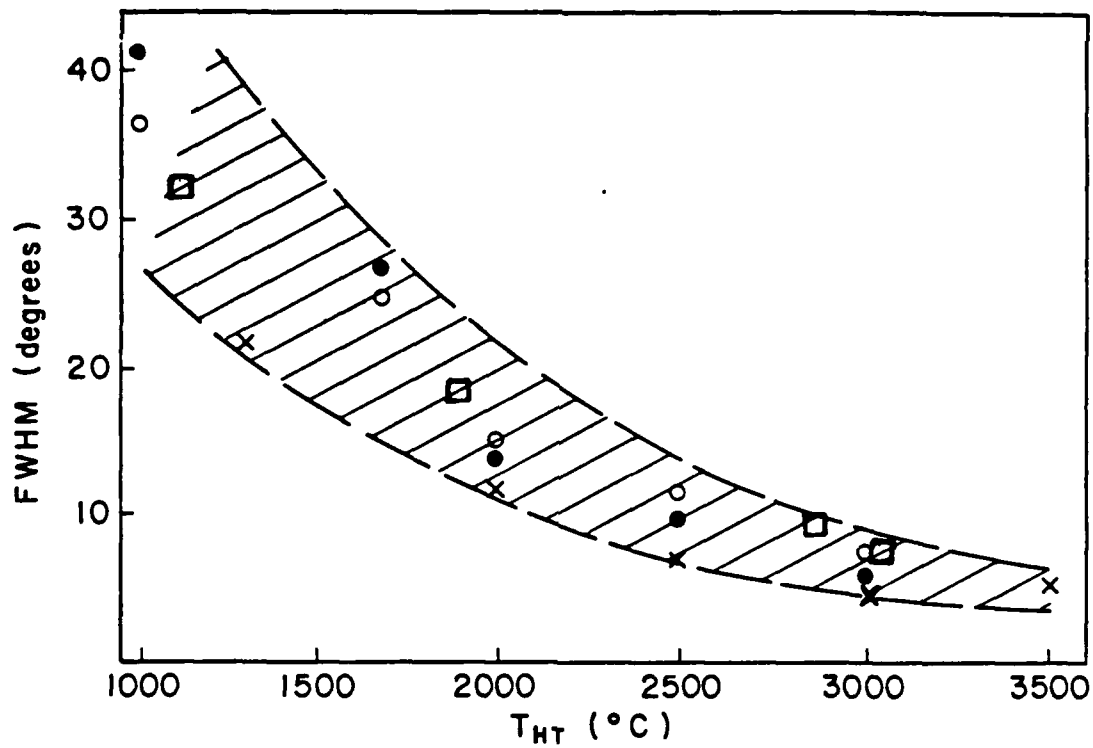


Fig. 9. Comparison of experimental values of the mean misorientation angle $\langle\phi\rangle$ (full width at half maximum) as a function of T_{HT} .
 ○--ex-pitch fibers, radial structure (17), ●--ex-pitch, random structure (17), □--present data, ex-PAN, x--present data, ex-pitch.

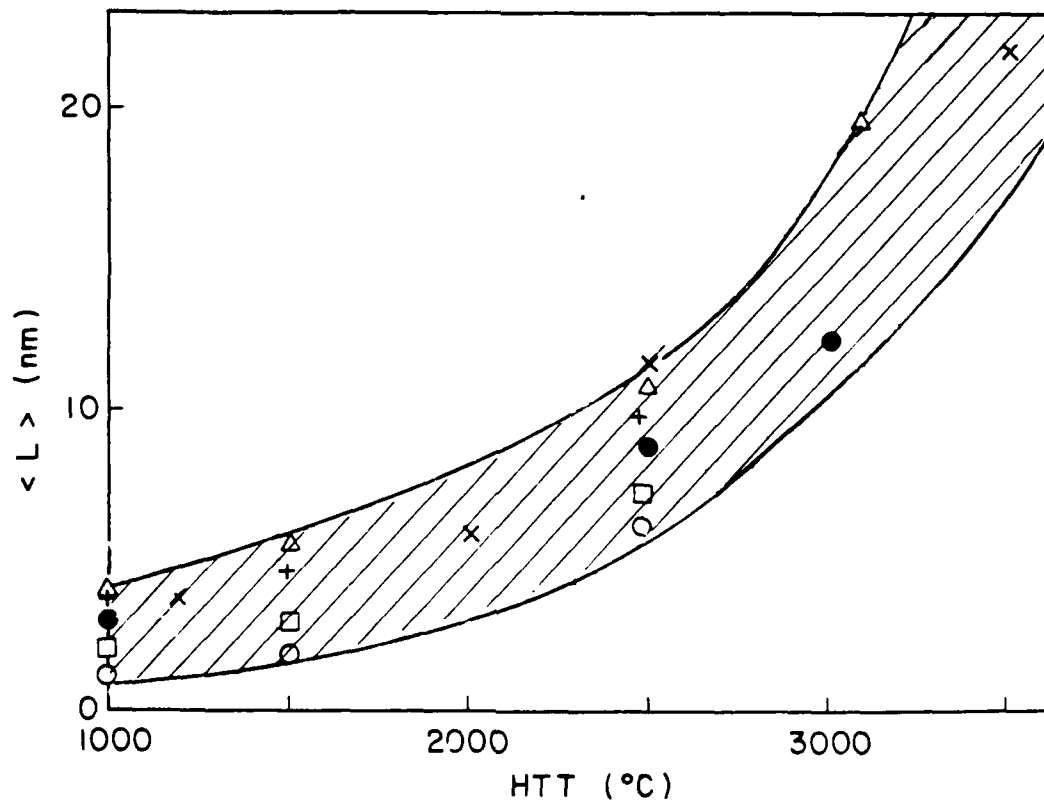


Fig. 10. Comparison of ribbon stack-height, L_c , as a function of T_{HT} .
 ○--ex-PAN (29), ●--ex-pitch (average of several types (17)), □--present results, ex-PAN, x--present results, ex-pitch.

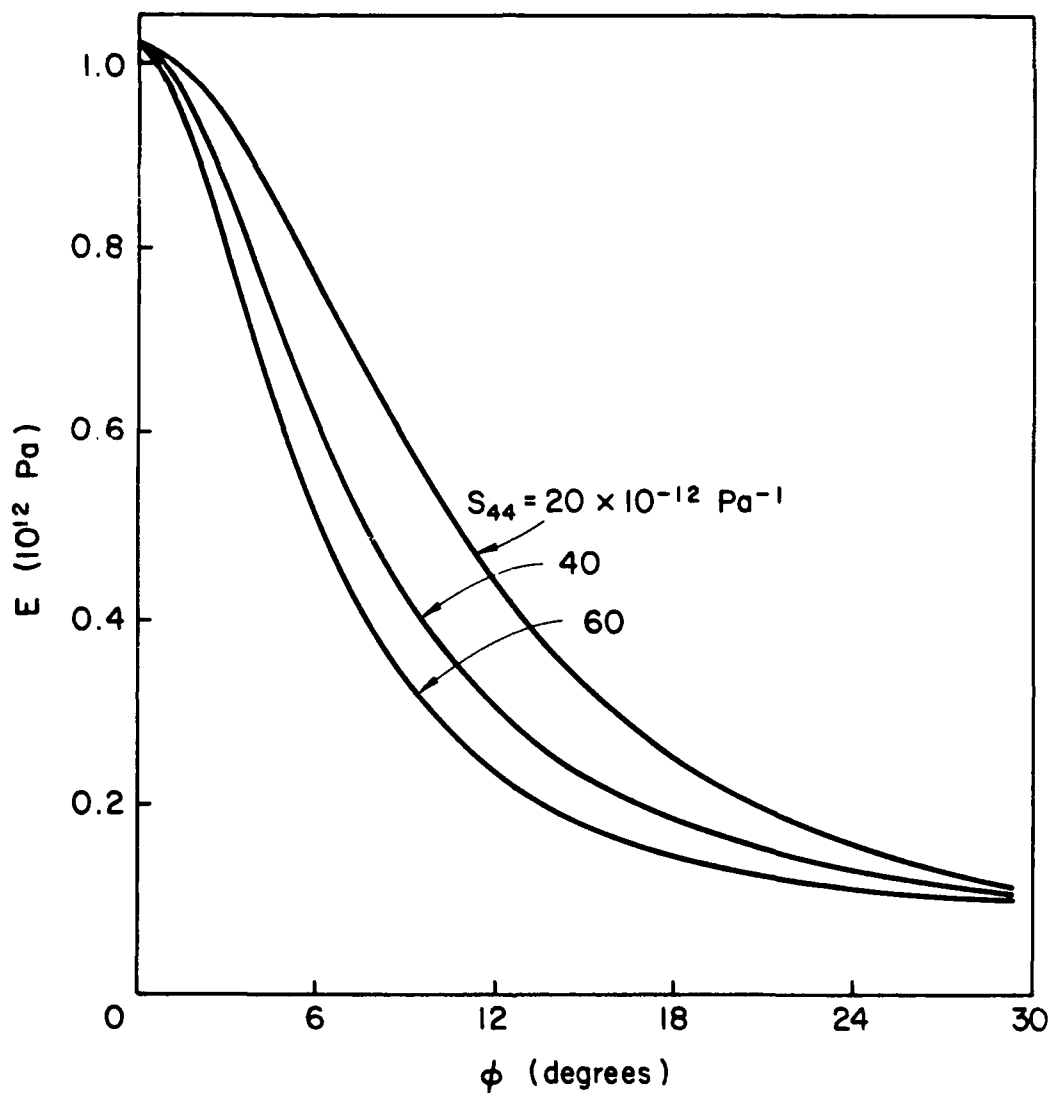


Fig. 11. Calculated values of E_Y as a function of $\langle \phi \rangle$ for several values of S_{44} .

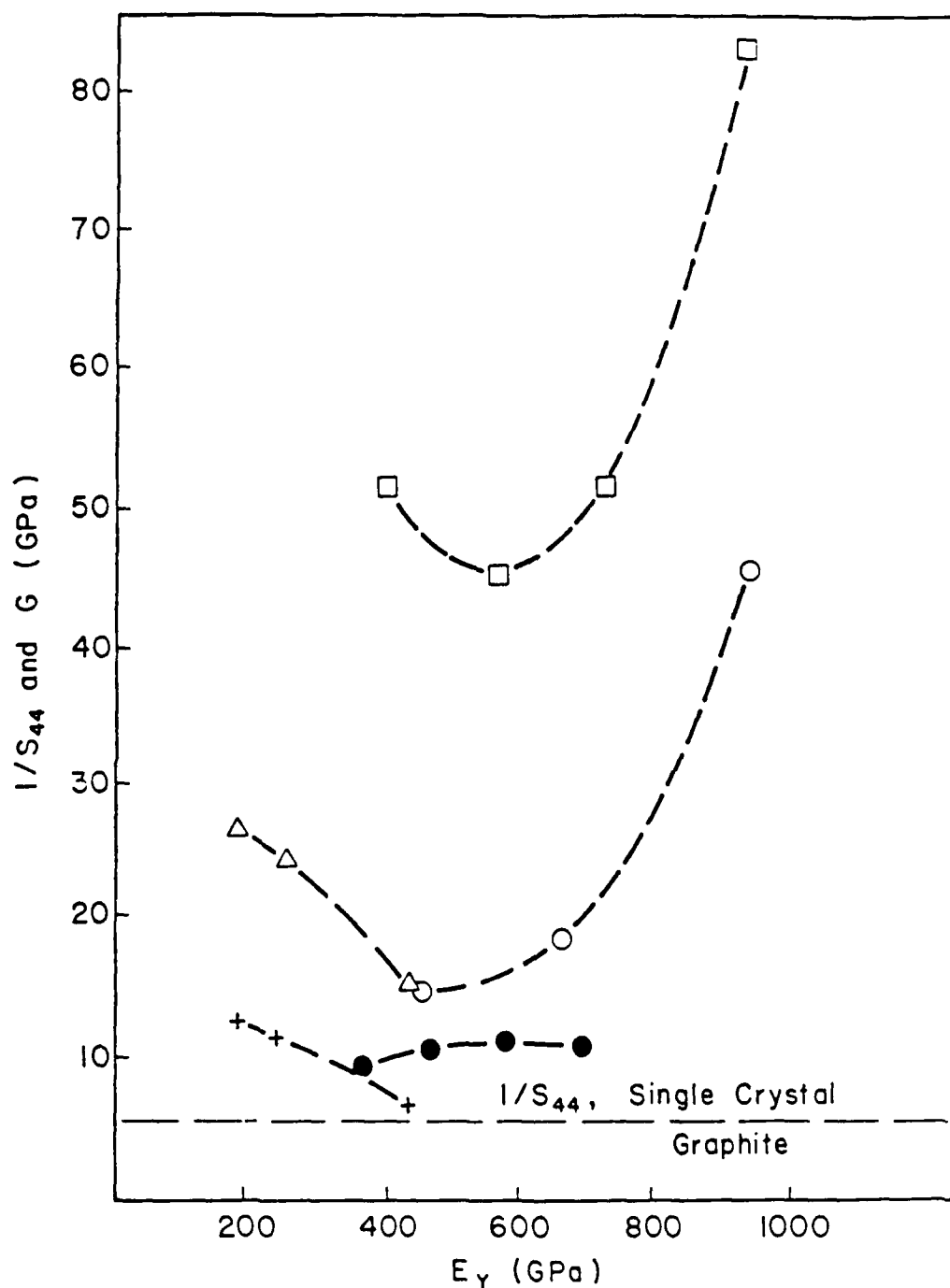


Fig. 12. Summary of experimental and theoretical data for the torsional modulus G and the reciprocal elastic compliances for the crystallites, $(1/S_{44})$. Δ experimental data for G (27), \bullet experimental data for G , ex-pitch fibers; \square calculated values for $(1/S_{44})$, ex-PAN (27); calculated values for $(1/S_{44})$ \bullet ex-pitch, \square ex-PAN fibers (27). Curves are drawn as guides to the eye.

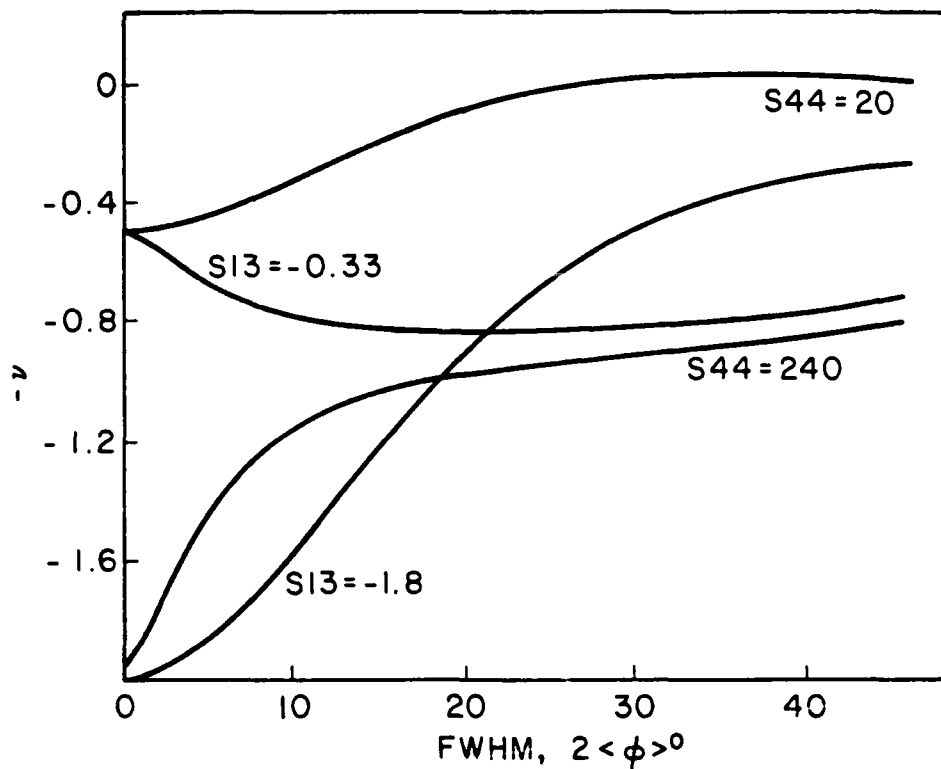


Fig. 13. Plots of Poisson's ratio, ν , as a function of mean orientation angle, $\langle\phi\rangle$, for different values of S_{13} and S_{44} .

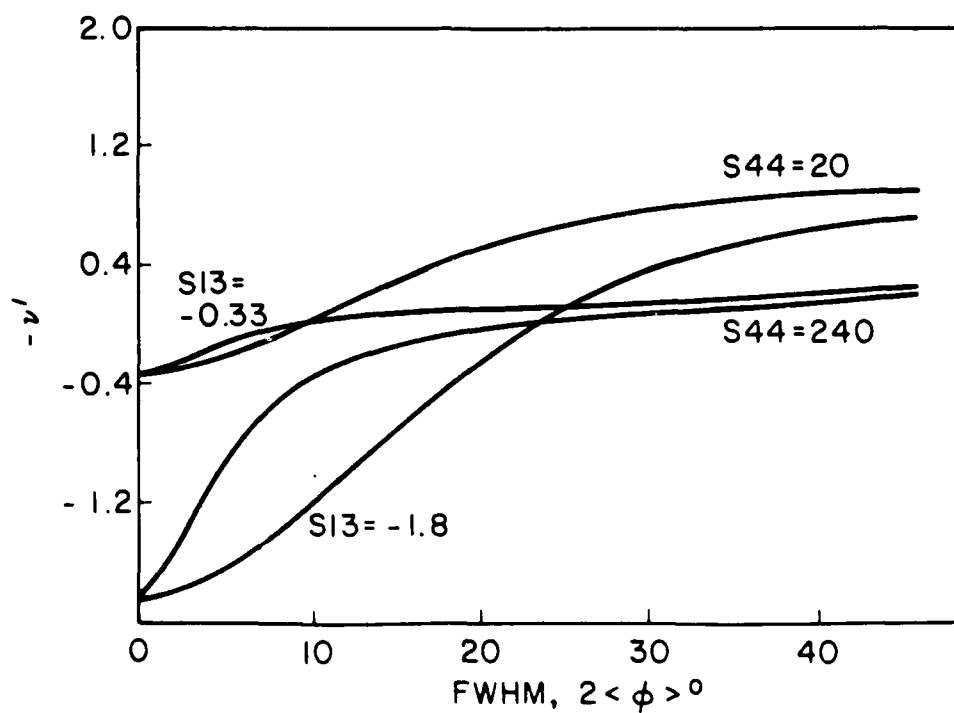


Fig. 14. Plots of the strain ratio, ν' , as a function of $\langle\phi\rangle$ for different values of S_{13} and S_{44} .

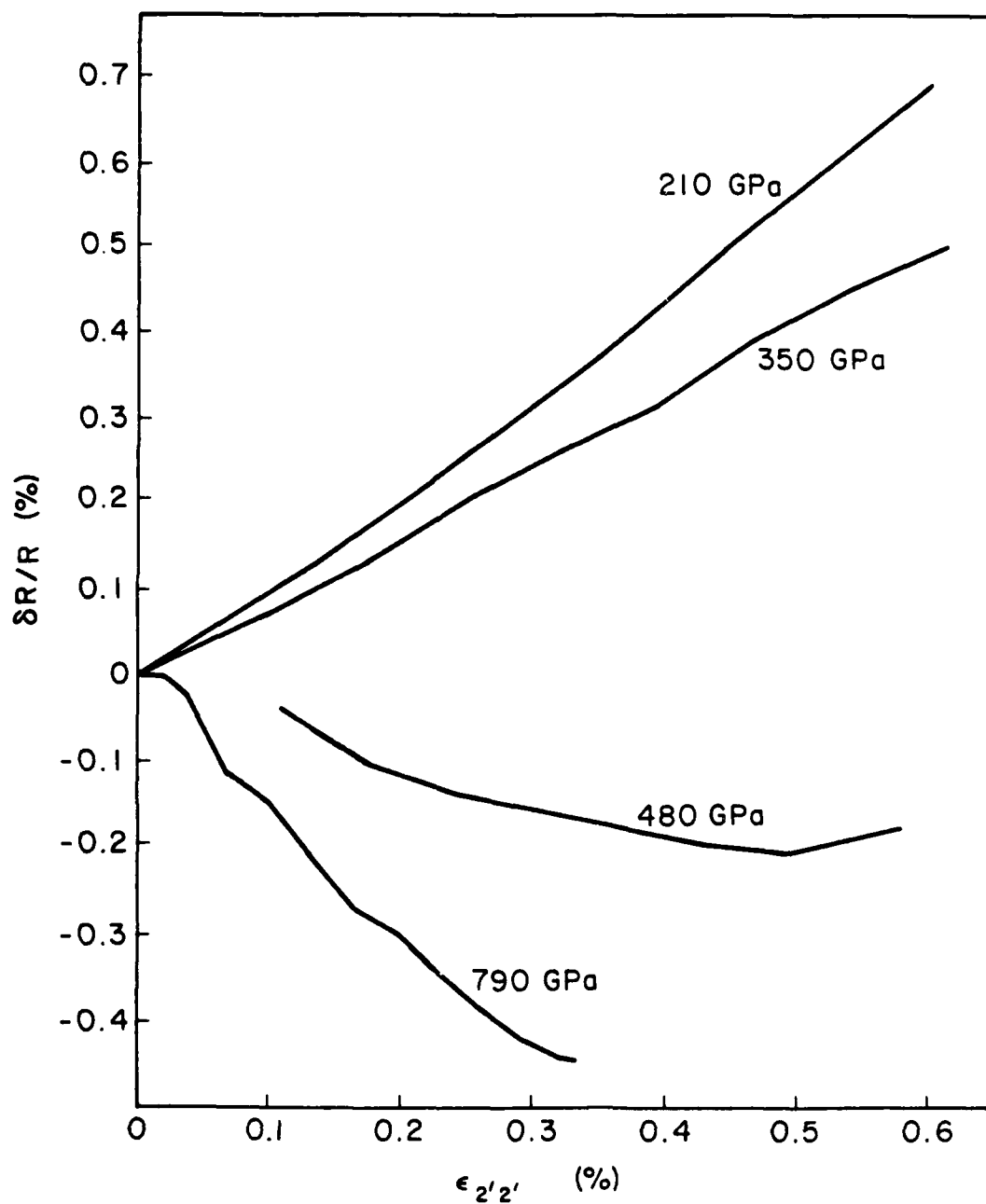


Fig. 15. Experimental curves of the change of resistance with longitudinal strain for ex-PAN fibers.

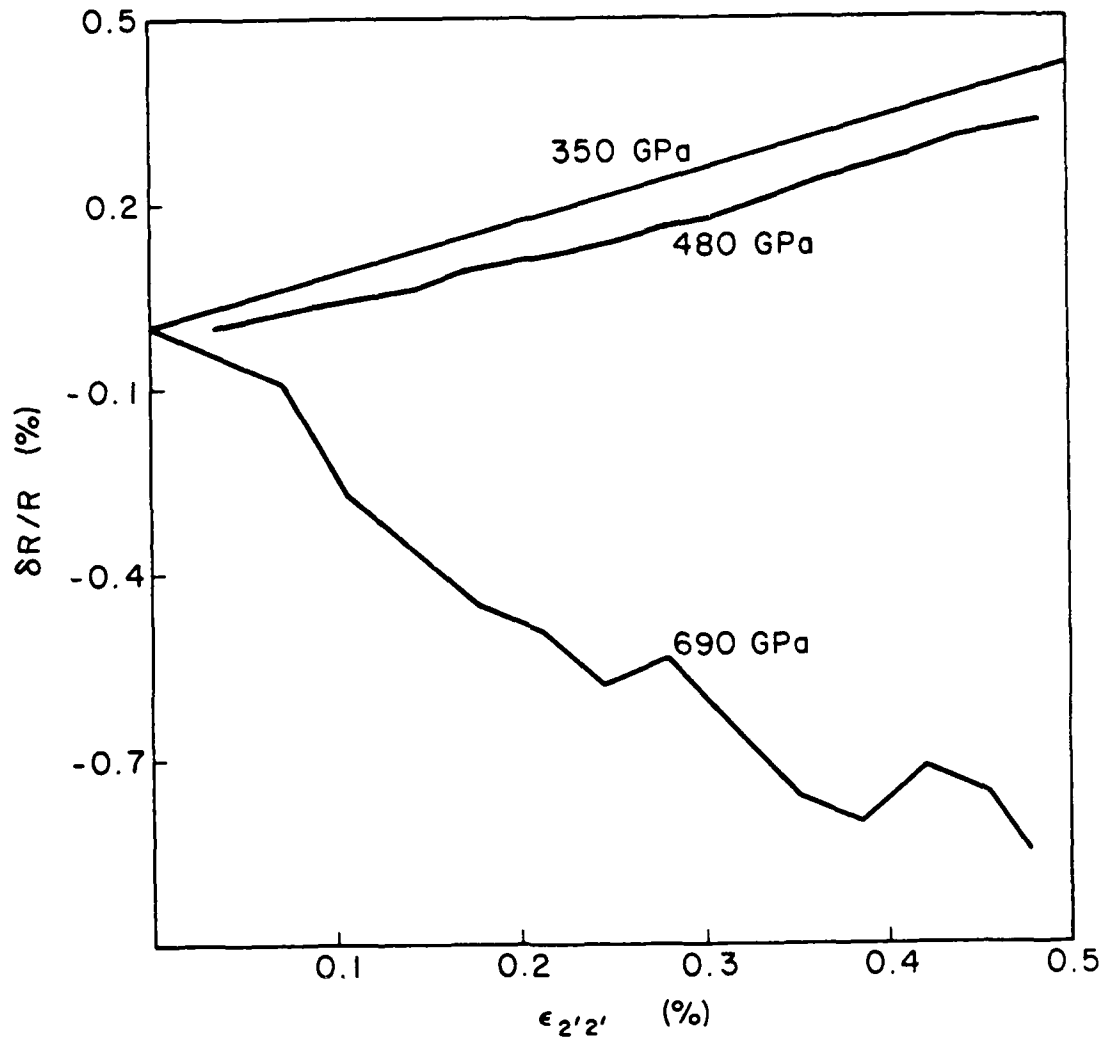


Fig. 16. Experimental curves of the relative change of resistance with strain for ex-pitch fibers.

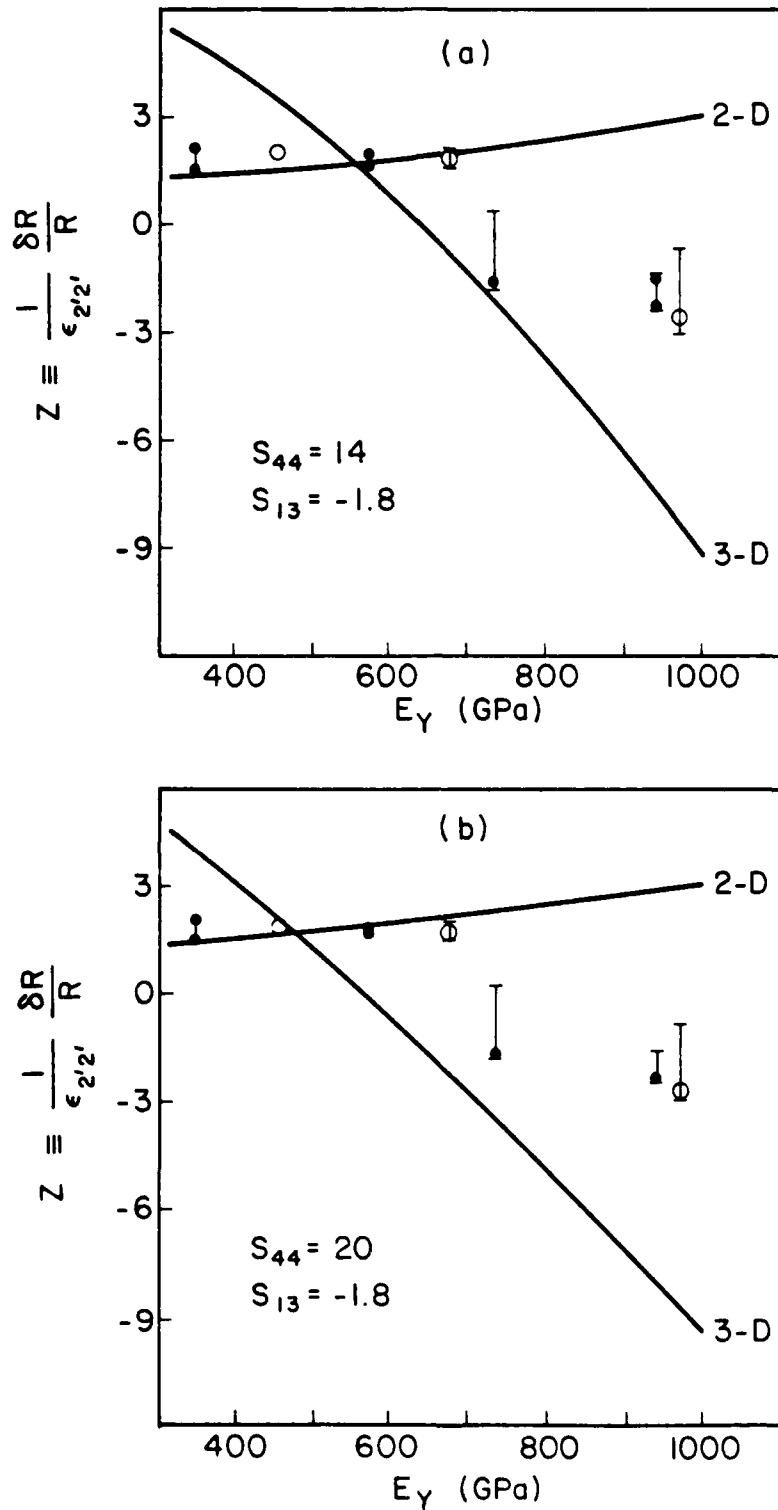
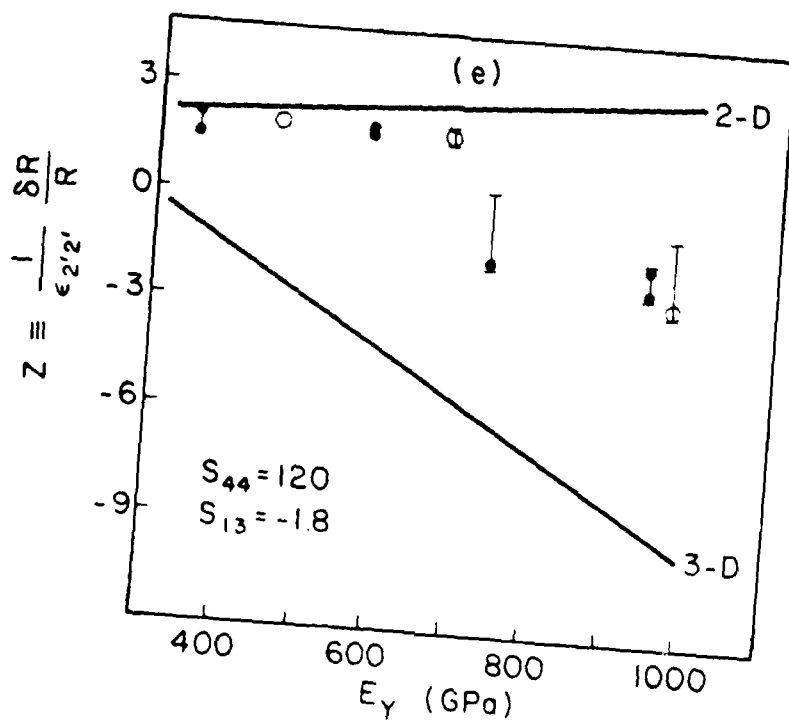
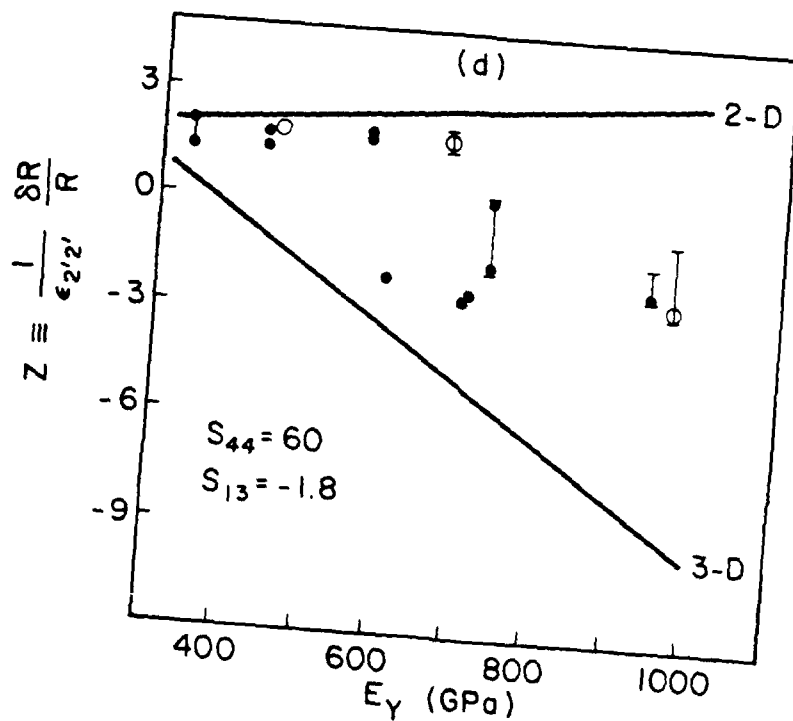
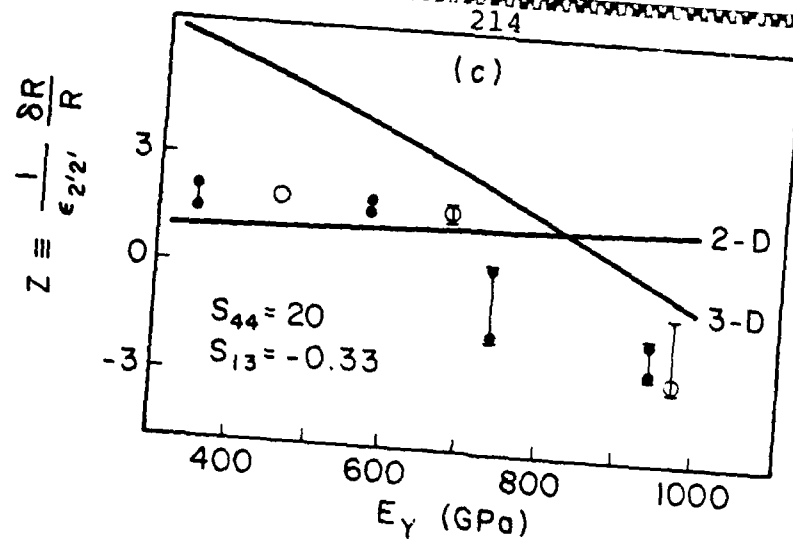


Fig. 17. Calculated values of the PRC as a function E_Y for different values of S_{13} and S_{44} , compared to experimental data: \square --ex-PAN and \times --ex-pitch.



III.3 THE VALUE OF THE ELASTIC CONSTANTS C_{13} AND S_{13} OF GRAPHITE

You-Xiang Zhao⁺ and Ian L. Spain

Department of Physics
Colorado State University
Fort Collins, Colorado 80523

The elastic stiffness constants, C_{ij} , of graphite have been reviewed by Kelly.⁽¹⁾ The experimental uncertainty in the constant $C_{13} = 15 \pm 5$ GPa⁽²⁾ is particularly large. This in turn results in considerable uncertainty in the predicted value of the in-plane bulk modulus $B_a = -a_o(\partial P/\partial a_o)_T$ where a is the lattice parameter, and P the pressure (the subscript T refers to the isothermal value). The relationship between B_a and C_{ij} is:

$$B_a = \frac{X}{2(C_{33} - C_{13})} \quad [1]$$

where

$$X = C_{33} (C_{11} + C_{12}) - 2C_{13}^2 \quad [2a]$$

$$= [S_{33}(S_{11} + S_{12}) - 2S_{13}^2]^{-1} \quad [2b]$$

where S_{ij} are the elastic compliance constants. S_{13} and C_{13} are related by

$$S_{13} = -\frac{C_{13}}{X} \quad [3]$$

The stiffness constants have been evaluated by Blakslee et al.⁽²⁾ yielding

$$X = (4.48 \pm 0.10) \times 10^4 \text{ (GPa)}^2 \quad [4a]$$

$$B_a = 1040 \pm 240 \text{ GPa} \quad [4b]$$

$$S_{13} = -(3.3 \pm 1.1) \times 10^{-4} \text{ (GPa)}^{-1} \quad [4c]$$

Although the ultrasonic value of S_{13} is uncertain, Kelly⁽¹⁾ concluded that the corresponding value of S_{13} , above, is reasonably consistent with thermal expansion and specific heat data.

Jansen and Freeman⁽³⁾ have recently carried out an ab-initio calculation of the elastic constants of graphite. The only input to the computer calculation is the atomic number of the element, and the crystal structure. Correlation and exchange terms are approximated by a method which has given excellent results for other Group IV elements and related compounds.⁽⁴⁾ The computer program allows the electron wavefunctions to be adjusted to minimize the internal energy (at $T = 0 \text{ K}$), thus allowing this energy to be computed for various values of the lattice parameters a and c . One result of this calculation is that C_{13} is close to zero, and possibly negative.

It was noted above the the experimental uncertainty in C_{13} gives rise to a large uncertainty in the calculated value of B_a . However, this situation can be reversed by noting that a determination of B_a can be used to determine C_{13} . We have recently determined B_a using x-ray diffraction measurements in the diamond anvil cell (a detailed report of

the method and results will be given elsewhere⁽⁵⁾). Analysis of the results gives a much stiffer value of $B_a = 1580 \pm 200$ GPa than that calculated above (Eqn. 4b). This gives a value for C_{13} of

$$C_{13} = (23 \pm 2) \text{ GPa} \quad [5]$$

and a corresponding value of S_{13}

$$S_{13} = - (5.2 \pm 0.5) \times 10^{-4} (\text{GPa})^{-1}.$$

This value of C_{13} can be considered consistent with the earlier one,⁽²⁾ within the joint error limits, but is clearly not compatible with the theoretical estimate,⁽³⁾ and in fact changes C_{13} (experimental) further away from the experimental value. A positive value of S_{13} would not be consistent with thermal expansion or specific heat data, nor with piezo-electric coefficients of carbon fibers.⁽⁶⁾ It is noted that the error in B_a is $\pm 13\%$, which is a reflection of the fact that the diamond anvil cell technique has inherent limitations, but also due to a phase transition which occurs at ~ 11 GPa⁽⁴⁾ which limits the range of variation of the lattice parameter $a_p > a(P) > 0.99 a_0$ over which the measurement can be made. Higher accuracy can be achieved in principle by carrying out a single crystal x-ray diffraction experiment in the DAC, and this is planned for the future when the facility for these measurements becomes available at the European Synchrotron Radiation Facility at Grenoble.

Acknowledgements

Thanks are due to the Air Force Office of Scientific Research for a contract (#F49620-84-K-006) supporting this work.

References

1. B. T. Kelly, "The Physics of Graphite," (Applied Science Publishers, London and New Jersey, 1981).
2. O. L. Blakslee, D. G. Proctor, E. J. Seldin, G. B. Spence, T. Weng, J. Appl. Phys. 41, 3373 (1970).
3. H. J. F. Jansen and A. J. Freeman, Phys. Rev. B35, 8207 (1987).
4. See, for example, M. L. Cohen, Science 234, 549 (1986).
5. Y. X. Zhao and I. L. Spain, "Crystal Data for Graphite at High Pressure," submitted to Phys. Rev.
6. H. A. Goldberg, final report to U.S. Army Res. Off. #DAA E29-81-C-0016 (1985).

III.4 ELECTRON TRANSPORT IN CARBON BORON NITRIDE

D. Patel, C. W. Bowers, and I. L. Spain
Physics Department
Colorado State University
Fort Collins, CO 80523

Abstract

Electrical transport measurements have been made on carbon-boron-nitrogen compounds prepared by codeposition. Resistivities increased with BN content, lying in the range $\sim 10^{-5}$ to $>10^4 \Omega\text{m}$, and its weak temperature-dependence suggested that mobilities are controlled by defect scattering, or localization. The magnetoresistance was consistent with this, being less than 10^{-4} at 1 T for all samples at 77 K. The Hall coefficient was positive, suggesting a nitrogen deficiency. The Hall mobility was consistent with the magnetoresistance and resistivity data.

Introduction

Carbon fibers have relatively low room temperature resistivities in the range 10^{-5} - $10^4 \Omega\text{m}$. These low values result from the extensive carbon hexagon networks that are aligned along the fiber axis. Defects in the fibers lower the carrier mobility from values characteristic of single crystal graphite, so that their resistivities are significantly higher (the resistivity of SCG is $4 \times 10^{-7} \Omega\text{m}$ at room temperature (1)).

Some applications of fibers require higher resistivities. One alternative is to use insulating materials such as SiC or BN. Another is to modify the properties of carbon. One possible route is to alloy with BN (2). Substitutional alloys typically have bandgaps that are approximately linear functions of the alloy composition. Accordingly, it was hypothesized (2) that gaps between the value 0 eV for turbostratic carbon and 5 eV for BN could be obtained.

Boron is known to replace carbon substitutionally in graphite at concentrations up to 2.35 atomic % (3). Similarly, it is believed that carbon replaces boron substitutionally in BN (4,5) at small concentrations. Polycrystalline samples containing roughly equal concentrations of C, B, and N were prepared (6,7) as well as thin films (8). These films were examined using x-ray diffraction and photoemission techniques, which indicated that the atoms were located in the hexagonal rings.

Samples have been prepared recently using a codeposition technique based on that used for the preparation of pyrolytic carbon (9). X-ray diffraction results showed that the lattice parameter, a , varied from 2.46 Å of graphite to 2.50 Å of BN as the composition was varied. However, the peaks split into two after hot-pressing, with spacing characteristic of both C and BN. A sample of hot-pressed material with 60% C, 40% BN has also been examined using scanning tunneling microscopy (10). The sample was found to be inhomogeneous, with regions of hexagonal structure.

Measurements of the electrical resistivity, Hall coefficient and magnetoresistance were carried out to characterize the carrier densities

and mobilities, and are reported here. The work is in progress, and the present report is provisional.

Experimental Details

The samples were supplied by Union Carbide Parma Technical Center (9). The carbon content ranged from a few percent to 60%. A Van der Pauw (11) technique was applied for most of the samples with a square geometry to avoid contact resistance and to assume infinite sheet geometry. Typical dimensions were 4x4x0.5 mm. The conventional six arm shape was also employed for two of the samples. Currents were kept small to avoid heating and the contact size minimized to avoid corrections (12). Electrical contacts were made with silver epoxy.

The temperature dependence of the resistivity was measured in a closed-cycle refrigerator in the range 10-300 K. The galvanomagnetic measurements were carried out in a liquid nitrogen cryostat, using an electromagnetic with a maximum field of 1.2 T.

Results and Discussion

Results of the resistivity measurements are summarized in Fig. 1 and Table 1. The temperature dependence of $\rho(T)$ is shown in Fig. 1b. For comparison $\rho(T)$ of other carbon and boronated carbons are shown in Fig. 1a and 2. In general the $\rho(T)$ curves show a small increase with decrease in temperature for all the samples studied here with the exception of 8621-3. This sample shows a sharp rise in ρ with decreasing temperature resembling $\rho(T)$ of the electron beam evaporated thin film in Fig. 1a. The lower carbon content samples showed much

higher values of ρ . This is also consistent with the sharp drop in ρ observed with increasing carbon content in carbon boron nitride reported by Moore (9).

In the presence of a 1 Tesla magnetic field perpendicular to the plane of the sample, no magnetoresistance ($\Delta\rho/\rho$) could be detected for the samples studied with the exception of the hot-pressed sample 8632 HP for which values of $\Delta\rho/\rho \sim 10^{-4} - 10^{-5}$ were obtained at 1 T and sample 8615 for which $\Delta\rho/\rho = 0.123$ at 1 T. This sample has a high carbon content. Unfortunately, no Hall measurements were possible because of large drifts in the readings caused perhaps by an inhomogeneous sample or bad contacts.

Hall measurements at 0.6 T showed very low mobility, μ , in comparison to the high values $\sim 10^3 \text{ cm}^2/\text{V-s}$ for semiconductor materials or $\sim 10^4 \text{ cm}^2/\text{V-s}$ for graphite at room temperature. This is probably due to scattering from a high concentration of defects. Using carrier properties similar to those of graphite would yield a mean free path of $\sim 2 \text{ nm}$. The relative temperature insensitivity of μ is also consistent with this.

The Hall coefficient was positive for all the samples. This is consistent with nitrogen deficiency in the samples. Boronated samples or graphite have been studied extensively (see Ref. 2 for a review). Boron acts as an acceptor, and the Fermi level can be depressed below the bottom of the conduction band by boron doping levels of only 0.1%. The resistivity curves of boronated samples are very similar to those observed by us (compare Figs. 1b and 2; the data from Fig. 2 are adapted from Klein (13)). The temperature-independent resistivity can be explained on the basis of a Fermi level lying below the bottom of the

conduction band, so that only one carrier type is present, with density independent of temperature, and a defect-controlled mobility, which is also independent of temperature. The Hall data will be analyzed in greater detail to give an estimate of the boron deficiency. The c-axis resistivity will also be studied.

Conclusion

Electronic transport properties of carbon boron nitride, including resistivity, magnetoresistivity, and Hall coefficient have been measured as a function of temperature. The temperature dependence of the resistivity showed a small increase for most of the samples with decreasing temperature down to 10 K. The sample with the lowest carbon content gave a steeper resistivity increase. High resistivities compared to graphite have been found in most of the samples, but the values for most of the samples ($\sim 10^{-5} \Omega\text{m}$) were not significantly higher than for typical carbon fibers. No magnetoresistivity was detected for most of the samples. A low mobility of less than $100 \text{ cm}^2/\text{V-s}$ was found.

Acknowledgements

We wish to thank Union Carbide Corporation, Parma Research Center, for funding the initiation of this research and supplying samples through Dr. A. W. Moore.

References

1. D. E. Soule, Phys. Rev. 112, 698 (1958).
2. I. L. Spain, "Chemistry and Physics of Carbon," edited by P. L. Walker, Jr. and P. A. Thrower, 16, 119 (1980).

3. C. E. Lowell, J. Am. Ceramic Soc. 50, 142 (1967).
4. A. W. Moore and L. S. Singer, J. Phys. Chem. Solids 33, 343 (1972).
5. A. Zunger and A. Katzir, Phys. Rev. B 11, 2378 (1975).
6. The first claim of synthesis is by A. Badyan, T. Niemski, S. Oppenheimer and E. Olkusnik, Khim, Svyaz. Poluprov. Polumetallakh, 362 (1972).
7. S. H. Chen and R. J. Diefendorf, Proc. 3rd Int. Carbon Conf. Baden-Baden, p. 44 (1980).
8. R. B. Kaner, J. Kouvetakis, C. E. Warble, M. L. Sattler, and N. Bartlett, Mat. Res. Bull. 22, 399 (1987).
9. A. W. Moore, Proc. 18th Biennial Carbon Conf. (Worcester, MA) p. 523 (1987) (Published by American Carbon Soc.).
10. H. A. Mizes, S. Park, J. Nogami, W. A. Harrison, and C. F. Quate (submitted to Phys. Rev.)
11. L. J. Van der Pauw, Philips Research Reports 13, 1 (1958).
12. H. H. Weider, "Laboratory Notes on Electrical and Galvanomagnetic Measurements," (Elsevier, Amsterdam) (1979).
13. C. A. Klein, J. Appl. Phys. 33, 3338 (1962).

Table 1. Summary of results of electrical transport measurements on carbon boron nitrate alloy from Union Carbide. Square sample geometry was employed with the exception of 8632 HP and 8615 HP where a conventional six arm sample geometry was used.

Sample	% Carbon	$\rho(10^{-3} \Omega\text{cm})$	$\Delta\rho/p^*$	$\mu(\text{cm}^2/\text{v-s})$	T(K)
8604-3	4-6	2.3×10^6		---†	296
8615 HP	60	3.5×10^{-3}	0.123	---†	296
8618 TOP	n/a	707±40 884	0	230±150 43	296 77
8619-I	60	1.2±0.2 1.3	0 0	---¶ ---¶	296 77
8621-2 TOP	n/a	2.7 3.3	0 0	8 9	296 77
8621-3 TOP	n/a	144	0	---†	---
8623	n/a	3.1 3.6±0.6	0 ---	12 12	296 17
8632 HP	n/a	0.17 0.23	5.9×10^{-5} 2.6×10^{-4}	69 39	296 77

*Values at 1 T.

†Unable to measure Hall voltage ($<10^{-6}$ V).

‡Unable to measure Hall voltage--large drifts in readings.

¶Hall voltage same sign for ±B sample inhomogeneous.

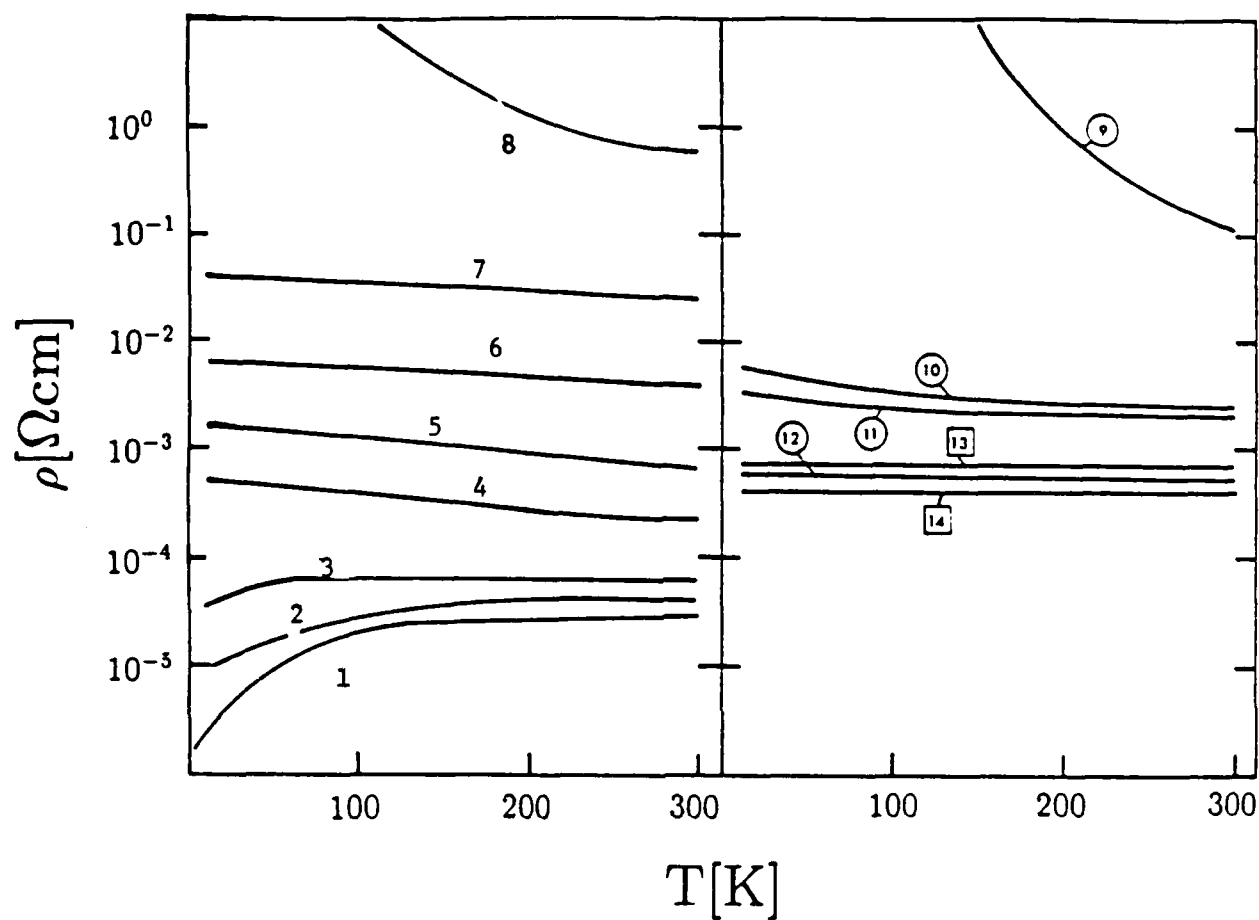


Fig. 1 Resistivities of various carbons and boronated carbons -vs- temperature:

- 1) single crystal graphite, 2) HOPG, 3) graphite whisker, 4) pyrolytic carbon,
 5) petroleum coke carbon, 6) lampblack base carbon, 7) glassy carbon, 8) carbon
 film - electron beam evaporated, 9) 8621-3 Top, 10) 8623 Top, 11) 8621-2 Top,
 12) 8622, 13) 8615 Hot Pressed, 14) 8632 Hot Pressed.

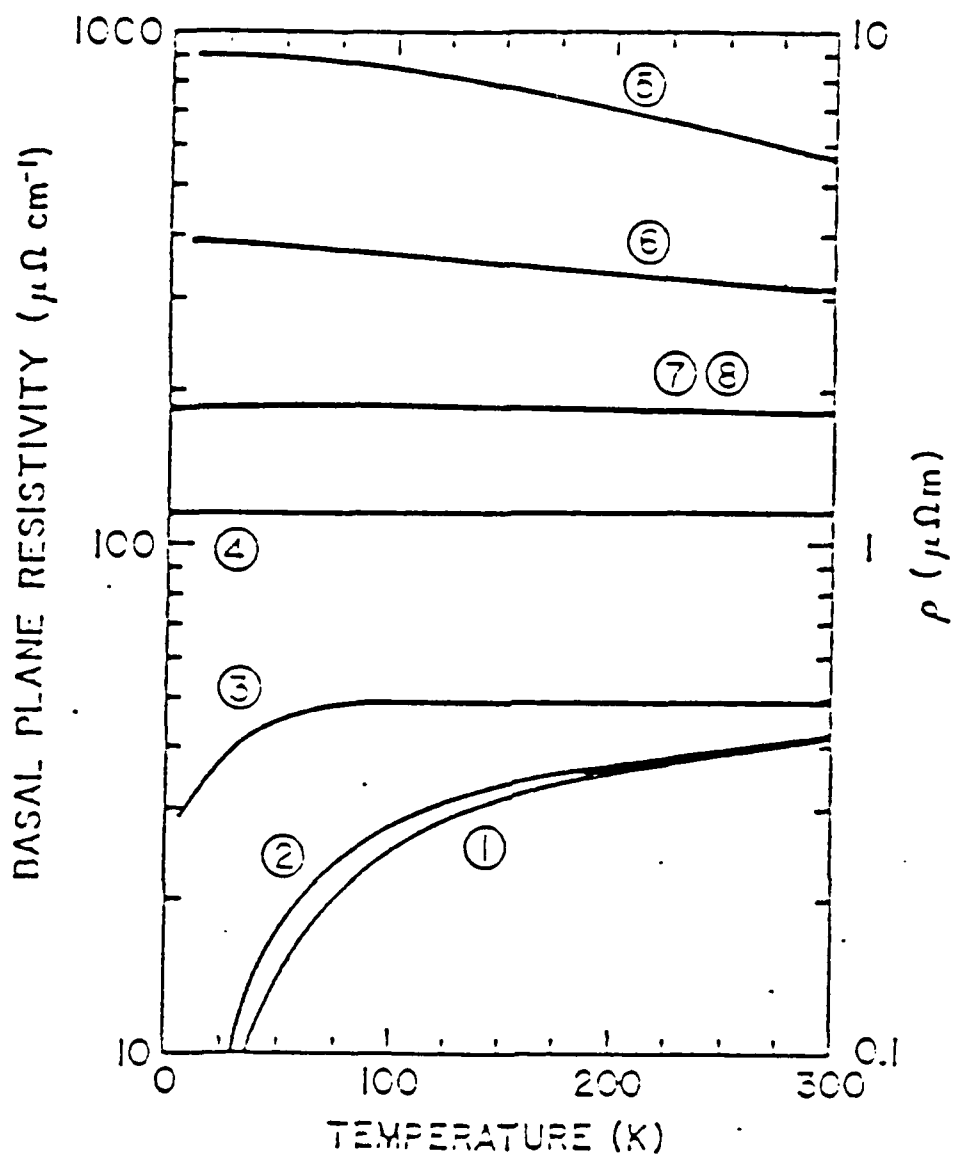


Fig. 13 Resistivities -vs- temperature for boron-doped pyrolytic carbon and graphite (adapted from Klein): 1) NSCG, 2) 3600°C heat-treated PG, 3) 3000°C heat-treated PG, 4) 3000°C heat-treated PG + 3% boron, 5) as-deposited pyrolytic carbon (2100°C), 6) as-deposited PC (2100°C) + 1% boron, 7) PC + 0.3 and 0.6 at. % boron.

IV. REVIEW OF THE PHYSICAL PROPERTIES OF CARBON

FIBERS AND FILAMENTS

A review of the physical properties of graphite fibers and filaments was carried out. The review was originally intended to be of about 120 pages for the journal *Advances in Physics*. However, the final article was of about 500 pages, with 700 references. Accordingly, it will be published as a book in the Springer Series on Materials Science. The publishing date will be about March of 1988.

Since the article is too long to include in this Final Report, only the cover page and List of Contents is included in the following pages.

Graphite Fibers and Filaments

M.S. Dresselhaus, G. Dresselhaus and K. Sugihara

Massachusetts Institute of Technology
Cambridge, MA 02139, USA

I.L. Spain

Colorado State University, Fort Collins, CO 80523, USA

and

H.A. Goldberg

Celanese Research Corp., Summit, NJ 07901, USA

October 29, 1987

Abstract

This review article on carbon fiber research was prepared to initiate graduate students into this field and for use by professionals already working in the field. The coverage is comprehensive and emphasizes topics of particular interest to physicists and materials scientists. This review is written from the point of view of the basic science underlying the properties of carbon fibers. Emphasis is given to those analytical techniques which have been successfully applied to bulk graphite and are now being applied to the study of carbon fibers. The review article specifically considers the preparation, microstructure and defects, electronic structure, lattice, thermal, mechanical, magnetic, electrical and high temperature properties of carbon fibers, together with modifications induced by intercalation and ion implantation, and finishes with a brief discussion of applications. Over 500 references are included which are chosen as much as possible from the recent literature.

Although commercial production is currently concentrated on PAN- and pitch-based fibers, vapor grown fibers have enormous potential in many applications, and have structural features which have enabled novel experiments to be carried out, revealing new physics. Particular attention has therefore been given in this review article to these newly developed vapor grown fibers, in an effort to elucidate the ultimate capabilities of carbon fiber technology.

Contents

1	Introductory Material on Graphite Fibers and Filaments	7
1.1	Introductory Discussion of Structure of Carbon Filaments	9
1.1.1	Ex-polymer Fibers	10
1.1.2	Arc-Grown Carbon Whiskers	12
1.1.3	CCVD Filaments	12
2	Synthesis of Graphite Fibers and Filaments	15
2.1	Carbon Fibers from Polymeric Precursors	15
2.1.1	Ex-Rayon Fibers	16
2.1.2	Ex-PAN Fibers	16
2.1.3	Ex-Pitch Fibers	17
2.2	Carbon Filaments by CCVD	18
2.2.1	General Considerations	18
2.2.2	Detailed Considerations	19
2.2.3	Growth Mechanisms	20
2.2.4	Growth Conditions	22
2.3	Carbon Coated Filaments	25
2.4	Filaments Prepared from Carbon Arcs	26
2.5	Synthesis by ion bombardment	26
3	Structure	31
3.1	Graphite and its Defect Structure	31
3.1.1	Structure of Ideal Graphite	31
3.1.2	Basic Scattering Concepts	32
3.1.3	Point Defects	33
3.1.4	Dislocations	34
3.1.5	Boundaries	35
3.1.6	Turbostratic Graphite	35
3.1.7	Partial Graphitization	36
3.2	Structure of Fibers and Filaments	38
3.2.1	Defects in Filaments with Partially Graphitic Structure	38
3.2.2	Highly Disordered Fibers and Filaments	39
3.3	Density	40

3.4	X-ray Diffraction	41
3.4.1	Interlayer Spacing	42
3.4.2	X-ray Studies of Turbostratic and Partial Graphitized Carbon	42
3.4.3	Preferred Orientation of the c-axes	43
3.4.4	Crystalline Structures of Finite Size	44
3.5	Small Angle Scattering	46
3.6	Optical Microscopy	49
3.7	Electron Microscopy	50
3.7.1	SEM Characterization	50
3.7.2	High Resolution Transmission Electron Microscopy	52
3.7.3	Microstructure of the CCVD Filaments	55
3.7.4	EELS	56
3.8	Other Spectroscopies	56
3.9	Other Characterization Techniques	57
4	Lattice Properties	66
4.1	Elastic Parameters of Single Crystal Graphite	66
4.2	Lattice Dynamics of Single Crystal Graphite	67
4.2.1	Lattice Vibrations in the Long Wavelength Approximation	68
4.3	Models for the Elastic and Lattice Properties of Fibers	70
4.3.1	Effect of Defects on Elastic Parameters	70
4.3.2	Models for Young's and Torsional Moduli of Fibers	71
4.3.3	Rayleigh Waves in Thin Carbon Films	75
4.4	Raman Effect for Single Crystal Graphite	76
4.5	Raman Effect in Disordered Carbons	76
4.5.1	Raman Spectroscopy of Fibers	77
4.6	Photoconductivity in Graphite Fibers	79
5	Thermal Properties	84
5.1	Specific Heat	84
5.2	Thermal Expansion	85
5.3	Thermal Conductivity	88
6	Mechanical Properties	95
6.1	Elastic Parameters	97
6.1.1	Experimental Techniques	97
6.1.2	Experimental Observations	98
6.1.3	Internal Friction	101
6.1.4	Comparison of Elastic Moduli with Theory	102
6.2	Fracture, Stress and Strain	104
6.2.1	Experimental Observations	104
6.2.2	Models of Fracture Processes in Ex-Polymer Fibers	110
6.3	Mechanical Properties of CCVD Fibers	113

7	Electronic Structure	121
7.1	Introduction and Overview	121
7.2	The Slonczewski-Weiss Model for Graphite	126
7.3	Electronic Structure in a Magnetic Field	129
7.3.1	Landau Levels in Three-Dimensional Graphite	129
7.3.2	Landau Levels in Two-Dimensional Graphite	131
8	Electronic and Magnetic Properties	136
8.1	Diamagnetism	136
8.1.1	Diamagnetism in Two-Dimensional Graphite	138
8.1.2	Magnetic Susceptibility of Carbon Fibers	139
8.2	Electron Spin Resonance	141
8.2.1	The g-Shift in Graphite	143
8.2.2	Anisotropy Effects	145
8.2.3	Application of ESR to Vapor Grown Carbon Fibers	146
8.3	Electrical Resistivity	146
8.3.1	Experimental Techniques	146
8.3.2	Electrical Resistivity Data	147
8.3.3	Simple Two Band (STB) Model	149
8.3.4	Size Effects in the Resistivity of Vapor Grown Fibers	151
8.4	Magnetoresistance	153
8.4.1	Positive Magnetoresistance	155
8.4.2	Negative Magnetoresistance	157
8.5	Hall Effect	164
8.6	Thermoelectric Power	164
8.7	Piezoresistance and the Effect of Hydrostatic Pressure	167
8.7.1	Effect of Pressure on Resistance	171
8.8	Non-Ohmic Behavior	172
8.9	Electrical Noise	172
9	High Temperature Properties	188
9.1	High Temperature Thermal Properties	188
9.1.1	Thermal Conductivity	188
9.1.2	Thermal Expansion Coefficient	189
9.1.3	Specific Heats	189
9.2	High Temperature Resistivity	190
9.3	High Temperature Mechanical Properties	191
9.4	Oxidation Resistance	192
9.4.1	Experimental Results	193
9.4.2	Oxidation-Resistant Coatings	194

10 Intercalation of Graphite Fibers and Filaments	199
10.1 Structural Order and Intercalation	201
10.2 Structure and Staging	204
10.3 Lattice Properties	207
10.4 Electrical Transport Properties	209
10.4.1 Electrical Conductivity	210
10.4.2 Magnetoresistance	214
10.4.3 Weak Localization	216
10.5 Thermal Transport Properties	219
10.6 Thermopower	221
10.7 Mechanical Properties	224
10.8 Exfoliation	225
11 Ion Implantation of Graphite Fibers and Filaments	236
11.1 The Ion Implantation Process	236
11.2 Application to Carbon Fibers	238
11.3 Implantation-Induced Structural Modifications	239
11.3.1 Characterization of Samples	241
11.3.2 Regrowth	241
12 Applications of Graphite Fibers and Filaments	245
12.1 Economic Considerations	245
12.2 Structural Applications of Composites	247
12.2.1 Carbon Fiber-Polymer Composites	247
12.2.2 Carbon-Carbon Composites	251
12.3 Electrical Applications for Carbon Fibers	252
12.3.1 Electromagnetic Interference (EMI) Shielding	252
12.3.2 Antistatic Coatings	254
12.3.3 Electrical Devices Near the Percolation Threshold	255
12.3.4 Fibers with Superconducting Coatings	256
12.3.5 CCVD Carbon on Ex-Polymer Fibers	257
12.4 Thermal Applications	257
12.5 Nuclear Applications	258
12.6 Optical Applications	259
12.6.1 Application of Carbon Filaments as Obscurants	259
12.6.2 Low-Reflectivity Surfaces	261
12.7 Applications for Intercalated Carbon Fibers	262
12.8 Batteries and other Electrochemical Applications	263
12.9 Medical Applications	266
13 Acknowledgment	268
14 References	269

VI. REPORT ON SUBCONTRACT "Theoretical Aspects of the Growth and Structure of Carbon Filaments"

James A. Van Vechten
Department of Electrical and Computer Science
Oregon State University
Corvallis, OR

On this subcontract we have studied the structure and the mechanism of growth for carbon whiskers with diameters of order 15 nm that appear on graphite surfaces subjected to sputtering conditions with moderate energy ions, e.g., 1 keV Ar⁺. Our contribution has been the development of theories; we were provided experimental data by our collaborators at the IBM Thomas J. Watson Research Center, particularly P. E. Batson, T.-S. Kuan, and S. M. Rossmagel, as well as by the Colorado State group. These data included scanning electron micrographs (SEM), transmission electron micrographs (TEM), electron diffractograms, and electron energy loss transmission electron micrographs. The theory developed is consistent with all these data and implies predictions for the result of further experiments that hopefully will be performed in the near future. We have also proposed a connection between the mechanism of formation of these whiskers and the formation of the so-called "magic number" carbon clusters over amorphous carbon targets in pulsed laser ablation experiments. Based on our study of the structure of the carbon whiskers, we have given the first explanation of the formation of those clusters that is consistent with the observation that

the "magic numbers" of the neutral and positively charged clusters, but not of the negatively charged clusters, are 11, 15, 19, and 23 but no others. This has also led to the proposal of the structure of amorphous carbon that is consistent with its observed density and the proposal of a new crystalline phase of carbon with remarkable mechanical and electronic properties. Two papers describing this work have been published: "Kink site saturation mechanism for whisker growth under sputtering conditions" by J. A. Van Vechten, et al., J. Crystal Growth 82, 289 (1987); and "Structure of laser-pulse-plasma-induced carbon clusters: Explanation of the magic numbers" by J. A. Van Vechten and D. A. Keszler, Physical Review B (Rapid Comm.) 36, 4570 (1987). (Copies enclosed.) The latter attracted the attention of the popular science press. See Science New, 15 August 1987 (enclosed). It is expected that this work will continue as follows. At Oregon State we have made a proposal to the NSF Materials Processing Initiative (DMR-8712573) (which is still pending and hopeful) to grow the new crystal structure of carbon by a succession of steps: growth of the whiskers by sputtering of graphite; nucleation of single crystals on the tips of these whiskers by laser ablation, photoionization, and mass selection; growth of bulk crystals using a chemical beam epitaxy apparatus developed at OSU by Prof. William Fredericks and hydrocarbon feed stocks produced by Prof. Peter Freeman (Chemistry Department). The IBM Corp. has already donated 400 hours of central processor time (valued at \$400,000) on an IBM 3090 vector array processor, plus a communications link between Corvallis and this machine (in Palo Alto, CA) and \$4000 for travel expenses for state-of-the-art electronic structure calculations re the whiskers and the clusters. These calculations are being performed

mainly by Henri Jansen of the OSU Physics Department. At IBM Watson Research Center, P. E. Batson has enhanced his electron energy loss transmission electron microscopy facility from a single slit detection to 128 slit detection. This provides an enhancement of a factor of 128 in the rate that data can be obtained. This allows correspondingly better statistics regarding the sample spectrum to be acquired before the sample is degraded by the 100 keV electrons of the incident beam. We expect vastly improved spectra for the graphite whiskers that should rigorously test our proposed structures for the whiskers. Finally, in response to a request for proposals from ONR (Max Yoder), we have proposed to use the dense arrays of carbon whiskers produced by sputtering of graphite to form arrays of point contact injectors to inject electrons into diamond, and other materials of interest for defense of spacecraft from laser attack and for ultraviolet detectors and light emitting devices. We have been contacted by Hughes Santa Barbara Research Center regarding this application and have been included as a subcontractor on such a proposal by Hughes.

Structure of laser-pulse-plasma-induced carbon clusters: Explanation of the magic numbers

J. A. Van Vechten

*Department of Electrical and Computer Engineering and Center for Advanced Materials Research,
Oregon State University, Corvallis, Oregon 97331*

Douglas A. Keszler

*Department of Chemistry and Center for Advanced Materials Research,
Oregon State University, Corvallis, Oregon 97331*

(Received 2 March 1987)

A simple explanation is offered for the magic numbers 11, 15, 19, and 23 for carbon clusters produced promptly by pulsed-laser ablation of carbon. The structure proposed for the eleven-member cluster has all C—C—C angles equal to 120° with three five-member rings about two atoms whose p_z orbitals are perpendicular to those of the other atoms. This structure allows one graphitic six-member ring to be formed on each of the three rings upon the addition of four more atoms, thereby accounting for 15, 19, and 23 and for the absence of 7, 27, 31, etc. Extended Hückel calculations indicate the eleven-member cluster is only about 1% less stable than carbon rings or chains under normal conditions. We also find that its highest occupied molecular orbitals have nonbonding character for all nearest-neighbor interactions, and argue that this explains why 11, 15, 19, and 23 are magic numbers for neutral and for positive clusters but not for negative clusters. When stacked together they produce very open structures with a density of 1.4 g/cm^3 . It is proposed that they are common constituents of glassy carbon and of soot and account for the fact that the densities of these materials are much less than those of graphite and diamond. Thus, the observed clusters are present in the target before ablation; they need not form during the pulse.

Several investigations of the material ablated from glassy carbon targets¹⁻⁴ have found remarkable patterns in the distribution of numbers of carbon atoms per cluster, n , and in the photoionization potentials of the most common clusters. The distribution of n is distinctly bimodal. That reported² for neutral clusters by Rohlffing, Cox, and Kaldor (RCK) is shown in Fig. 1. For $n > 40$ only even values of n are found. For $n < 40$ all values are found but certain values, the "magic numbers" $n = 11, 15, 19$, and 23, are much more common than intervening values. We also note that while $n = 3$ is common, 7, 27, 31, 35, etc., are not magic: a $4m + 3$ rule does not describe the data. It should be noted that these same numbers are also magic for those clusters produced in a positive ionization state by the initial laser pulse but not for those produced as negative ions. Negative clusters have entirely different magic numbers: 5, 10, 12, 16, 18, and 22.

RCK give convincing evidence that the bimodal distribution results from two distinctly different processes. In addition to the distinction in the distribution of n , they report that the smaller clusters are produced promptly during a 25-ns laser pulse, while the larger clusters were produced after some time delay, and that the small clusters have a remarkably high photoionization potential, between 6.4 and 12.8 eV as compared with 4.5 and 5.0 eV for graphite and diamond, respectively, while RCK conclude that the $n > 40$ clusters have ionization potentials less than 4.99 eV.

RCK have also given an explanation for the $n > 40$ clusters in terms of a carbyne structure consisting of $-\text{C}\equiv\text{C}-\text{C}\equiv\text{C}-$ chains. However, Cox, Trevor,

Reichmann, and Kaldor cast doubt on RCK's conclusion that the $n > 40$ clusters have ionization potentials lower than 6.4 eV and propose these clusters are spheroidal shells.⁵

RCK do not explain the $n < 40$ clusters but attribute them to the intense plasma present over the target surface during the pulse. (They used 14 to 40 mJ of 532-nm light plus 5 to 10 mJ of $1.06\text{-}\mu\text{m}$ light focused to about 1 mm.)

Bernholc and Phillips (BP) have addressed⁶ the problem with a modified neglect of differential overlap (MNDO) calculation of ring and chain structures with $1 < n < 26$. In addition to calculating the total energies of the various clusters that they considered, they also attempted to simulate kinetic processes by coalescence of single C atoms that were assumed to have been evaporated from the surface. Their result for the relative abundances of neutral clusters is reproduced in Fig. 2. The comparison with Fig. 1, and with the data of others,^{1,3,7} is hardly satisfying. BP state that their calculation finds the $4n + 3$ ring clusters to have particularly low photoionization potentials and suggest that this fact might skew the data in their favor. (RCK photoionized their clusters with various excimer lasers and used a mass spectrometer to determine n .) BP's suggestion is contradicted by RCK's report that these clusters have remarkably high ionization potentials, not low potentials. It also seems reasonable to suppose that the observed abundance is connected to some combination of (i) the structure of the target, (ii) a high cohesive energy of the cluster, and (iii) the dynamic stability of the clusters in the pulse plasma. The last factor may be attributed to either a high ionization energy asso-

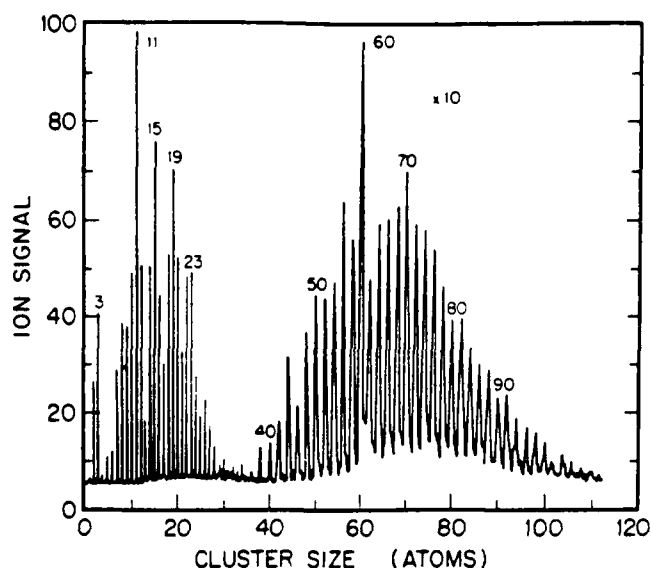


FIG. 1. Reproduction of photoionization time-of-flight mass spectroscopy data reported by Rohlffing, Cox, and Kaldor (Ref. 2) for pulse-laser-ablated carbon targets with ionization of resultant neutral clusters with an unfocused ArF (193 nm) laser. Note that for $n > 20$ the gain was set a factor of 10 higher than for $n < 20$. Also, for $n > 40$ the clusters were ionized with a single photon, while for $n < 20$ two photons were required; the intensities of the two sections of the spectrum cannot simply be compared. The abundance of the $n < 40$ clusters is much greater than that of the $n > 40$ clusters.

ciated with low-lying strongly bound levels, or to highest occupied levels of nonbonding or antibonding character whose ionization would not decrease the stability of the cluster. Our proposal appeals particularly to the latter option. As ionization destabilizes certain clusters, those with low ionization potentials are more easily broken apart in the intense plasma resulting from the pulse. Those with

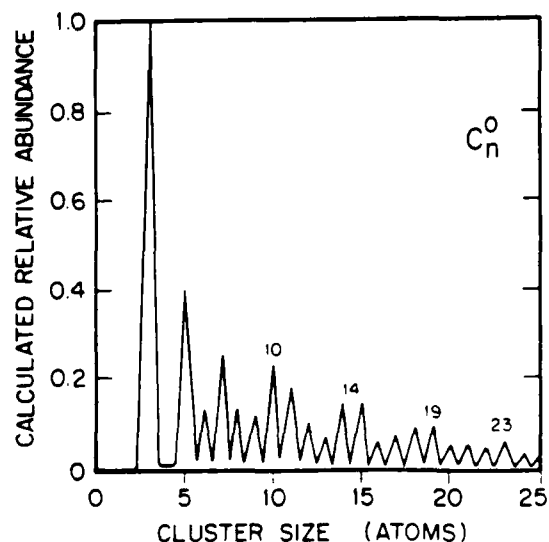


FIG. 2. Reproduction of the MNDO-calculated relative abundances of neutral carbon ring and chain clusters reported by Bernholc and Phillips [Ref. 5, Fig. 3(a)].

very high ionization potentials are more apt to survive in the plasma and tend to be formed from the fragments of the others. This view can be directly applied to the presence of even-numbered carbyne chains⁷ with $n \approx 10$ in these experiments, since the localized $C \equiv C$ interactions with strong π overlap would provide high ionization potentials. In contrast to the present subject, carbyne chains are always even and give up even fragments. (It is one of the single bonds that breaks.)

The present explanation for the odd magic numbers of $n < 40$ clusters has been motivated by an ongoing study of a rather different phenomenon that may involve similar physics. The phenomenon is the formation of very fine (15 nm) whiskers on the surface of graphite subjected to prolonged and moderately intense sputtering.⁸⁻¹⁰ This study has shown the whiskers to be at least semicrystalline but to have a structure that is neither graphitic, nor diamond, nor the scrolled graphite structure of the much thicker whiskers produced by catalytic pyrolysis of hydrocarbons. From studies of these whiskers with transmission electron microscopy (TEM) and electron-energy-loss spectroscopy (EELS), which will be published separately,¹¹ we have concluded that the whiskers contain a mixture of the building unit shown in Fig. 3(a) and the closely related unit shown in Fig. 3(b). The sputtering environment that produces these units involves highly excited, displaced C atoms, which are often ionized, particularly at the tip of the whiskers where a strong field is present. Their density is high where the whiskers are formed. Therefore, it seems reasonable to suppose that the clusters

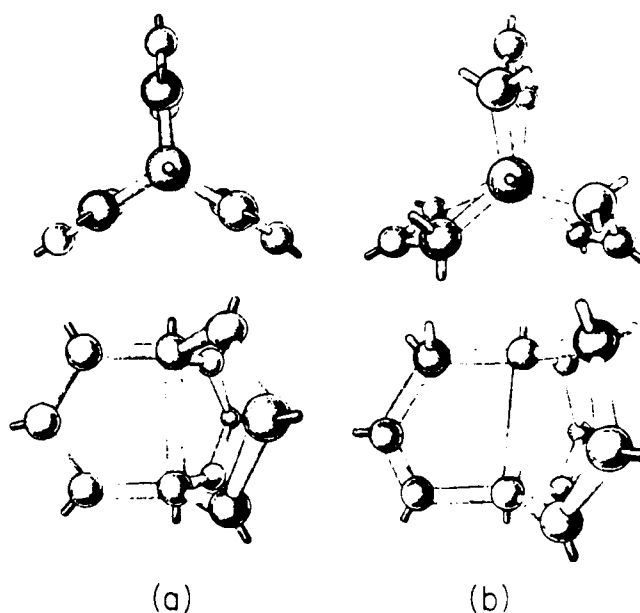


FIG. 3. (a) TUTT, the all- sp^2 -bonded 11-C-atom cluster here proposed to be the $n=11$ magic number cluster. TUTT units are also found in sputter-induced carbon whiskers. (b) TUT, derived from TUTT by converting the three atoms bonded to one of the hub atoms from sp^2 to sp^3 bonding. TUT is less stable than TUTT in free space but allows for much denser packing in a condensed phase. Sputter-induced carbon whiskers contain many TUT units.

condensing to form these whiskers may be present also in the laser-ablation-produced plasma, if not in the original target.

The formal chemical name of the cluster in Fig. 3(a) is tricyclo(3.3.3.0^{1,5}) undeca-2,7,9-triene-4,6,11-triyl, which will hereafter be denoted TUTT. That for the cluster in Fig. 3(b) is tricyclo(3.3.3.0^{1,5}) undeca-2,7,9-triene, which hereafter will be denoted as TUT. This cluster was not considered by BP. However, Hoffmann, Hughbanks, and Kertesz (HHK) have considered crystalline phases of carbon containing closely related units.¹² TUTT contains 11 C atoms arrayed in three five-member rings such that all C-C-C angles are 120°C. The rings have in common two hub atoms whose p_z orbitals are perpendicular to all others and coaxial to the threefold axis. TUTT may be viewed as three partial sections of the graphitic six-membered ring whose terminal atoms are bonded to form hubs through which the threefold axis passes. As an isolated hydrocarbon this may be compressed to a propellerlike structure by $p\sigma$ bonding between hub atoms. In extended or polymeric clusters, this axial bond may lengthen to restore D_{3h} symmetry. TUT differs from TUTT in that three C atoms, one in each side section and at the same side, are sp^3 -bonded rather than sp^2 . This bonding strains the unit rather more, so it is not the stable configuration in free space, but such a carbon framework allows for much more dense packing as a condensed solid, so it may be favored in solids.

Consider now how the carbon framework of TUTT and TUT accounts for the magic-number clusters in the laser-ablation experiment.

(i) They contain 11 C atoms as does the strongest of the magic-number clusters.

(ii) Extended Hückel calculations indicate that its cohesive energy is within 1% of that for a C₁₀ carbyne chain, a C₁₀ carbyne ring, and a C₁₁ cumulene chain ring.

(iii) More important, the highest occupied orbital has much nonbonding character, so the cluster is little destabilized when ionized to a positive state in the plasma. However, addition of an electron to form a negative ion is expected to weaken the bond connecting a side section to the hub atom, leading to fragmentation. Thus, we explain why 11, 15, 19, and 23 are magic for neutral and positive but not for negative clusters.

(iv) The obvious extension of TUTT is to add four atoms on one side section to complete a six-member benzene-type ring, which gives the 15-C atom cluster shown in Fig. 4. This can be done again on the other two side sections to give the 19 magic-number clusters. However, the addition of more than one six-member ring onto one side section severely weakens the bond between the hub atom and its nearest neighbor, which would destabilize the cluster in the plasma environment. This is the explanation for the absence of 27, 31, etc., from the magic number series. The $n=7$ cluster is not magic because it does not suffice to form the basic TUTT unit.

(v) RCK have also studied the photofragmentation of these clusters under excimer-laser irradiation. Their result is shown in Fig. 5. We see that the $n=3$ peak, which was also found in Fig. 1, is dominant here. The same result has been found and elaborated upon by Geusic *et*

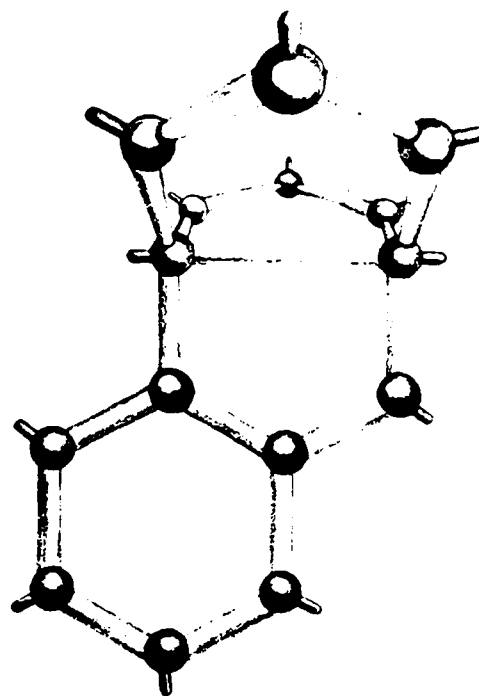


FIG. 4. TUTT+4, the proposed structure of the $n=15$ magic-number cluster. By adding four C atoms to one of the graphite side sections of the TUTT cluster, a graphitic six-member ring is formed. This can be done also on the other two side sections to produce the $n=19$ and $n=23$ magic-number clusters, but no further easy extension is then evident. It is proposed that this is the reason that the magic-number series stops at $n=23$.

al.,¹³ who note that the tendency to photofragment by emitting three atoms is found only for C clusters, not for similar experiments with Si or Ge. (For Si and Ge the numbers 11, 15, 19, and 23 are not magic.) This is explained for C by noting that the weakest bond in TUTT are those bonds connecting the side sections to the hub

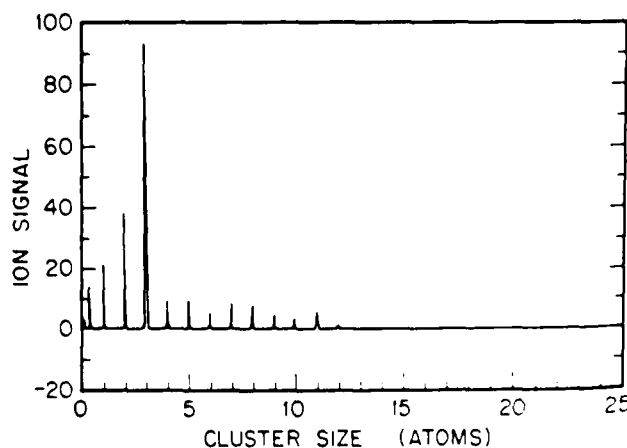


FIG. 5. Data [from Ref. 2, Fig. 4(b)] as with Fig. 1, but with focused, high-intensity (10 mJ) KrF laser used to photoionize and photofragment the neutral clusters.

atoms. Because of the 90° twist of the orientation of the π bonds at these points, this bond does not benefit as greatly from the constructive π -bond overlap between adjacent atoms that so strengthens the in-plane bonding of graphite. Consequently, the most likely fragmentation mode for these clusters is the splitting off of one of the side sections. This produces a three-atom cluster and destabilizes the remaining structure, so that other three-atom side sections may subsequently split off.

(vi) Heath *et al.*⁷ report that the 11, 15, 19, and 23 magic numbers are suppressed if sufficient overpressures of H_2 are introduced at the C target during ablation. Chemical reasoning, and our extended Hückel calculations, imply that saturation of the dangling bonds on the nonhub C atoms severely weakens the bond between hub atoms and destabilizes these clusters.

While our TUTT model provides these natural explanations of the facts, the assumptions that the ablation clusters must be either planar or ring or chain models, as made by BP, has not explained some of the facts. As already noted, BP could not explain why 11, and not 10, is the dominant magic number. They also predict monocyclic structures for $n > 10$, which is inconsistent with the conclusions of Ref. 7. Perhaps most strikingly, the alternative structures do not afford an explanation of the magic number 3 for the photofragments.

If one tries to stack pure TUTT units, without allowing any TUT units or any further twists of the π -bonding axes, as has been considered by HHK, then the structure shown in Fig. 6 is obtained. This "honeycomb graphite" structure has a density of only 1.4 g/cm^3 , as compared with 2.27 for graphite and 3.51 for diamond. It also has a honeycomb of empty hexagonal cylinders which would easily accommodate a wide variety of intercalating species. It is noted that the handbook values of the density of glassy carbon and of soot are in the range 1.8 to 2.0 g/cm^3 . If this structure were derived from either graphite or from diamond, it is difficult to see how this density could be so low. Therefore, it is here proposed that these amorphous phases of carbon may in fact be derived from the TUTT structure of Fig. 6 with a substantial degree of intercollation (and impurities) acting to increase the density of these amorphous materials. Our extended Hückel calculation finds the cohesive energy of this structure to be within 1% of that of graphite. Once formed, such a material should be quite stable. Also, the problem of the formation of the magic-number clusters may be resolved by

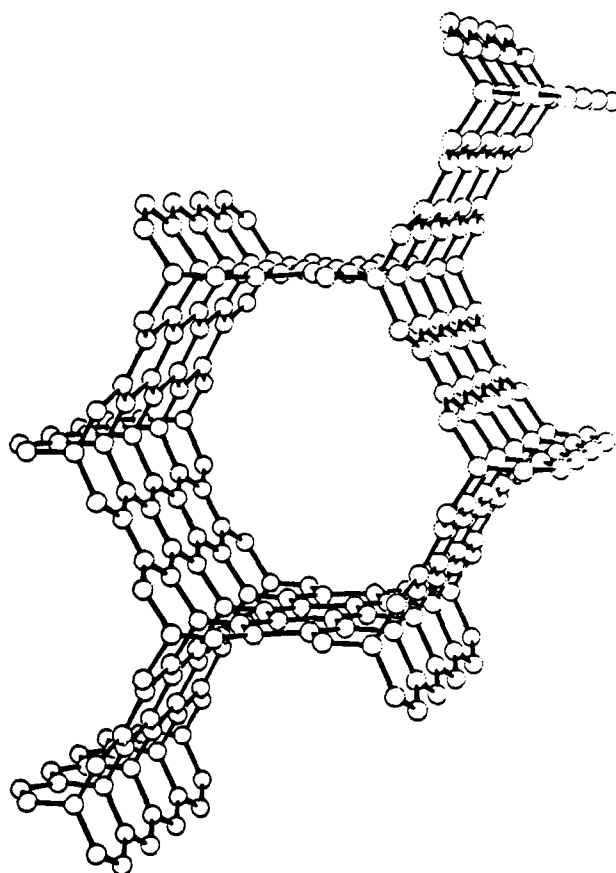


FIG. 6. Low density (1.4 g/cm^3) obtained by stacking TUTT with no conversion to TUT. It is proposed that the presence of (often intercollated) regions of this structure accounts for the low density of glassy carbon and soot.

their presence in the original target. We suggest a comparison of the ablation products of single-crystal graphite and of diamond with those of glassy carbon.

This work was supported in part by the Air Force Office of Scientific Research under Contract No. F-49620-84-K-0006. Support for one of us (D. A. K.) was provided by an M. J. Murdock Charitable Trust Grant of Research Corporation and the Petroleum Research Fund administered by the American Chemical Society.

- ¹N. Furstenau and F. Hillenkamp, *Int. J. Mass Spectrom. Ion Phys.* **37**, 135 (1981).
- ²E. A. Rohlfing, D. M. Cox, and A. Kaldor, *J. Chem. Phys.* **81**, 3322 (1984).
- ³L. A. Bloomfield, M. E. Geusic, R. R. Freeman, and W. L. Brown, *Chem. Phys. Lett.* **121**, 33 (1985).
- ⁴W. L. Brown, R. R. Freeman, K. Raghavachari, and M. Schlüter, *Science* **235**, 860 (1987).
- ⁵D. M. Cox, D. J. Trevor, K. C. Reichmann, and A. Kaldor, *J. Am. Chem. Soc.* **108**, 2457 (1986).
- ⁶J. Bernholc and J. C. Phillips, *Phys. Rev. B* **33**, 7395 (1986).
- ⁷Evidence has recently been reported for the existence of polyyne chains for even-numbered clusters with $n \geq 8$: J. R. Heath, Q. Zhang, S. C. O'Brien, R. F. Curl, H. W. Kroto,

- and R. E. Smalley, *J. Am. Chem. Soc.* **109**, 359 (1987).
- ⁸J. J. Cuomo and J. Harper, *IBM Tech. Discl. Bull.* **20**, 775 (1977).
- ⁹J. A. Floro, S. M. Rossmagel, and R. S. Robinson, *J. Vac. Sci. Technol. A* **1**, 139 (1983).
- ¹⁰J. A. Van Vechten, W. Solberg, P. E. Batson, J. J. Cuomo, and S. M. Rossmagel, *J. Cryst. Growth* **82**, 289 (1987).
- ¹¹P. E. Batson, J. J. Cuomo, S. M. Rossmagel, W. A. Solberg, and J. A. Van Vechten (unpublished).
- ¹²R. Hoffmann, T. Hughbanks, and M. Kertesz, *J. Am. Chem. Soc.* **105**, 4831 (1983).
- ¹³M. E. Geusic, T. J. Mellrath, M. F. Jarrold, L. A. Bloomfield, R. R. Freeman, and W. L. Brown, *J. Chem. Phys.* **84**, 2421 (1986).